



Defense Threat Reduction Agency
8725 John J. Kingman Road, MS
6201 Fort Belvoir, VA 22060-6201



DTRA-TR-15-38

TECHNICAL REPORT

Sensing Fissile Materials at Long Range

Distribution Statement A. Approved for public release; distribution is unlimited.

April 2016

HDTRA1-09-1-0042

Leslie Bromberg et al.

Prepared by:
Massachusetts Institute of
Technology
77 Massachusetts Avenue
Cambridge, MA 02139

DESTRUCTION NOTICE:



Destroy this report when it is no longer needed.
Do not return to sender.

PLEASE NOTIFY THE DEFENSE THREAT REDUCTION
AGENCY, ATTN: DTRIAC/ J9STT, 8725 JOHN J. KINGMAN ROAD,
MS-6201, FT BELVOIR, VA 22060-6201, IF YOUR ADDRESS
IS INCORRECT, IF YOU WISH IT DELETED FROM THE
DISTRIBUTION LIST, OR IF THE ADDRESSEE IS NO
LONGER EMPLOYED BY YOUR ORGANIZATION.

REPORT DOCUMENTATION PAGE				<i>Form Approved</i> OMB No. 0704-0188	
<small>Public reporting burden for this collection of information is estimated to average 1 hour per response, including the time for reviewing instructions, searching existing data sources, gathering and maintaining the data needed, and completing and reviewing this collection of information. Send comments regarding this burden estimate or any other aspect of this collection of information, including suggestions for reducing this burden to Department of Defense, Washington Headquarters Services, Directorate for Information Operations and Reports (0704-0188), 1215 Jefferson Davis Highway, Suite 1204, Arlington, VA 22202-4302. Respondents should be aware that notwithstanding any other provision of law, no person shall be subject to any penalty for failing to comply with a collection of information if it does not display a currently valid OMB control number. PLEASE DO NOT RETURN YOUR FORM TO THE ABOVE ADDRESS.</small>					
1. REPORT DATE (DD-MM-YYYY)		2. REPORT TYPE		3. DATES COVERED (From - To)	
4. TITLE AND SUBTITLE				5a. CONTRACT NUMBER	
				5b. GRANT NUMBER	
				5c. PROGRAM ELEMENT NUMBER	
6. AUTHOR(S)				5d. PROJECT NUMBER	
				5e. TASK NUMBER	
				5f. WORK UNIT NUMBER	
7. PERFORMING ORGANIZATION NAME(S) AND ADDRESS(ES)				8. PERFORMING ORGANIZATION REPORT NUMBER	
9. SPONSORING / MONITORING AGENCY NAME(S) AND ADDRESS(ES)				10. SPONSOR/MONITOR'S ACRONYM(S)	
				11. SPONSOR/MONITOR'S REPORT NUMBER(S)	
12. DISTRIBUTION / AVAILABILITY STATEMENT					
13. SUPPLEMENTARY NOTES					
14. ABSTRACT					
15. SUBJECT TERMS					
16. SECURITY CLASSIFICATION OF:			17. LIMITATION OF ABSTRACT	18. NUMBER OF PAGES	19a. NAME OF RESPONSIBLE PERSON
a. REPORT	b. ABSTRACT	c. THIS PAGE			19b. TELEPHONE NUMBER (include area code)

UNIT CONVERSION TABLE

U.S. customary units to and from international units of measurement^{*}

U.S. Customary Units	Multiply by   Divide by [†]		International Units
Length/Area/Volume			
inch (in)	2.54	$\times 10^{-2}$	meter (m)
foot (ft)	3.048	$\times 10^{-1}$	meter (m)
yard (yd)	9.144	$\times 10^{-1}$	meter (m)
mile (mi, international)	1.609 344	$\times 10^3$	meter (m)
mile (nmi, nautical, U.S.)	1.852	$\times 10^3$	meter (m)
barn (b)	1	$\times 10^{-28}$	square meter (m ²)
gallon (gal, U.S. liquid)	3.785 412	$\times 10^{-3}$	cubic meter (m ³)
cubic foot (ft ³)	2.831 685	$\times 10^{-2}$	cubic meter (m ³)
Mass/Density			
pound (lb)	4.535 924	$\times 10^{-1}$	kilogram (kg)
unified atomic mass unit (amu)	1.660 539	$\times 10^{-27}$	kilogram (kg)
pound-mass per cubic foot (lb ft ⁻³)	1.601 846	$\times 10^1$	kilogram per cubic meter (kg m ⁻³)
pound-force (lbf avoirdupois)	4.448 222		newton (N)
Energy/Work/Power			
electron volt (eV)	1.602 177	$\times 10^{-19}$	joule (J)
erg	1	$\times 10^{-7}$	joule (J)
kiloton (kt) (TNT equivalent)	4.184	$\times 10^{12}$	joule (J)
British thermal unit (Btu) (thermochemical)	1.054 350	$\times 10^3$	joule (J)
foot-pound-force (ft lbf)	1.355 818		joule (J)
calorie (cal) (thermochemical)	4.184		joule (J)
Pressure			
atmosphere (atm)	1.013 250	$\times 10^5$	pascal (Pa)
pound force per square inch (psi)	6.984 757	$\times 10^3$	pascal (Pa)
Temperature			
degree Fahrenheit (°F)	[T(°F) – 32]/1.8		degree Celsius (°C)
degree Fahrenheit (°F)	[T(°F) + 459.67]/1.8		kelvin (K)
Radiation			
curie (Ci) [activity of radionuclides]	3.7	$\times 10^{10}$	per second (s ⁻¹) [becquerel (Bq)]
roentgen (R) [air exposure]	2.579 760	$\times 10^{-4}$	coulomb per kilogram (C kg ⁻¹)
rad [absorbed dose]	1	$\times 10^{-2}$	joule per kilogram (J kg ⁻¹) [gray (Gy)]
rem [equivalent and effective dose]	1	$\times 10^{-2}$	joule per kilogram (J kg ⁻¹) [sievert (Sv)]

^{*} Specific details regarding the implementation of SI units may be viewed at <http://www.bipm.org/en/si/>.

[†] Multiply the U.S. customary unit by the factor to get the international unit. Divide the international unit by the factor to get the U.S. customary unit.

FINAL REPORT

FOR

Sensing Fissile Materials at Long Range

Prepared under
GRANT NO. HDTRA-09-1-0042

Principal Investigator: Leslie Bromberg
(brom@psfc.mit.edu)
replacement for Dr. Timothy Antaya, who has retired.

Massachusetts Institute of Technology
77 Massachusetts Avenue
Cambridge, MA 02139
July 31, 2012

DISTRIBUTION STATEMENT A. Approved for public release; distribution is unlimited.

Leslie Bromberg
Leslie Bromberg

Table of contents

Table of contents	2
Objectives	4
Status of program.....	5
Staffing:.....	5
Financials as of 12/31/2011 (from second annual report)	5
Financials as of 1/31/2012	6
Executive Summary.....	7
Publications	8
A. Cyclotron Performance limits: Isochronous Flutter Field implications.....	10
A.1. Flutter Evaluation for VectorFields 3D Models.....	10
A.2 Minimum Flutter Requirements	15
A.3 Example: Solution for a 250 MeV, 1 mA isochronous cyclotron	17
Analysis.....	17
Magnetic Design Working Point Parametrics	18
Adjusted Magnetic Design Working Point Parametrics.....	21
B. Use of HTS Monoliths or Permanent Magnets for Field Modification and Flutter Generation.....	23
B.1 Introduction	23
B.2 Cyclotron requirements.....	25
B.3 Applications of HTS bulk to cyclotrons.....	26
B.4 Cyclotron Field Flutter	30
B.5 Beam Extraction.....	33
B.6 Use of permanent magnets with iron to provide the flutter.....	35
C. Cyclotron Prototype Magnet	37
C.1 Magnet design and construction	37
C.2 Test Coil Quench Analysis	40
Details.....	41
C.3 Magnetic Model of the Test Coil	49
Model	49
C.4 Test Coil Results	52
Newest Winding Pack Design.....	52
Model	52
Analyses.....	54
C. 5 Conclusion	57
D. HTS Potential for cyclotrons	58
Comments.....	60
E. Evolution of proton bunches in high intensity cyclotrons: a preliminary study on space-charge effects.....	61
E.1 Introduction	61
E.2 Geometrical effects.....	61
E.3 Physical models for the evolution of the proton bunch.....	61
A. Kinetic description.....	61
B. Fluid description.....	63

C. Electromagnetic fields	64
Summary	65
E.4 Starting fluid equations: Non-dimensional equations in moving frame	65
E.5 Ideal focusing model	66
A. Asymptotic analysis: Asymptotic expansion	67
B. Solving the equations	69
E.6 Numerical results	72
A. Numerical method	73
B. Numerical results: Cylindrical bunch	73
C. Numerical results: Elliptic bunch	74
E.7 Future plans	80
F. Ion Sources Of High Current Proton Cyclotrons	81
F.1 Hollow Cathode Discharges.....	81
F.2 Status and summary	82
F.3 Electron Cyclotron Resonance Ion Source.....	84
A. Source Design and Assembly	84
B. Power Supplies.....	85
C. Characterization of the Ion Beam	86
F.4 Theory of ion composition for low pressure discharges.....	88
G. Ironless Cyclotrons.....	92
G.1 Background.....	92
G.2 Iron-less or minimum-iron cyclotron concepts.	92
A. Magnetic shielding.....	92
B. Establishment of magnetic field shaping in synchrocyclotrons.	99
Discussion.....	104
G.3 Enabling features by ironless and iron-minimized cyclotrons.....	106
H. Phase-locked loop in	110
H.1 Background.....	110
H.2 Optimized system for accelerating beams in synchrocyclotrons.....	110
H.3 Beam sensors	115
H.4 Ion sources for synchrocyclotrons	119

Objectives

						Option year 1	Option Year 2
Compact High Field Cyclotron Development	Year	1	2	3		4	5
High Energy	VPAC Simulation	7 Tesla Baseline Compact 2GeV Cyclotron	Central Region & Extraction at 7T and 2 GeV	Coil Only Cyclotron Performance Limits		HTS Cyclotron Performance Limits	Ultimate Cyclotron Performance
	Testing	Rare Earth Magnetization Meas. At low temps.	Advanced Conductor Options	Prototype Coil Test		HTS Cyclotron Coil Test	Active Self Shielding Demonstration Test
	Modeling	Ferromagnetic Limits- Cyclotron Focusing	Coil Only Cyclotron Concepts- Design Limits	HTS Conductor Cyclotron Concepts		Self Shielding Coil-only Cyclotron Concepts	Ultimate Compact Cyclotron Design Concepts at high field
Particle Injection at Cyclotron Center	Year	1	2	3		4	5
High Intensity	Beam3D Simulation	High Field Axial Injection	Inflection Phase Space Evolution	ECRIS Injection Phase Space Evolution		Central Region Capture Phase Space	RF Acceleration at High Field Phase Space
	Testing	HCD Injection at 7 to 9 Tesla	HCD median Plane Inflection at High Field	ECRIS Inflection at High Field		Central Region Admittance at High Field	RF Acceleration Intensity Measurement at High Field
	Modeling	High Field Inflector	ECRIS Optimization	Ion Buncher Optimization		RF Acceleration Optimization	>250 KV Cyclotron Ion Injection

Statement from proposal:

The determination of the proton energy limit of a high field superconducting cyclotron shall be completed through a series of simulation, modeling, and testing tasks. The beam dynamics simulations should determine stability, injection, acceleration, and extraction requirements of compact high field cyclotrons for proton acceleration, while the field design studies should establish the distribution of currents in space required to generate such fields, and test should provide new data as required. Benchmarked cyclotron design codes and field simulation codes (MIT and commercial) shall be used to establish the highest cyclotron final energy that may be achieved in a superconducting isochronous cyclotron. The starting point will be a 2 GeV proton cyclotron at 6-7 T, where coils only or the already established saturated iron plus coil design will be used. Thesis students shall be included as essential participants in all of these activities.

The determination of the high intensity field shall be completed through a series of simulation, modeling, and testing subtasks. In order to assess the intensity frontier of iron free superconducting cyclotrons, we shall assemble and operate a high field cyclotron injection test stand. This test stand should include bright external proton ion sources operated at high voltage, an axial injection column that includes bunching and focusing elements, an inflector, a cyclotron central region (dee, dummy dee, RF acceleration), and beam phase space measurement devices. The principle aim shall be to measure the longitudinal and transverse phase space of bunched inflected proton beams as a function of intensity, voltage, and guide magnetic field. Thesis students shall be included as essential participants in all of these activities.

Status of program

Staffing:

The following people/fraction of effort are actively working on this program:

Staff:

Timothy Antana (retired)
Leslie Bromberg
Philip Michael
Joseph V. Minervini
Alexey Radovinsky
Donald Stracham
Makoto Takayasu
Richard Torti

Students:

Mark Artz GRA 100% (September-May 14)
Piesi Le GRA 100% (September-May 14)
Jeixi Zhang GRA 100% (full year)

There are no post-docs or faculty, although Prof. Jeffrey Freidberg and Antoine Cerfon (postdoc, with academic support) have been collaborating in this program.

Financials as of 12/31/2011 (from second annual report)

TOTAL PROJECT

Balance as of 12/31/11: \$205,938
Commitments as of 1/30/12: \$154,713
Balance projected to 5/14/12: \$51,225

OPERATIONS & PERSONNEL

Balance as of 12/31/11: \$115,361
Commitments as of 1/30/12: \$154,739
Balance projected to 5/14/12: (-\$39,377)

FAB ACCOUNT

Balance as of 12/31/11: \$90,603
Commitments as of 1/30/12: \$0
Balance projected to 5/14/12: \$90,603
Completed: 7/14/2012

Other information: Unbudgeted equipment requires advance approval, unbudgeted foreign travel requires advance approval (there is no foreign travel in the budget). The F&A rate is fixed at 68% for all five years.

Financials as of 1/31/2012

Status as of 1/31/2012

\$1,259,000.00 Obligated Funds

\$1,094,693.75 Expended

\$164,306.25 Balance

Executive Summary

It has been our goal to explore the design limits of cyclotrons. Two parameters that are being pushed in this program are beam energy and beam current. However, there are other concerns that we have explored besides energy and current:

- Size/weight of device
- Cryogenic requirements minimization
- Decreased complexity

Some of the main conclusions:

Minimum size of isochronous cyclotron is not determined by peak average field, but by flutter field requirements. The limits in the case that the flutter is generated by ferromagnetic materials has been determined, and machines designed upon those bases. The use of HTS bulk for making the flutter field has been analyzed, and it removes these limitations. We have also used permanent magnets and superconducting monoliths to improve the performance of iron in generating flutter for strong focusing.

The use of HTS materials for the main field have been investigated. We have determined that if the field is less than 18 T, high performance Nb₃Sn is sufficient. Only for very high fields, larger than 18 T, would HTS be useful.

We have built a model to investigate the space charge limitations of cyclotrons. The tool shows time dependent properties of the beam. Only equilibrium orbits have been performed during this program.

We have designed and built a compact Nb₃Sn coil to benchmark design codes. The coil has been tested and the results interpreted.

We have investigated ion sources. The Hollow Cathode Discharge is not suitable for cyclotron, because of durability. We have built and tested an Electron Cyclotron Resonance Ion Source (ECRIS) and modeled the ion source and the extracted beam.

We have investigated iron free designs. We have found, somewhat surprisingly, that it is straight-forward to generate the field profiles in the accelerating chamber of synchrocyclotrons, without iron. In addition, we have found out that it is possible to provide magnetic shielding without increasing the currents/field in the main coil.

We have identified the use of phase-locked loop technology for improving the performance of the RF acceleration in both isochronous and synchrocyclotrons.

Publications

The following publications have been published or submitted:

Three Master's degrees were awarded:

Mark A. Norsworthy

"Characterization of Selected Bulk rare Earth Metals for Compact Superconducting Cyclotrons"

Master of Science in Nuclear Science and Engineering

Massachusetts Institute of Technology

June 2010

Jordi Reig Armero

"Disseny d'una font de protons an al marc d'un experiment per desenvolupar ciclotrons compactes d'alta intensitat"

Master Degree in Mechanical Engineering

Escola Tecnica Superior D'Enginyeria Industrial De Barcelona

July 2010

Mark Artz

"Design and Testing of an Electron Cyclotron Resonance Heating Ion Source for Use in High Field Compact Superconducting Cyclotrons"

Master Degree in Nuclear Science and Engineering

Massachusetts Institute of Technology

August 2012

Papers:

J. Zhang, T. Antaya, R. Block, *Beam Dynamics Of A Compact SC Isochronous Cyclotron-Preliminary Study Of Central Region*, presented at the 2011 PAC meeting.

Three papers submitted for conferences:

L. Bromberg, J.V. Minervini, T. Antaya, M. Takayasu, A. Radovinsky, *Cyclotron optimization by the use of bulk High Temperature Superconductor*, submitted to the 2012 Applied Superconductivity Conference.

A. Radovinsky, L. Bromberg, J.V. Minervini, T. Antaya, M. Takayasu, *Design of a compact, high field, cyclotron using 2nd generation tapes*, submitted to the 2012 Applied Superconductivity Conference.

M. Artz, R. Torti, T. Antaya and L. Bromberg, *Evaluation and modeling of a hydrogen ECRIS for injection into cyclotrons*, submitted to IEEE ICOPS 2012

One Omnibus patent application (provisional):

L. Bromberg, J.V. Minervini, A. Radovinsky, P. Le, P. Michael and T. Antaya, *Ultra Light and Magnetically Shielded, High Current Compact Cyclotrons*, assigned to MIT (this provisional patent application has 3 components: ironless cyclotrons, phase-locked loop control for cyclotron acceleration, and use of HTS/PM for flutter generation in isochronous cyclotrons).

A. Cyclotron Performance limits: Isochronous Flutter Field implications

Models have been applied to 3D VectorFields models and analyses to investigate flutter requirements for the axial beam stability. We have determined that the need for substantial flutter limits the maximum magnetic field when ferromagnetic materials are used to create the flutter. **Alternative methods for generating the flutter, using high temperature superconductor monoliths, are presented in section A.**

The magnetic design has to address the isochronous field profile and the flutter simultaneously. A simplified analytical model (so far not supported by 3D VectorFields modeling) was developed and it shows that for the current isochronous field design point the field flutter, $\Delta B = B_{\max} - B_{\min}$, has to be in excess of 4 T. This appears to be excessive even for high saturation magnetization yoke materials. This calls either for using flutter coils in cold yoke, changing the working design point, or a combination of all of the above.

A.1. Flutter Evaluation for VectorFields 3D Models

The following equations were used to define and evaluate the target magnetic field

For Isochronous field

$$B_{av} = B_0 / \sqrt{1 - (r/\alpha)^2}$$

$$B_{av} = 1/2\pi \int [B_z d\theta \quad \{\theta, 0, 2\pi\}]$$

$$\alpha = R_{ex} / \sqrt{1 - (1/\gamma)^2}$$

where R_{ex} is the radius of extraction.

For Flutter field

$$n_{u_z^2} = n + f^2 (1 + 2 (r/A)^2)$$

$$n_{u_r^2} = 1 - n$$

$$n = -r / B_{av} * \Delta B_{av} / dr$$

$$f^2 = 1/2\pi \int [(1 - B / B_{av})^2 * d\theta, \{\theta, 0, 2\pi\}]$$

The working design point was defined by the following values of the parameters

$$\gamma = 1.26; R_{ex} = 0.4 \text{ m}; B_0 = 5.5 \text{ T}; A = 0.2 \text{ m}$$

A procedure has been developed for Opera Post-processor, which calculates “n” and “f²” as a function of radius, applied it to both models and postprocessed in Excel. The

result is that neither of these cases is even close to satisfying requirement, $\nu_z^2 > 0$. We have used BH curve for material identified as TAA-100804 Material, instead of the Iron BH curve used in the K250, which has been used before in previous models. Case 3D31g1, with exactly the same coils and yoke shape as in 3D31g and a BH curve per TAA-100804 Material, has been ran. Results for models 3D31g and 3D31g1 are shown in the left (Fig. A.1.a, A.2.a, A.3.a) and the right (Fig. A.1.b, A.2.b and A.3.b), respectively. The Model views and the B-M curves are shown in the first three rows of the Table. Respective saturation magnetization for models 3D31g and 3D31g1 is 2.05 T and 2.85 T as shown in Figs. A.3.a and A.3.b.

Figures A.4.a and A.4.b show that higher saturation magnetization of the yoke material leads to a higher isochronous field at all radii including the extraction point, which has been difficult. Adjusting the profile of the isochronous field at smaller radii can be achieved by increasing the axial gap between the valleys.

Figures A.5.a and A.5.b show B along the circumference at various radii. Figures A.6.a and A.6.b show ν_z and ν_r . They indicate that both designs don't pass the $\nu_z^2 > 0$ requirement¹. Figures A.7.a and A.7.b show additives in the formula for ν_z^2 . They clearly show that $f^2 (1+2 (r/A)^2)$ has to be much bigger to offset the negative n.

The main positive contributor is f^2 . For analytical estimates it is convenient to present it in the following form

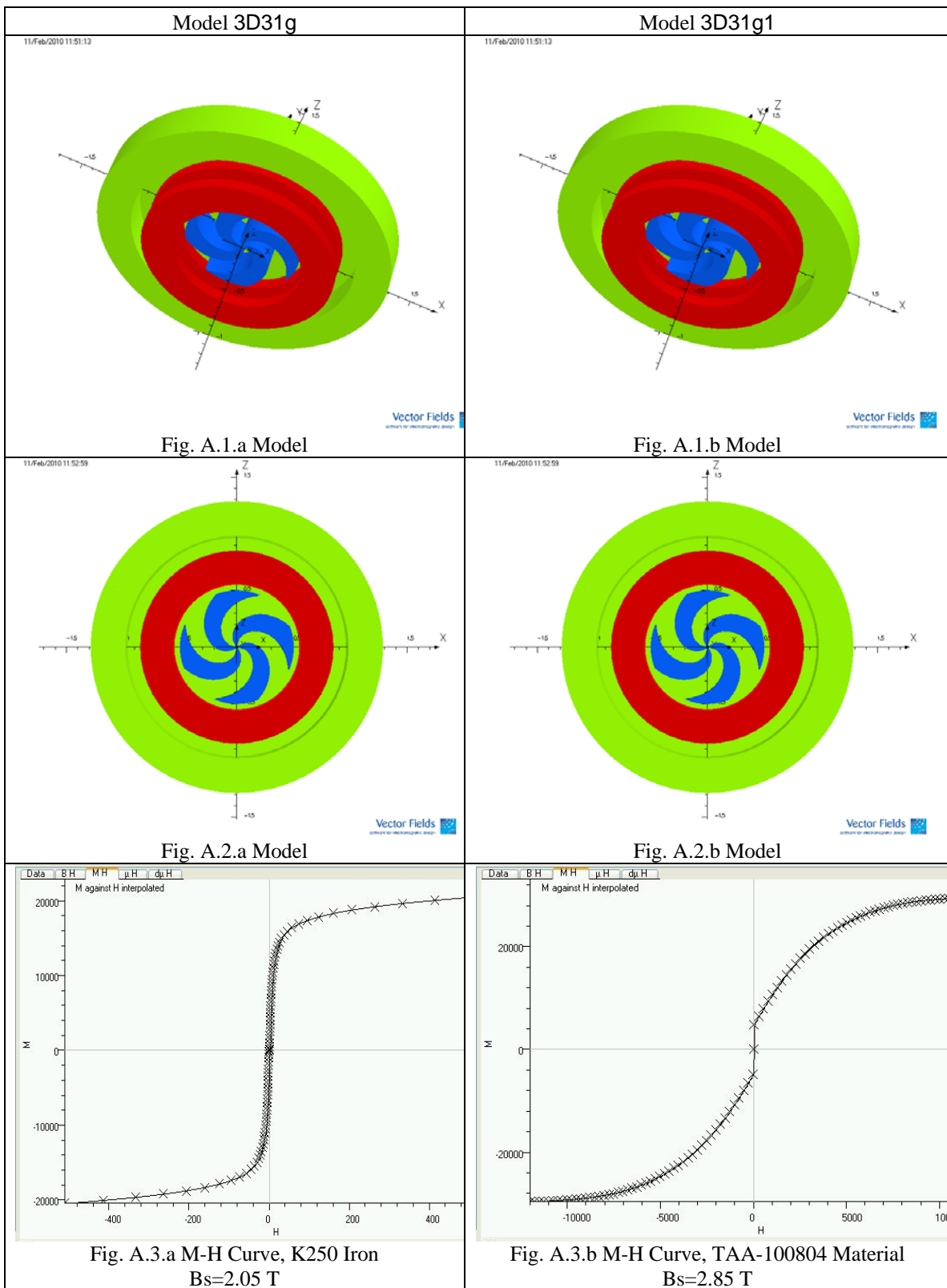
$$f^2 = s \cdot 0.25 (\Delta B / B_{av})^2$$

where $\Delta B = B_{max} - B_{min}$ and s is the shaping factor, which value is somewhere between $s=0.5$ for a sinusoidal wave and $s=1$ for a wave in a shape of a step function.

Figures A.8.a and A.8.b show ΔB vs. r calculated as a part of the VectorFields postprocessing procedure. Figures A.9.a and A.9.b show the shaping factor, s, derived from f^2 , B_{av} , and ΔB . Note that maximum ΔB is about 1.7 T and 2.4 T in models 3D31g and 3D31g1 respectively. A typical value of the shaping factor is less than 0.7. These observations will be used in the next section.

Conclusion 1. Magnetic design of an isochronous cyclotron requires simultaneous adjustment of both isochronous and flutter field. Creating a flutter field sufficiently strong to satisfy the minimum conditions for the vertical beam stability is a particularly challenging task, which for a given design point can be limited by physical limitations, such as for instance saturation magnetization of the yoke material.

¹ Zero portions of the ν_z curve represent points where ν_z^2 is negative and ν_z is imaginary



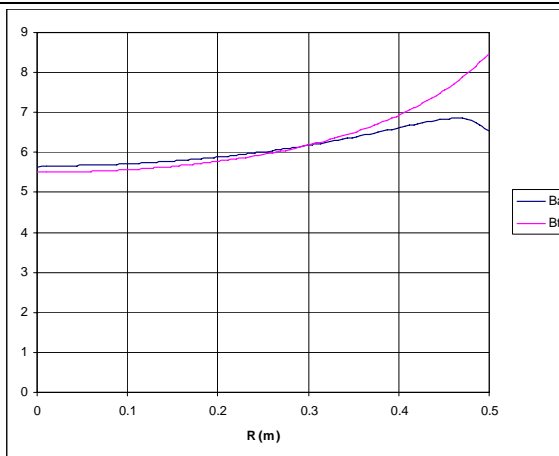


Fig. A.4.a Isochronous Modeled and Target Field

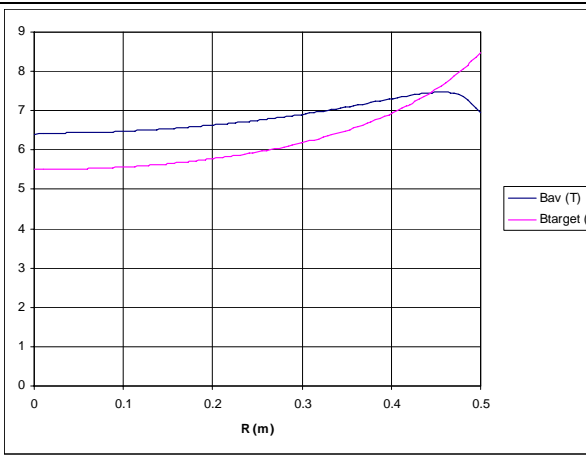


Fig. A.4.b Isochronous Modeled and Target Field

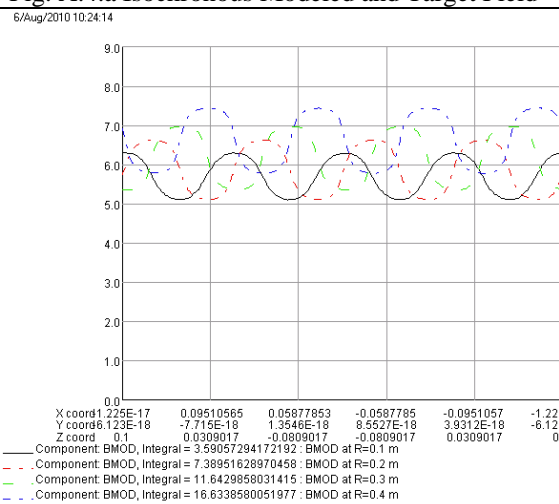


Fig. A.5.a $B(r*\theta)$ @ $r=0.1, 0.2, 0.3, 0.4$ m

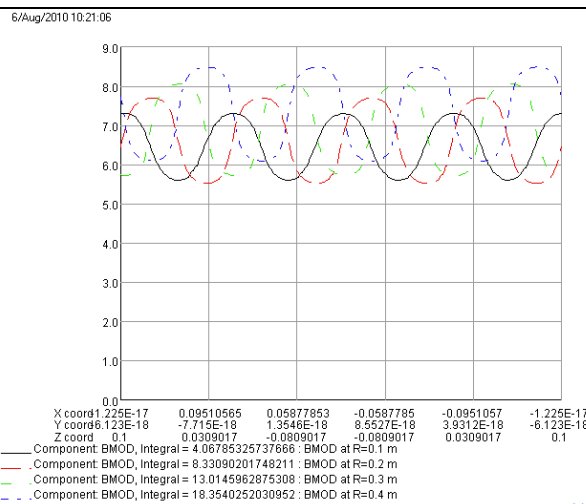


Fig. A.5.b $B(r*\theta)$ @ $r=0.1, 0.2, 0.3, 0.4$ m

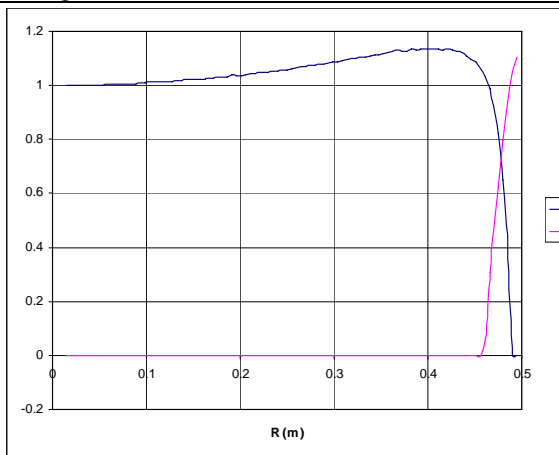


Fig. A.6.a ν_r, ν_z vs. r

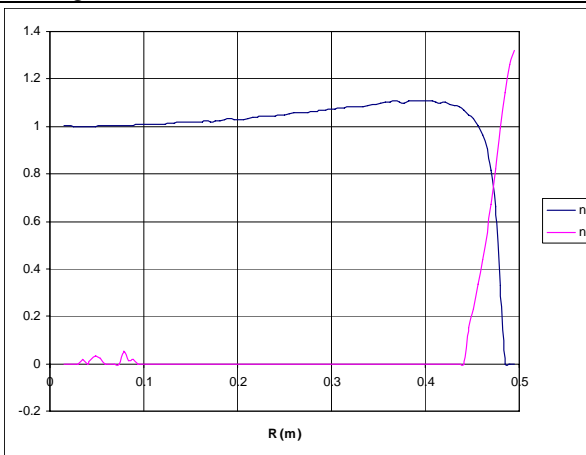


Fig. A.6.b ν_r, ν_z vs. r

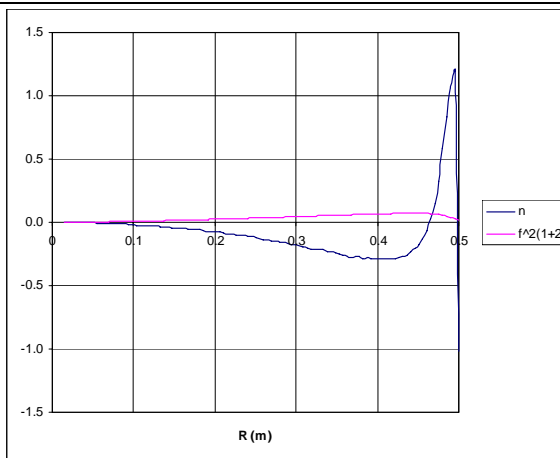


Fig. A.7.a ν_z^2 additives vs. r

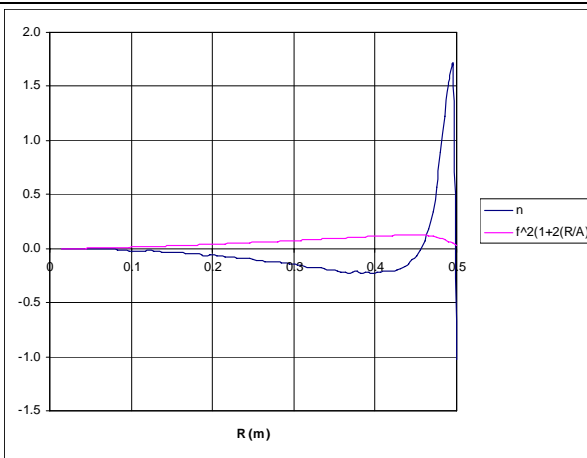


Fig. A.7.b ν_z^2 additives vs. r

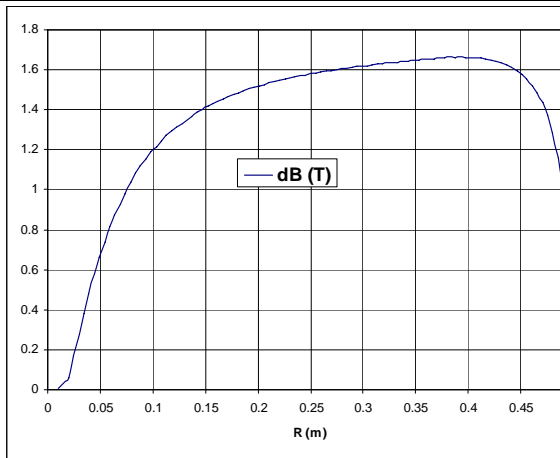


Fig. A.8.a dB vs. r

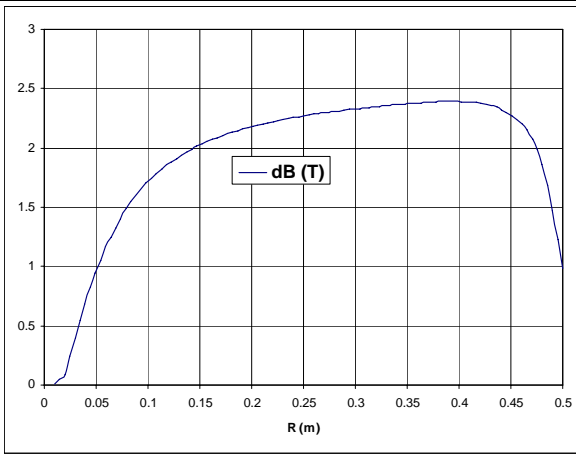


Fig. A.8.b dB vs. r

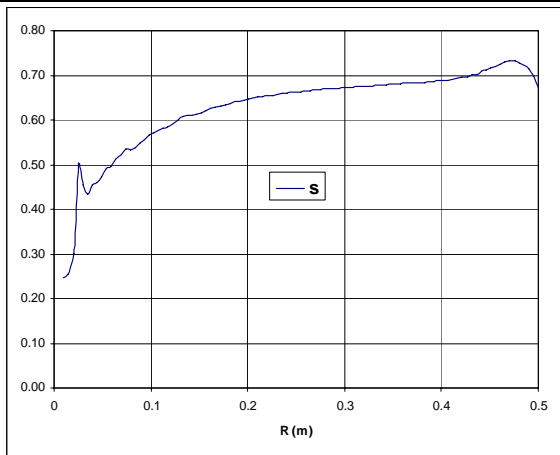


Fig. A.9.a Shaping factor s vs. r

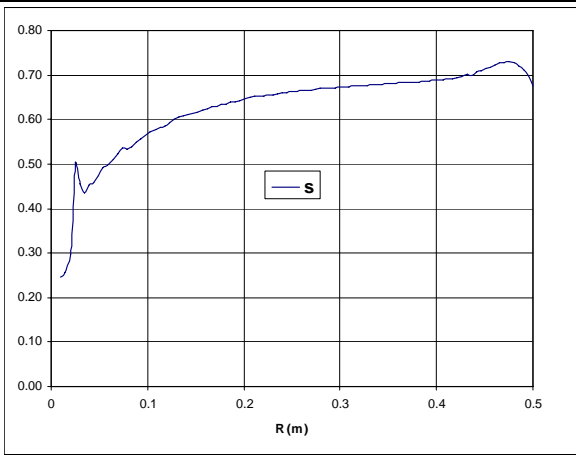


Fig. A.9.b Shaping factor s vs. r

A.2 Minimum Flutter Requirements

In this section we'll discuss minimum requirements for the flutter field for a given design point defined in this particular study by the following values of parameters specifying the isochronous field

$$\gamma=1.26; R_{ex}=0.4 \text{ m}; B_0=5.5 \text{ T}$$

These parameters and equations from Section 1 define the target isochronous field, $B_{av}(r)$. Condition $nu_z > \varepsilon$, where ε is a given safety margin, resolved with respect to ΔB defines minimum flutter, ΔB_{min} , required for the given target isochronous field

$$\Delta B > \Delta B_{min} = B_{av} / \sqrt{s \cdot 0.25} \cdot \sqrt{(\varepsilon^2 - n) / (1 + 2 \cdot (r/A)^2)}$$

Figures A.10.a – A.10.f show profiles of $\Delta B_{min}(r)$ calculated for several combinations of values of ε and the shaping factor, s . The Archimedes spiral constant is set to $A=0.2$.

Cases with $\varepsilon = 0$ just marginally satisfy condition $nu_z > 0$. Value $\varepsilon = 0.3$ is the recommended² one. The flutter shaping parameter, s , is given three values, 0.5, 0.7 and 1. Analyses of the data from VF models in Section A.1 show that the most realistic value is a little less than $s=0.7$.

We can expect that the target combination is $\varepsilon = 0.3$, $s=0.7$, which corresponds to Fig. A.10.d. For this case the maximum required $\Delta B=4.5 \text{ T}$ is at the extraction radius.

Even practically unrealistic cases with $s=1$ require ΔB in excess of 3.5 T.

Conclusion 2. In a magnetic design without flutter coils flutter happens due to the difference between the field in the valley and in the axial gap between the hills of a ferromagnetic yoke and ΔB is always smaller than the saturation magnetization, B_s , of the material of the yoke. As we need $\Delta B=4.5 \text{ T}$ the saturation magnetization has to be $B_s > 4.5 \text{ T}$. I don't know such materials. This means that either we need to use flutter coils or we need to reconsider the working design point of the isochronous field.

² TAA – e-mail, August 3, 2010

Required $\Delta B(r)$ for Current Design Point

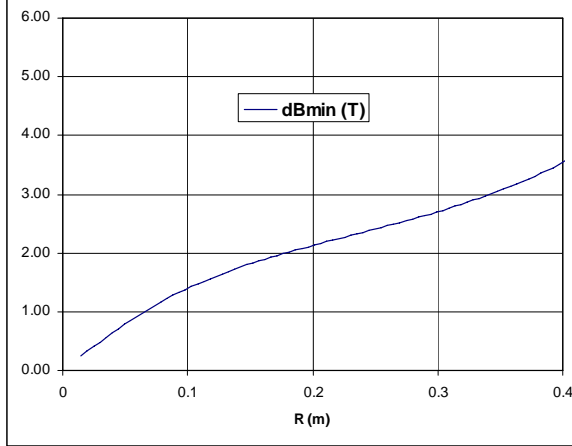


Fig. A.10.a $s=1, \varepsilon=0$

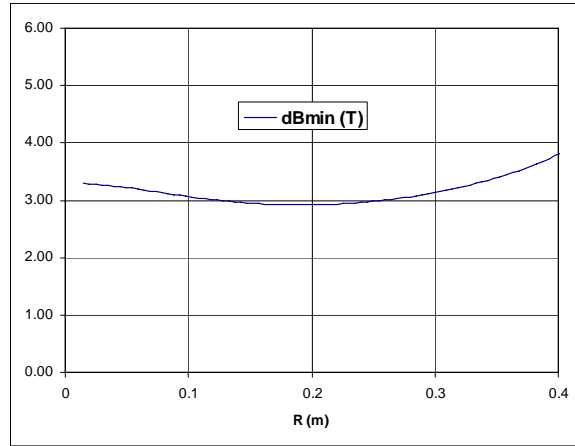


Fig. A.10.b $s=1, \varepsilon=0.3$

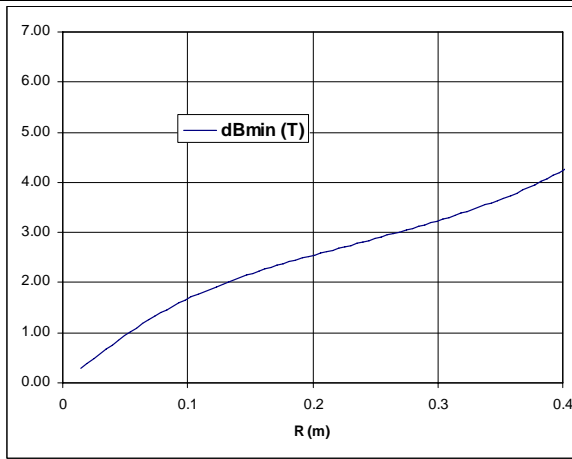


Fig. A.10.c $s=0.7, \varepsilon=0$

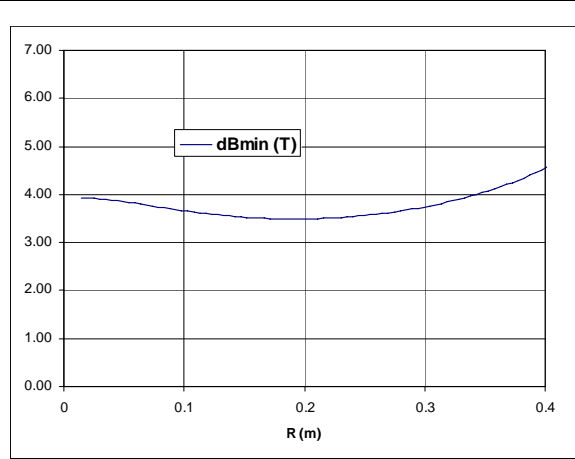


Fig. A.10.d $s=0.7, \varepsilon=0.3$

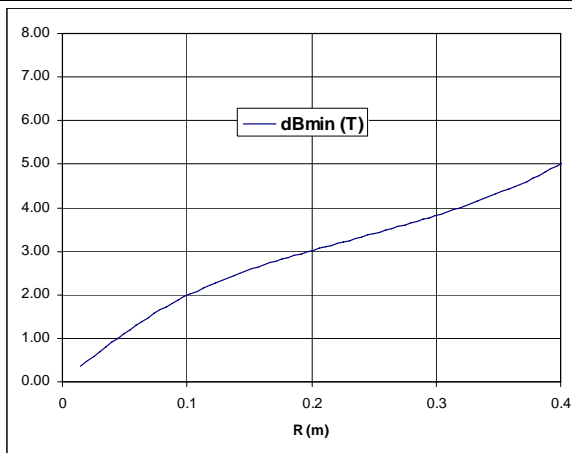


Fig. A.10.e $s=0.5, \varepsilon=0$

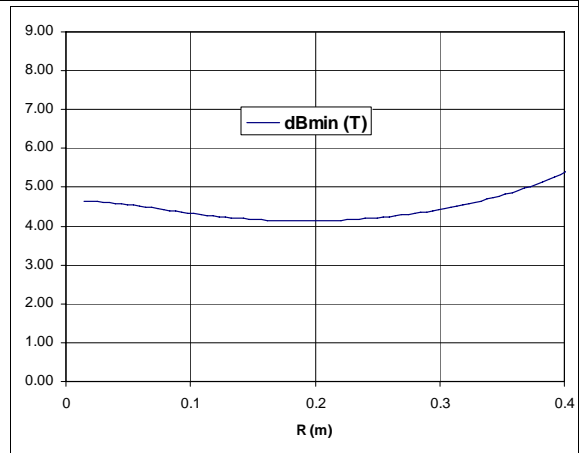


Fig. A.10.f $s=0.5, \varepsilon=0.3$

A.3 Example: Solution for a 250 MeV, 1 mA isochronous cyclotron

Equations have been derived to specify the working design point for a 250 MeV, 1 mA cyclotron using definitions of the isochronous field, the magnetic rigidity and the relativistic factor at extraction, as well as the peak-to-peak amplitude of the flutter field as parameters.

Analysis

General equations specifying magnetic field of synchronous cyclotron above have been used in this study. The general conclusion from above is that satisfying requirements to the isochronous field at the same time with creating a field flutter sufficient for the axial beam stability is a challenge limited, in particular, by a physical implementation of the flutter field. The required flutter field can be in excess of what can be achieved by using a hills-and-valleys geometry of a ferromagnetic yoke. Analytical and numerical results as well as most published papers on the subject show that this is particularly difficult to satisfy at the beam extraction point.

Let us assume that the magnetic design working point is defined by given values of the magnetic rigidity at extraction radius, $\mathfrak{R}_{ex}=R_{ex}*B_{ex}$, and the relativistic factor, gamma. Let us also assume that the flutter field is specified by the maximum achievable value of the peak-to-peak amplitude of the flutter field at extraction radius, ΔB_{ex} .

Let us consider the constraint, $nu_z^2 > \varepsilon$, at the beam extraction

$$(1) \quad nu_{z_{ex}}^2 = n_{ex} + f_{ex}^2(1 + 2(R_{ex}/A)^2) > \varepsilon^2$$

From equations ¹ we can derive that

$$(2) \quad n_{ex} = 1 - \gamma, f_{ex}^2 = s/4 * (\Delta B_{ex}/B_{ex})^2, B_{ex} = \mathfrak{R}_{ex}/R_{ex}$$

Formula (1) presumes that the shape of the hill is defined by an Archimedes spiral with a given value of constant, A.

Usual practice is to set

$$(3) \quad A = R_{ex}/2$$

In this case constraint (1) with account of (2) and (3) yields

$$(4.a) \quad R_{ex} > R_{ex_min} = \mathfrak{R}_{ex} / \Delta B_{ex} * 2/3 * \sqrt{(\varepsilon^2 + \gamma^2 - 1)/s}$$

In case (3) is not used and A is set as a free parameter R_{ex_min} is defined as a root of a quadratic equation

$$(4.b) \quad R_{ex} > R_{ex_min} = \sqrt{[-b + \sqrt{b^2 - 4ac}] / (2a)},$$

where

$$\begin{aligned} a &= 2(\Delta B_{ex} / (\mathfrak{R}_{ex} * A))^2, \\ b &= (\Delta B_{ex} / \mathfrak{R}_{ex})^2, \\ c &= -4/s * (\varepsilon^2 + \gamma^2 - 1) \end{aligned}$$

Once R_{ex_min} is found we can find major characteristic of the magnetic design from the following equations

$$(5) \quad R_{ex} = R_{ex_min}, B_{ex} = \mathfrak{R}_{ex} / R_{ex}, B_0 = B_{ex} / \gamma$$

Magnetic Design Working Point Parametrics

Let us apply formulas (4.a) and (5) to a cyclotron defined by

$$\gamma = 1.26, \mathfrak{R}_{ex} = R_{ex} * B_{ex} = R_{ex} * B_0 * \gamma = 0.4 \text{ m} * 5.5 \text{ T} * 1.26 = 2.772 \text{ T-m}$$

It is presumed that $\varepsilon = 0.3$, and that the flutter shaping factor, $s = 0.7$, the value typical for the numeric analyses using VF modeling.

Figures A.11 and A.12 show B_{ex} , B_0 and R_{ex} as a function of ΔB_{ex} .

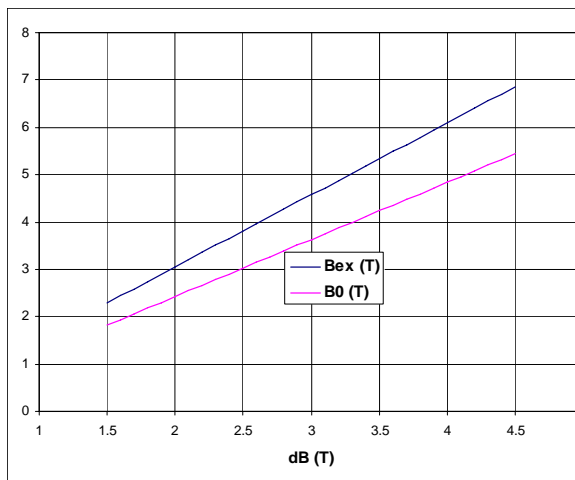


Fig A.11. B_{ex} , B_0 vs. ΔB_{ex}

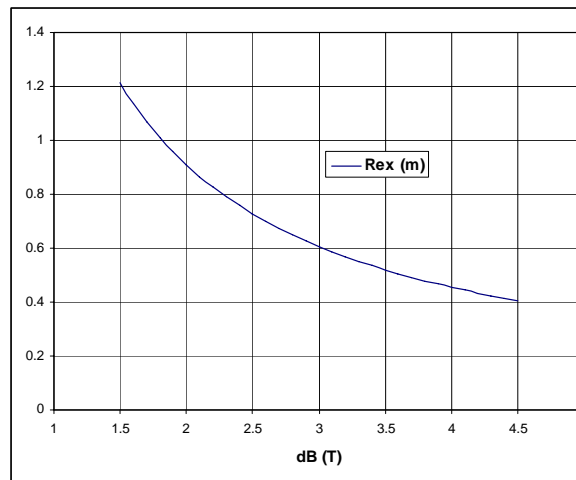


Fig A.12. R_{ex} vs. ΔB_{ex}

The following characteristic working points can be derived from these charts:

Case A: Extraction radius, $R_{\text{ex}}=0.4$ m, requires $\Delta B_{\text{ex}}=4.5$ T and corresponds to $B_0=5.44$ T and $B_{\text{ex}}=6.86$ T. This is the working point discussed in ¹. Its peculiarity is that physical implementation with $\Delta B=4.5$ T is problematic.

Case B: Flutter peak-to-peak amplitude $\Delta B_{\text{ex}}=1.8$ T as in most cases with an iron yoke corresponds to $R_{\text{ex}}=1.01$ m, $B_{\text{ex}}=2.74$ T and $B_0=2.18$ T.

Case C: Flutter peak-to-peak amplitude $\Delta B_{\text{ex}}=2.4$ T, which appears to be possible to achieve with the yoke of a material defined by BH curve, TAA-100804, supplied by TAA corresponds to $R_{\text{ex}}=0.76$ m, $B_{\text{ex}}=3.66$ T and $B_0=2.90$ T.

Case D: Flutter peak-to-peak amplitude $\Delta B_{\text{ex}}=3.5$ T, which we expect to achieve with the yoke of rare earth metals, Gadolinium, Holmium, etc., corresponds to $R_{\text{ex}}=0.52$ m, $B_{\text{ex}}=5.34$ T and $B_0=4.23$ T.

Figures A.13.a – A.13.d show ν_r and ν_z and Figs. A.14.a – A.14.d show B_{av} coincident with the target isochronous field as a function of radius. All plots curves are plotted for $0 < r < R_{\text{ex}}$. Note that in all Figures A.13.a thru A.13.d ν_z at extraction radius is equal $\varepsilon=0.3$

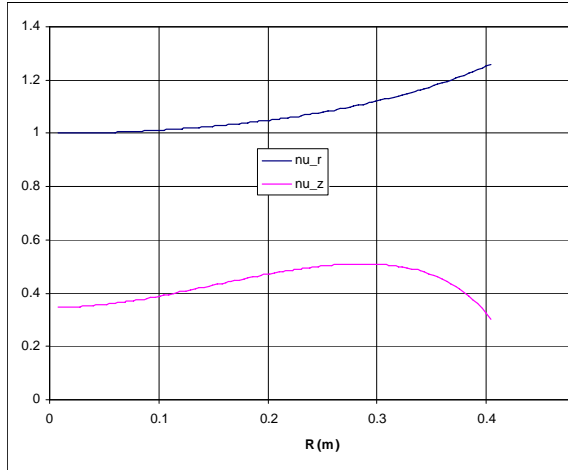


Fig A.13.a ν_r and ν_z for Case A

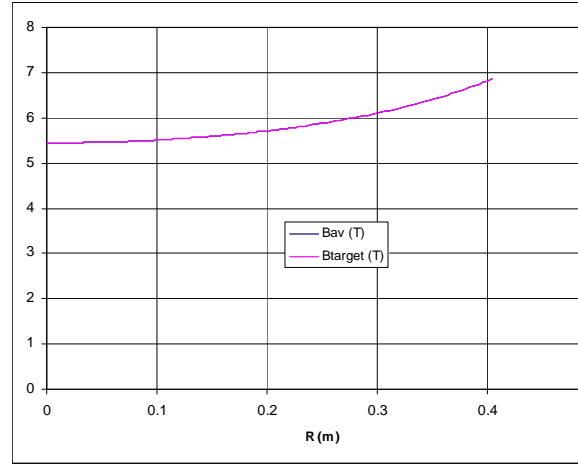


Fig A.14.a $B_{\text{av}}(r)$ for Case A

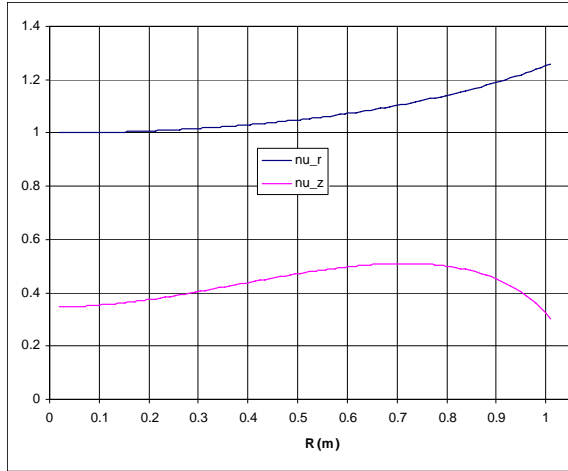


Fig A.13.b ν_r and ν_z for Case B

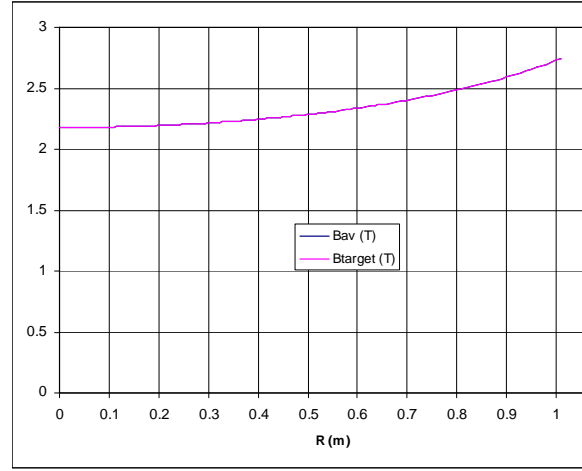


Fig A.14.b $B_{av}(r)$ for Case B

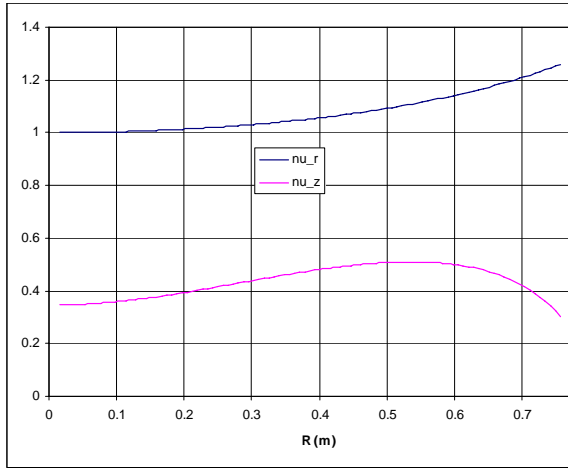


Fig A.13.c ν_r and ν_z for Case C

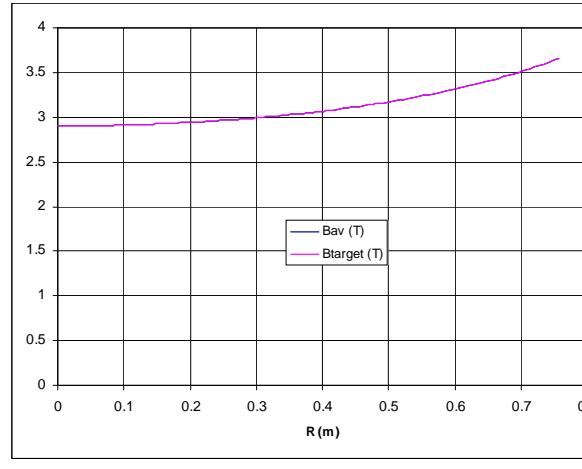


Fig A.14.c $B_{av}(r)$ for Case C

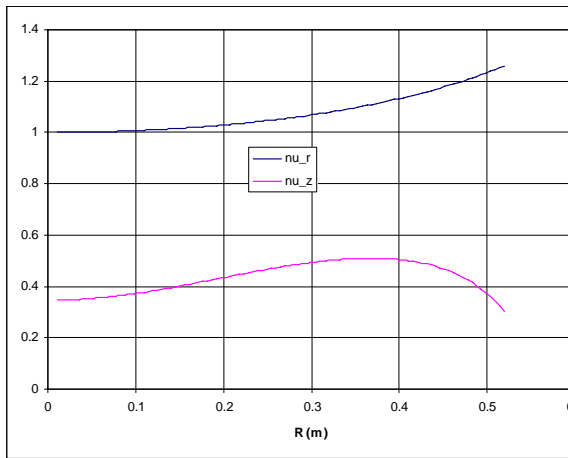


Fig A.13.d ν_r and ν_z for Case D

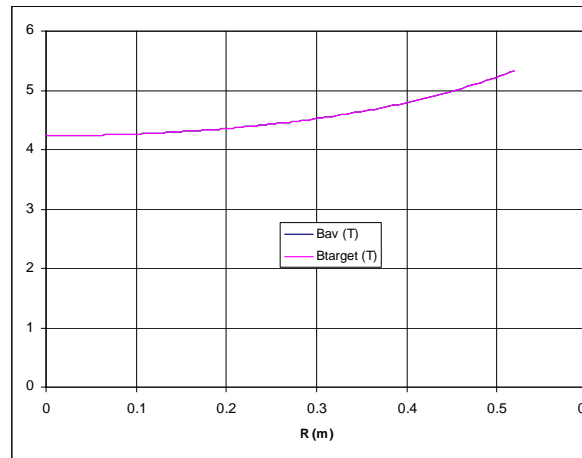


Fig A.14.d $B_{av}(r)$ for Case D

Adjusted Magnetic Design Working Point Parametrics

In the previous section we used gamma and magnetic rigidity, \mathfrak{R}_{ex} , scaled from the previous VF models. These values slightly differ from the theoretical values. For a proton accelerator we can use the following formulas

$$(6) \quad \gamma = 1 + T/E_0, \quad \mathfrak{R}_{ex} = m_0 c / e \sqrt{\gamma^2 - 1}$$

where $E_0 = 938$ MeV, $m_0 = 1.660 \times 10^{-27}$ kg, $c = 2.9979 \times 10^8$ m/s, $e = 1.602 \times 10^{-19}$ C.

For the target kinetic energy of $T = 250$ MeV

$$\gamma = 1.266, \quad \mathfrak{R}_{ex} = 2.414 \text{ T-m},$$

which is slightly different from the values in the previous section.

Figures A.15 and A.16 show B_{ex} , B_0 and R_{ex} as a function of dB_{ex} for the new set $\{\gamma, \mathfrak{R}_{ex}\}$

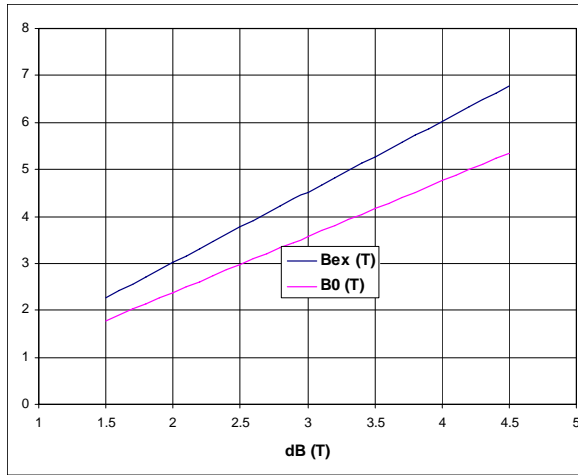


Fig A.15. B_{ex} , B_0 vs. dB_{ex}

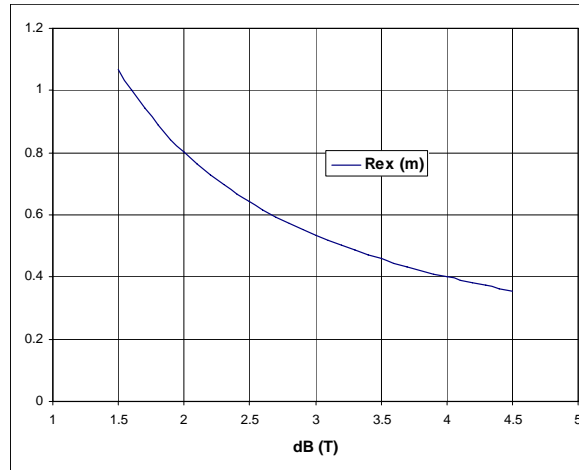


Fig A.16. R_{ex} vs. dB_{ex}

Adjusted characteristic working points derived from these charts are

Case A': Extraction radius, $R_{ex} = 0.4$ m, requires $dB_{ex} = 4.0$ T and corresponds to $B_0 = 4.76$ T and $B_{ex} = 6.03$ T. This is analogous to the working point discussed in ¹. Physical implementation with $dB = 4.0$ T is problematic.

Case B': Flutter peak-to-peak amplitude $dB_{ex} = 1.8$ T as in most cases with an iron yoke corresponds to $R_{ex} = 0.89$ m, $B_{ex} = 2.71$ T and $B_0 = 2.14$ T.

Case C': Flutter peak-to-peak amplitude $\Delta B_{ex}=2.4$ T, which appears to be possible to achieve with the yoke of a material defined by BH curve, TAA-100804, supplied by TAA corresponds to $R_{ex}=0.67$ m, $B_{ex}=3.62$ T and $B_0=2.85$ T.

Case D': Flutter peak-to-peak amplitude $\Delta B_{ex}=3.5$ T, which we expect to achieve with the yoke of rare earth metals, Gadolinium, Holmium, etc., corresponds to $R_{ex}=0.46$ m, $B_{ex}=5.27$ T and $B_0=4.16$ T.

B. Use of HTS Monoliths or Permanent Magnets for Field Modification and Flutter Generation

B.1 Introduction

Bulk HTS materials have been made from several materials and in many shapes. Presently, both BSCCO 2212 and YBCO-123 materials are available. 2212 is more developed, because of applications as current leads, and more recently, as components for fault current limiters. 2212 is available from several manufacturers, such as Nexans in Europe, either as rods, cylinders or as plates. While its properties are lackluster at 77 K, they are very good at 20-30 K and below.

Bulk YBCO is being developed mainly as materials to be used in bearings, in the US (Boeing), Europe (Nexans) and Japan (ISTEC), among others. The characteristics of this material are nothing less than spectacular, at temperatures up to 60-65 K. YBCO has limited current density capabilities at 77 K; however, the material produced by the Houston group [Weinstein] with neutron irradiated monoliths, has good performance at 77 K. The material is not good for high field magnet applications, unless they are subcooled.

The most impressive performance of YBCO pucks has been a 17 T magnet at 29 K without a background field [M. TOMITA and M. MURAKAMI, *High-temperature superconductor bulk magnets that can trap magnetic fields of over 17 T at 29 K*, *Nature* **421** 517 (2003)]. Weinstein has 2 T at 77 K in a 20 mm monolith. And Cardwell has over 1 T at 77 K in a 25 mm monolith [D. A. Cardwell, W. K. Yeoh, S. K. Pathak *et al.*, The Generation Of High Trapped Fields In Bulk (Re)BCO High Temperature Superconductors, Y-H Shi1, AIP Conference Proceedings, v 1219, p 397-406, 2010].

For 2212, the MIT group has built a 3 T magnet at 4 K, and a 1 T insert in a 19 T background [Bromberg, private communication].

These materials are available at costs of 15 €/cm² (150 k€/m²).



- ♦ Top Seeded Melt Grown mono domain bulk parts for magnetic applications
- ♦ Actual batch size 64 samples in one furnace.
- ♦ Standard sample size 40 × 40 × 14 mm³
- ♦ Maximum sample size 60 × 60 × 16 mm³

 nexans

HTS Bulk Material II



Multi seeded YBCO plates
200 mm

Cylinder
target



Frank N. Werfel, Dr. rer. nat. habil.
Adelwitz Technologiezentrum GmbH (ATZ)
Rittergut Adelwitz
04886 Arzberg- Adelwitz, Germany
Phone ++49 34 222 45 200
werfel@t-online.de
www.atz-gmbh.com

 ATZ

Figure B.1. Commercially available elements with HTS made with Y(Re)BCO materials.



Figure B.2. Photographs of HTS tubes made from 2212 tested at MIT.

HTS materials have been considered for modification of magnetic fields that are generated by relatively simple coils, for minimization of field ripple in tokamaks and providing the external rotational transform in stellarators.

B.2 Cyclotron requirements

Cyclotrons have specific requirements that make good opportunities for the use of HTS bulk material.

One class of cyclotrons, the isochronous cyclotron, requires a magnetic field profile that increases with radius to accommodate for relativistic effects of the accelerated particles. This field profile results in unstable orbits, unless some form of focusing is used. Focusing is provided by azimuthal variations of the magnetic field, known as “flutter”. In low field machines, the use of ferromagnetic sectors to provide the field flutter is used. However, as the field increases, the possibility of using ferromagnetic fields results in less attractive machines, as the ferromagnetic material become saturated at magnetic flux densities of ~ 2 T for common magnetic materials and ~ 3 T for exotic materials (Holmium and other rare earths).

Other potential application of bulk material in high field cyclotrons is for injection. In most designs, the ion beam is generated outside of the device and injected axially. Inflectors are used for bending the beam and introducing into the midplane accelerating region. The high magnetic field makes the inflector design difficult. Either high accelerating energies of the ions being injected, or miniature inflectors (for bending the ions) are required. These inflectors require that the equivalent

electric radius and the magnetic Larmor radius are comparable. Since the Larmor radius is relatively small for modest energies and high fields, the electric radius needs also to be relatively small, making it difficult to manufacture, as the power densities are high.

Finally, HTS monoliths can be used for beam extraction. The use of magnetic perturbations for affecting the orbits near the extraction region are usually employed. It is difficult to make effective magnetic perturbations by the use of ferromagnetic materials.

Thus, the use of materials with high diamagnetic properties is highly desirable.

B.3 Applications of HTS bulk to cyclotrons.

High field, cryostable, highly complex magnet field topologies can be generated using HTS materials. The diamagnetic properties of the bulk HTS material can be used to provide simple mechanisms for providing field-shaping in cyclotrons: in the injection region, the central region (focusing) and the extraction region. The absence of the need for copper, insulation, current leads, and even structural elements inside the HTS elements allows for very high current densities, much higher than allowed by conventional superconducting strands or tapes, as is common for making superconducting magnets. In the above mentioned applications of HTS to cyclotrons the most important parameter is field gradient. The very high current densities of these materials can provide very high field gradients: in magnetic circuits, the curl of B (a measure of the field variation in space) is proportional to the current density.

Since the HTS monoliths require no insulation or copper for stability/quench protection, the radiation fluence is limited by the HTS material itself. Due to the high temperature of operation of the HTS compounds, nuclear heating is also very much relaxed: at 50 K (for YBCO) it is possible to remove more than one order of magnitude higher cryogenic loads than at 4 K, for the same refrigerator power. In addition, irradiation damage limits on HTS, and YBCO in particular, are no lower than for Nb_3Sn .

These materials need to be cooled to relatively low temperatures, but not necessarily near 4 K as is needed for conventional low temperature superconductors.

The field cancellation or gradient can be adjusted either geometrically (radius, thickness, separation between the two HTS monoliths), or it can be adjusted by varying the temperature of the superconductor.

Electromagnetic/thermal/structure models for the HTS materials have been developed that are based on the Bean model of superconductivity. We have used a simple model that represents the electrical resistivity of the material when the current density is larger than critical and flux penetrates into the superconductor, as modeled by Coombs [Min Zhang and T A CoombsCampbell, *3D modeling of high-Tc*

superconductors by finite element software, Supercond. Sci. Technol. **25** (2012)]. Figures B3 and B4 show illustrative calculations of the use of bulk material for the injection region, using the simple model. It is assumed that the HTS materials are about 2 cm in radius. The cyclotron field, in the absence of the HTS pucks, is about 9T. There is a 10 mm diameter central hole in both pucks to allow for ion beam access; the size of central hole can be substantially increased without changing the results substantially. Clearly, the magnetic field cancellation is sufficient for introduction of ions into the cyclotron by bending the ions in this region of low magnetic field. The cylinders have a hole through the center that allows for the beam to go through. The superconducting pucks can be placed either in the vacuum of the beam, or outside the beam transport chamber, but need to be kept at cryogenic temperature.

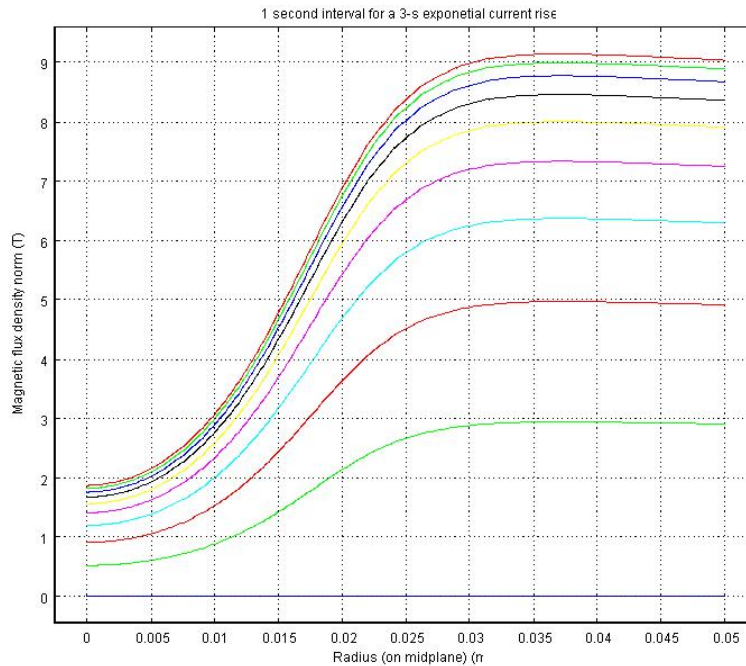


Figure B.3. Illustrative calculations of time-dependent magnetic flux density on the midplane of the cyclotron, as a function of radius, for an external field that increases from 0 to 9 T, for various times. The beam is injected through the center of the monoliths.

The field profile is shown in Figure B.4.

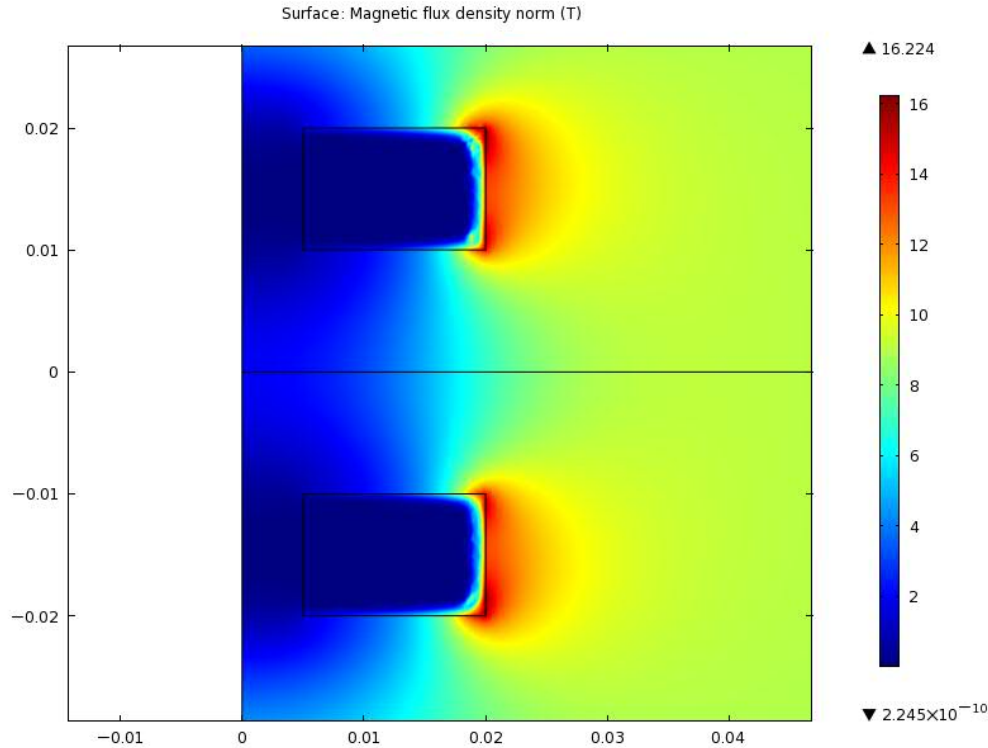


Figure B.4. Field profile along a vertical plane through the axis of the cyclotron, in the region next to the HTS monoliths, at the end of the field ramp-up.

As the temperature increases, both the critical current and the field gradient decrease. By adjusting the temperature of the superconductor, it is possible to adjust the current in the pucks, and thus, the field cancellation. It should be noted that if the field exceeds a given amount such that the flux penetrates throughout the bulk, when the field is removed there will be trapped magnetic field in the pucks. If unwanted, these remnant magnetic fields can be eliminated by warming up the pucks above the critical temperature and recooling afterward. They need to be warmed up to temperatures where the critical current/critical fields are small or even where the entire puck is non-superconducting. In the case where the flux does not penetrate fully there will be currents flowing in the superconductor, but in opposite direction in different regions, and with no net magnetic field.

If there is flux creep in the superconductor, there is heating. However, unless operating at or near 4 K, the heat capacity of the bulk HTS material is enough to prevent substantial temperature increase. It also should be noted that the magnetic field should be raised slowly to prevent flux jumping, where a sudden substantial change in current distribution in the superconductor occurs, driven by the unstable situation where flux creep heats the superconductor, decreasing its current carrying capability and thus allowing a cascading flux penetration. However, even these large flux jumps terminate well before the entire sample is non-superconducting, and results in field trapping inside the superconductor, although in a rather uncontrolled condition. Large flux jumps are observed at fast magnet charging rates;

however, with low magnet charging, there are no flux jumps, although there is flux creep.

Any heating needs to be removed from the HTS material. Sources of heating are thermal radiation from the warm background, conduction through supports, convection from residual gas, and heating during transients in the main magnetic field, which are usually infrequent. To cool the monoliths, either conduction cooling or bath cooling in either gases (He, Ne, depending on the temperature), or liquids (H₂ or Ne, again depending on the temperature), is required.

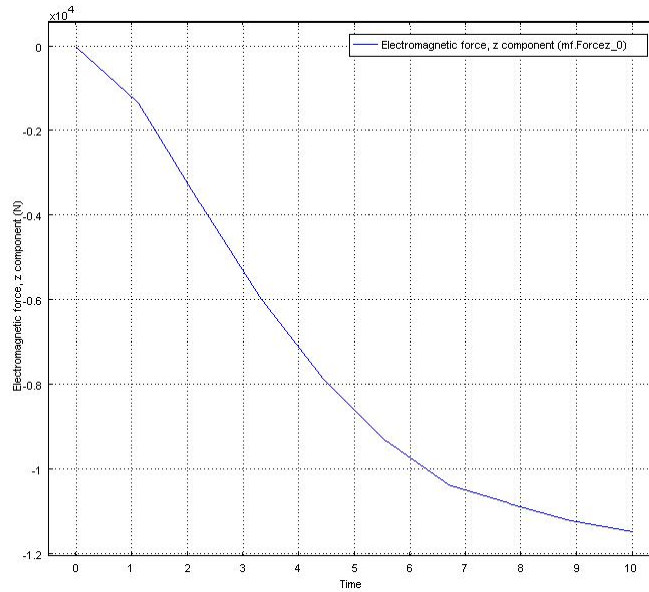


Figure B.5. Axial force as a function of time, for the cases shown in Figures C3 and C4.

The pucks have large mechanical loads that need to be supported. The loads internal to the monoliths, generated by the interaction between the local magnetic field and the internal current, place the material under compression. But there can be large net loads on the pucks, as well. For the case illustrated in Figures C3 and C4, the time dependence of the load is shown in Figure B.5; the force is acting to bring the two pucks together. It is best to support these loads from the cyclotron hemispheres above and below the midplane, as opposed to through the midplane, in order to keep this region clear for the beam chamber.

The magnetic field profile can be designed by selecting the proper dimensions of the pucks and the proper separation.

In order to achieve adequate injection, ions need to be accelerated in a few cycles to energies that are sufficiently high to push the ion orbit that correspond to this energy outside of the affected region. Adjustment of the radius of the monoliths, the

temperature of the monoliths, the SC properties of the monoliths (type of monolith, superconducting properties) and gap between the puck could be used. In addition, more than one set of monoliths could be used.

B.4 Cyclotron Field Flutter

A different application of the superconducting monoliths is the generation of field flutter in cyclotrons. The biggest challenge of magnetic design of compact isochronous cyclotron is achieving sufficient flutter for strong focusing. One of the optional solutions lies with the use of rare earth magnetic materials, *e.g.* holmium or gadolinium, as the spiral pole tip material. Although these materials exhibit a magnetic saturation much greater than low carbon steel, they must be maintained at a cryogenic temperature to achieve these high values. Another option is using superconducting coils wound around the spiral steel pole pieces to achieve a satisfactory degree of flutter, or using superconducting monoliths, as described below.

The main advantage of the two approaches described below is the elimination of the field constraints in cyclotrons, which are difficult to design at high fields with the use of saturated ferromagnetic materials.

a. Use of superconducting monoliths for providing the pole-shaping.

Some of the HTS materials, BSCCO 2212 in particular, can be made in the form of sheets. YBCO, with higher properties, is difficult to make in large areas, although some groups have been making wider sheets by joining, during manufacturing, several monoliths, with adequate current transfer capabilities between pucks (each puck manufactured from a single seed, or from multiple seeds. The size of the available plates, however, is somewhat limited at the present time. Plates as large as 20 cm by 20 cm, 1 cm thick, can be made commercially. The size of these plates may be sufficient for applications in compact cyclotrons. Multiple plates could be used in larger cyclotrons.

The shape of the HTS monoliths can be made to best suit cyclotron requirement. The magnetic sectors can be made with radially oriented edges of the HTS monoliths, as shown in Figure B.6 or they can be made with radial dependence, in order to provide additional flexibility, as shown in Figure B.7. As in conventional cyclotrons with magnetic sectors, the monoliths would be both above and below the beam chamber, arranged symmetrically.

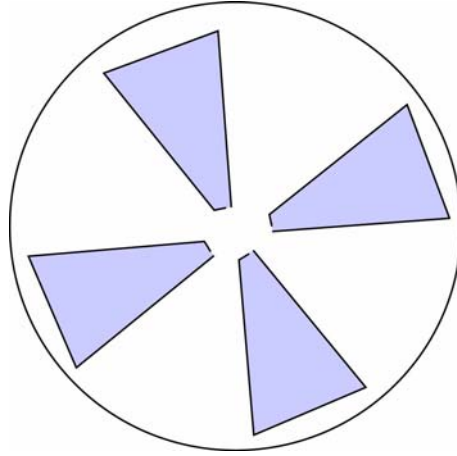


Figure B.6. Schematic diagram of a system with HTS bulk serving as diamagnets for providing flutter field in cyclotrons. Illustrative case with 4 sections per revolution shown.

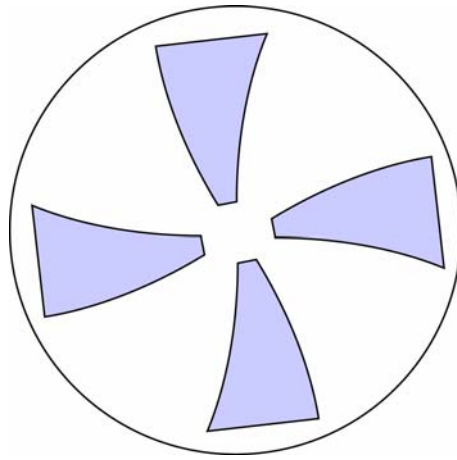
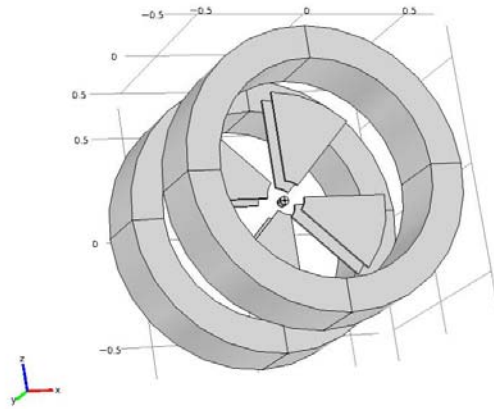
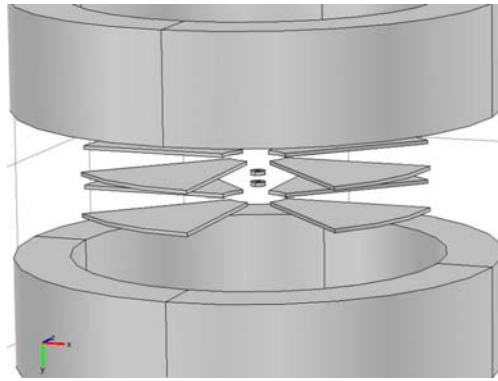


Figure B.7. Variation of arrangement in Figure 6, indicating the flexibility for shaping the HTS monoliths. Illustrative case with 4 section per revolution shown.

In opposition to the ferromagnetic materials, the HTS monoliths behave as diamagnetic materials, excluding the flux. The magnetic flux density, as a consequence, looks very different from the case of the ferromagnetic materials. In particular, the field gradients can be made larger and more concentrated.



(a)



(b)

Figure B.8 a and b. Illustrative concept of the use of HTS monoliths in cyclotrons for the central region (for injection) and for generating the flutter field. Illustrative case with 4 sectors per revolution is shown.

As opposed to the system for canceling the magnetic flux density near the axis for ion injection, the monoliths that produce the flutter field will experience large torque loads, in addition to large forces. These loads (both torques and forces) will be supported by the cyclotron structure, away from the beam aperture in the midplane of the machine.

Figure B.8 shows an illustrative case with 4 sectors. The Figure also shows the injection monoliths located along the axis of the cyclotron.

Different material can be used for the poles. If a ripple of about 4 T is needed (at the pole tip), YBCO monoliths can reach this level of field at about 50 K, while BSCCO materials need to be cooled to about 35 K.

In the approach describe above with HTS monoliths, it is necessary to have a central pole assembly contained within a cryostat. This is also the case when other

superconducting material (wires, tapes) is used, or when cryogenic high-saturation field materials are used. To maintain a small size of the cyclotron the gap between the hills made of Holmium and maintained at the cryogenic temperature has to be of the order of only 3 cm. The use of a pole cryostat requires extra axial space to maintain the vacuum, conduction, and thermal radiation separation needed to maintain a low cryogenic temperature. The extra space required increases the pole gap, thus also reducing the flutter field. The challenge is decreased by the use of high temperature superconductors, operating at fields substantially higher than 4 K, and even 30 K.

B.5 Beam Extraction

Field perturbations in the region near the field extraction are useful. The use of HTS materials can produce substantially higher gradients in the field than possible with permanent magnets or by ferromagnetic materials.

There are two functions for which the HTS elements are useful. The first function is in providing a large field perturbation near the last confined particle orbit in order to provide beam separation that allows for beam extraction. The purpose of the field cancellation near the extraction region is to increase the betatron oscillation of the ions, by forcing the ions to rapidly move away from the equilibrium orbit into orbits where they can be extracted because of large separation between the orbits. This requires that the particle bunches remain tightly packed, to provide for the possibility of insertion of field canceling elements.

The second function is to further cancel the magnetic fields in the extraction channel. Both functions can be coupled.

In some instances, the monoliths that can be manufactured are of smaller size than the one desired for the present application. It is possible to put them together in arrays in order to resemble the desired geometry. Either a single layer of pucks can be envisioned, or multiple layers.

Cylindrical pucks can be set in the array as either a Cartesian arrangement, or in a triangular arrangement, as shown in Figure B.9a or b.

The multiple layers of monoliths can have the monoliths stacked on top of each other, or they can be staggered, as shown in Figure B.10.

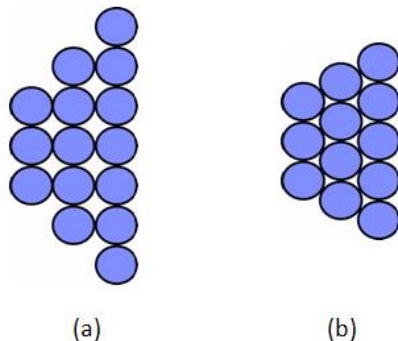


Figure B.9. Arrangement of cylindrical monoliths in a Cartesian array (a) or triangular array (b).

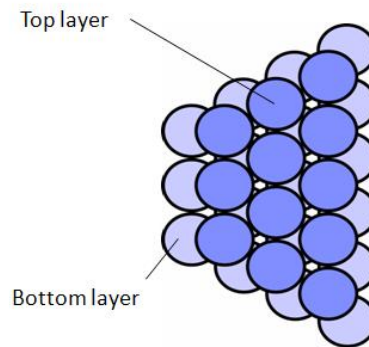


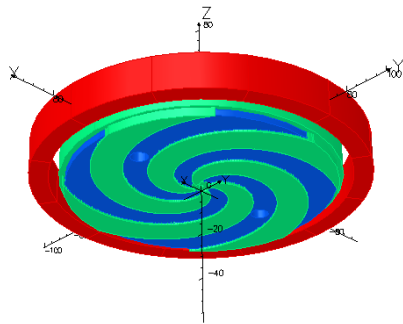
Figure B.10. Schematic having 2 layers of monoliths, staggered.

An alternative approach is described below that can use room temperature elements.

B.6 Use of permanent magnets with iron to provide the flutter

One of the elements of this invention is the use of permanent magnets and iron to produce the flutter, as depicted in Figures B11-B17. This aspect of the invention consists of a background field produced by a superconducting coil in a cryostat combined with a room temperature insert in the bore shown in Figs. B13 and B14 respectively, with a superconducting coil shown in Figure B.12. Only half of the magnetic system is shown; there is a symmetrical unit below that shown in Figures B11-B16. The insert has two elements: the spiral iron hills shown in Figure B.13, which amplify the field of the background coil, and the permanent magnets, shown in Figure B.14 which fill the space between the iron hills (*i.e.* the valleys is filled with permanent magnets), polarized oppositely to the field of the coil. Iron hills provide a field change of 1.7 T and permanent magnets give about 0.3 T in the opposite direction. Illustrative calculations of the use of combined iron and permanent magnets is shown in Figure B.16; together the iron and the permanent magnets produce a step of up to 2 T, which, given the same mid-plane gap, comparable to the fields that can be produced with cryogenic holmium hills alone, but without the cryogenic environment and the increased gap (the increased gap degrades both the change in field and the flutter field shaping factor). With the Fe+PM arrangement the bore is at RT and no additional gap is needed.

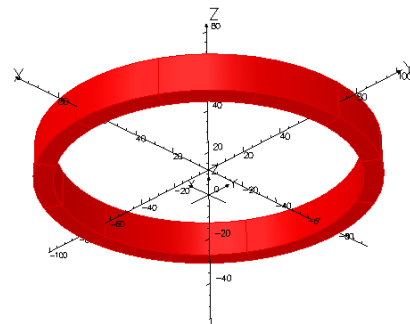
26/May/2012 16:57:14



Opera

Figure B.11 Isochronous Cyclotron. EM Components. Upper Half

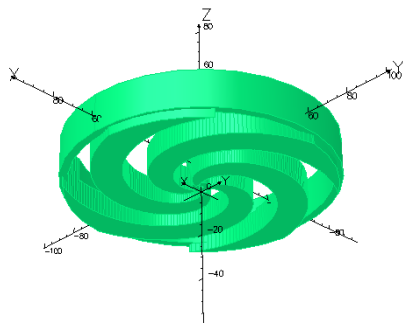
26/May/2012 17:01:17



Opera

Fig B.12 Isochronous Cyclotron. SC Background Field Coil. Magnetization in Z+.

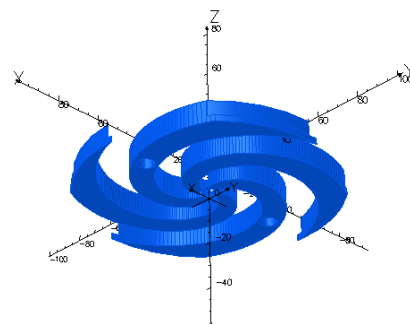
26/May/2012 16:58:36



Opera

Figure B.13 Isochronous Cyclotron. RT Fe Hills. Magnetization in Z+.

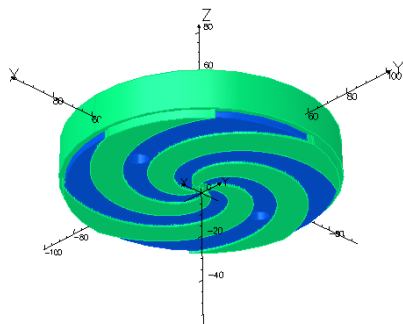
26/May/2012 16:59:50



Opera

Figure B.14 Isochronous Cyclotron. RT PM Valleys. Magnetization in Z-.

26/May/2012 17:02:14



Opera

Figure B.15 Isochronous Cyclotron. RT Bore Insert Comprised of Fe Hills and PM Valleys.

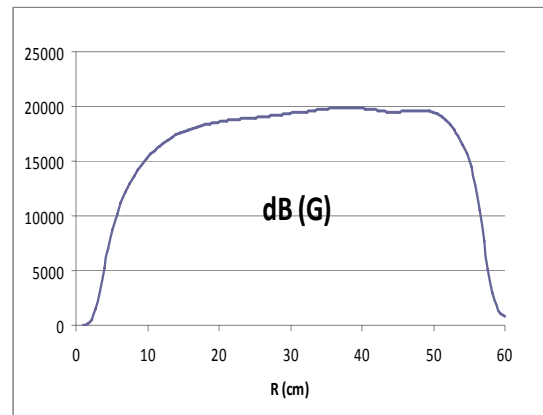


Figure B.16 Isochronous Cyclotron. $dB = B_{\max} - B_{\min}$ vs. radius

C. Cyclotron Prototype Magnet

C.1 Magnet design and construction

We have built and tested a superconducting coil for a cyclotron. The coil is made from Nb₃Sn, and has capability for high field operation. It has been designed for very high current density, in order to determine protection requirements of the coil, which determines the amount of copper required, the overall current density and thus the size of the coil.

Key coil parameters of the Nb₃Sn coil after heat treatment are given below:

- | | | |
|----|-------------------|----------|
| 1) | Coil ID: | 8.210 in |
| 2) | Coil OD: | 9.675 in |
| 3) | Coil Width: | 2.425 in |
| 4) | Number of layers: | 22 |
| 5) | Turns per layer: | 63 |

The coil has been designed to operate at a maximum current densities between 200-400 A/m².

The coil after heat treatment was placed in an aluminum casing. The basic dimensions of the aluminum casing are: I.D. of 8.21", O.D. of 10.25", and width of 3.27". A solid model of the aluminum shell is shown in Fig. C.1 Pictures of the finished coil incased in aluminum casing are given in Fig. C.2 Figure C.3 is a close-up of the first layer, showing a uniform winding array. The 22nd layer was as uniform when the coil was encased in the aluminum casing.

The wire used to make the coil is an internal-tin type wire. Supercon applied the s-glass insulation. The wire diameter over insulation was 0.962 mm.

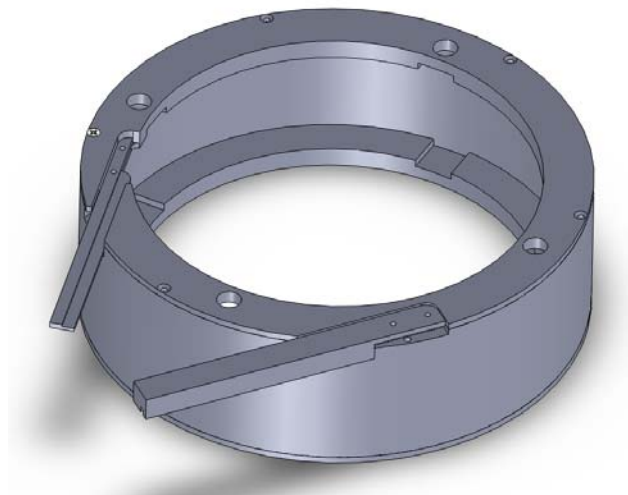


Figure C.1 Schematic diagram of the SC coil.

The encased coil was vacuum impregnated with CTD 512 epoxy. After curing, three 1' long pieces of 0.75mm diameter Nb-Ti type wires were soldered to each of the coil ends, to server as current leads. The Nb-Ti wires have a Cu/SC of 1/1 and each can carry 110A at 9T.

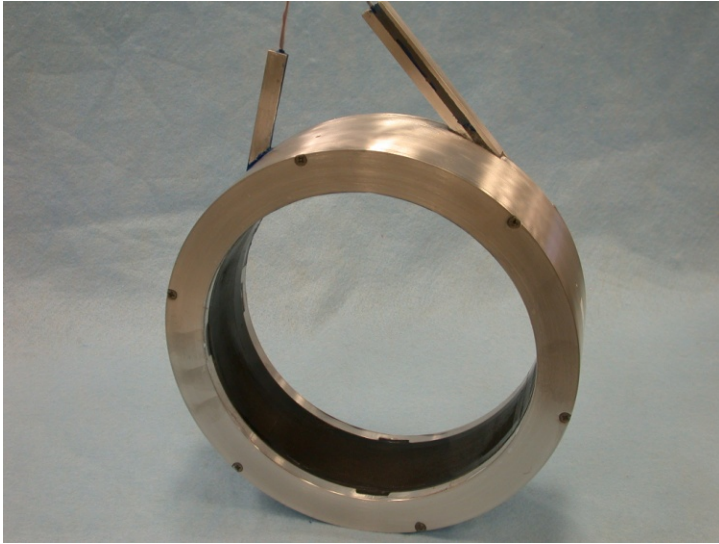


Figure C.2 Photograph of the finished coil

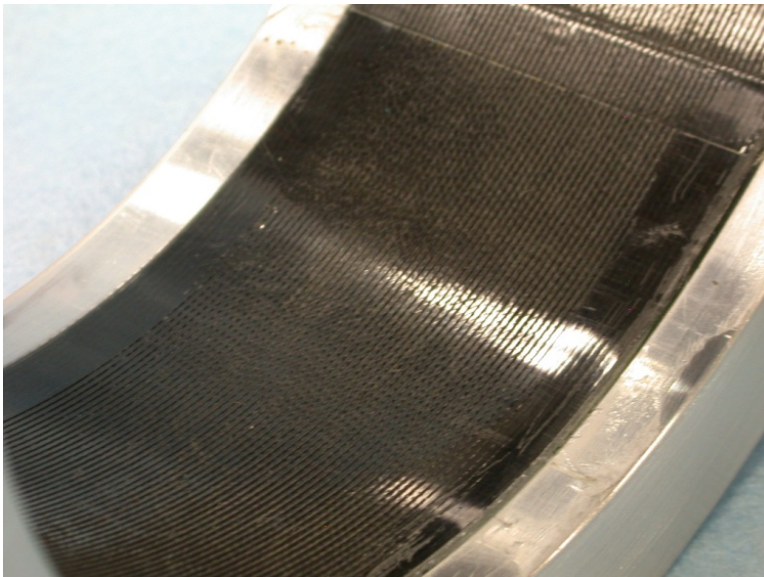


Figure C.3 Photograph of the innermost layer of the coil.

These coils will be tested during the 3rd year of the program. They will be tested to failure, to determine the protection characteristics of this type of coil, and to benchmark our models.

The rig and schematic for testing the coil are shown in Figures C.4-C.5.

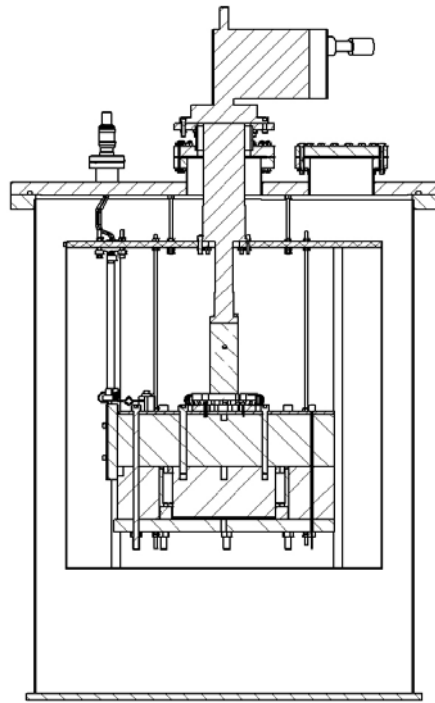


Fig. C. 4 Schematic of the testing setup for the superconducting coil

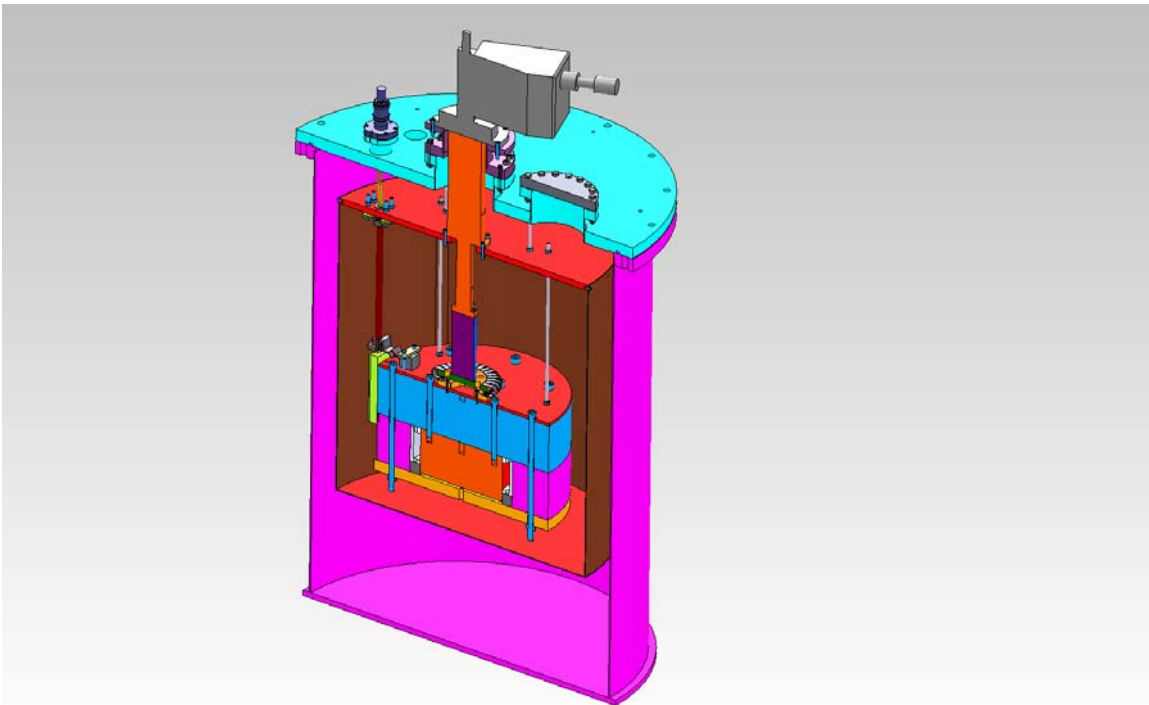


Figure C.5 Engineering diagram of the testing setup.

The end-to-end resistance of the coil after heat treatment was 19 ohms at room temperature. The calculated resistance of the wire making up the coil was about 47 ohms. The discrepancy is due to conductivity of the residual carbon within the glass insulation around the wire. The conductivity of carbon drops by about two orders of magnitude at below 10K and it should not be a problem when charging this coil. Also note that because the aluminum casing is in contact with outer surface of the coil, and that there is the residual carbon conductivity, the aluminum casing was not electrically grounded during charging.

C.2 Test Coil Quench Analysis

This section reports the results of several quench cases run as scoping studies on the Synchrocyclotron prototype test coil. The Synchrocyclotron prototype test coil is a wind-and-react Nb₃Sn coil wound from a single round strand approximately 1 mm diameter with a copper fraction of 20%. The wire is insulated with a fiberglass sleeve which goes through the wire reaction process. There are 50 turns per layer and 18 layers of conductor housed in an 6061-T6 bobbin. Fields and operating current are based on the POISSON model provided for the test configuration. The operating current for the coil is 500 A, resulting in a peak field on the winding of approximately 6 T.

Several quench runs were made for quench initiating from the high field point, first without credit for the Al bobbin and then with it, accounting for its energy consumption by eddy current heating and subsequent thermal conduction into the coil (quench back). The analyses show that the coil quench performance is limited by the low copper fraction in the conductor. With copper at only 20% of the metal cross section, copper current density is quite high when a coil section goes normal, and $\int J_{Cu}^2 dt$ thermal limits are reached quite quickly. The heat capacity of the other materials in the winding help prolong the temperature rise somewhat, particularly at low temperatures, but still, at 500 A, the winding hot spot reaches 300 K in about 40 ms, before the quench has hardly propagated, and before quench back can get started. Using low threshold (20 mV), fast detection (20 ms) dump hardly helps at 500 A, extending the time before reaching 300 K to only 52 ms. Without credit for the bobbin, the quench analysis shows that the operating current should be limited to between 200 A and 250 A, where the hot spot temperatures were calculated at 65.8 K and 187 K, respectively. With credit for the presence of the Al bobbin, operating current can be safely raised to 270 A with a calculated hot spot temperature of 130 K.

Quench from the low field point was evaluated at the 270 A operating condition with the effects of the bobbin included. The analysis shows that quench from the low field point is more benign than when quench is initiated from the high field point.

Details

Pourrahimi indicates that between the winding OD and the bobbin ID the coil has no extra ground insulation other than the nominal turn insulation. The turn insulation thickness was reported at 0.06 mm by Pourrahimi and 0.08 mm by Williams, but close-stacked circular wires using either insulation thickness do not fit into the winding space defined either as measured (Williams/Pourrahimi) or modeled (POISSON). This implies that there was either some crushing of the insulation or distortion of the circular cross sections (or both) during winding. These effects were accounted for in the quench model by assuming the wire cross sections stay circular. The quench model unit cell used for calculating bulk properties assumes the circular turns are spread to the maximum axial extent allowed by the bobbin dimension and then the glass insulation thickness is reduced to about 0.032 mm to enable the turns to fit in the available space. The unit cell is shown in Figure C.6. Notice the turn axial spreading effect is reflected by the epoxy filled section (yellow) adjacent to the circular wire/turn insulation regions. In consideration of the insulation thickness to ground, the maximum dump voltage was limited to $V_d = 200$ V in the quench studies. To evaluate quench at different currents, the dump voltage was kept constant by adjusting the size of the dump resistor, $R_d = \frac{V_d}{I_{op}}$.

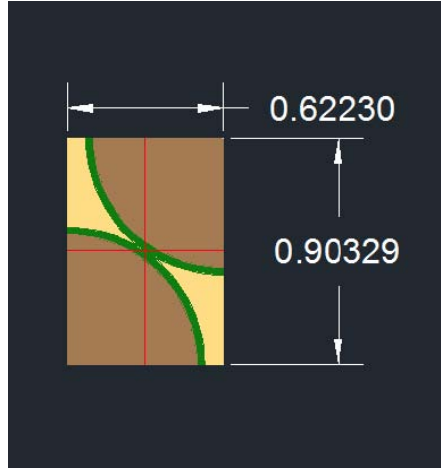


Figure C.6 Winding Unit Cell. The winding axial direction is horizontal and radial is vertical in the figure. Horizontal and vertical red lines are additional symmetry planes for calculation of bulk kappa values in the radial and axial directions, respectively.

Bulk material properties were calculated numerically for both the axial and radial directions by taking horizontal and vertical slices through the unit cell of Figure C.8 and using individual material properties. Thermal resistances were calculated within each slice using a series relationship for the thermal resistances in the slice and the total thermal resistance was calculated by combining all of the slice resistances in parallel. Bulk thermal conduction in the circumferential direction was calculated based on the thermal conductivity of copper as a function of magnetic field and temperature, multiplied by the area ratio of copper in the unit cell. Specific heat at each temperature is calculated based on the volume weights of the respective materials: copper, Nb_3Sn , epoxy-impregnated fiberglass (assumed to be G10) and pure epoxy. The specific heat of Nb_3Sn depends on whether it is superconducting or not. The specific heat of Nb_3Sn is much higher when it is superconducting, and this affects the quench propagation velocity.

Summary results of the quench runs without the bobbin are provided in Table C.1. Fields at full current at each of the quench model element locations are calculated in POISSON with its 2d accounting of the iron. Models for the field vs. current were not constructed for each element in the model, so once the current starts to decay, field is assumed to be everywhere proportional its original value multiplied by the ratio of the current to the current at the start of the problem.

The minimum propagating zone was not investigated. This exclusion will have some effect on the results reported for the quench protected cases. The quench model mesh size had to be much more coarse with the bobbin than without to prevent execution times from becoming too slow to be practical. Note that with no bobbin

present at 250 A, it took 54 ms to reach the quench detection/protection threshold of 20 mV + 20 ms time delay. The time to reach the quench detection/protection threshold starting from the minimum propagating zone would take longer. With the coarse mesh required for the bobbin cases, the voltage across the single normal element at the Bmax location was already more than enough to trigger the dump at $t=0$ s. The implication is that the hot spot temperatures could be somewhat higher than the 130 K reported for the 270 A case quenching from the Bmax location with the bobbin.

Transient plots of the analysis results at 270 A quenching from both the Bmax and Bmin locations with the bobbin effects included are shown in Figures C.7-C.12. Note that only 38% of the winding is normal at the end of the transient (1.18 s) for the quench from Bmax case. Temperature distribution plots at selected time points are included as Figures C.13C.16 for the quench from Bmax case. Voltages are worse at the time of the initiation of quench protection, in this case $t=0$. At this time the resistive voltage is virtually all across the dump resistor and it equals 200 V. If the dump circuit is balanced with respect to ground, then each end of the coil will be 100 volts from ground. Figure C.17 plots the approximate voltage distribution at 270 ms, the time when the normal zone voltage is maximum. Voltage is plotted by turn number with turn 1 assumed to be at the beginning of the first layer. All other turn voltages are referenced to the voltage at the start of the first turn. The voltage difference between turn 1 and 900 (number of turns in the coil) should equal the dump voltage at this time, $V_d = (107.8 \text{ A})(0.74 \text{ } \Omega) = 80 \text{ V}$. The plot shows a value more like 68 V. This difference is likely due to round off errors in the summation of the 19,440 element voltages, which themselves are subject to round off errors in their several component calculations based on mutual inductances and di/dt calculations, which, in turn depend on the additive element resistances of the model. In other words, round off errors can be significant, so the 15% error in the voltage calculation with turn number is perhaps rational.

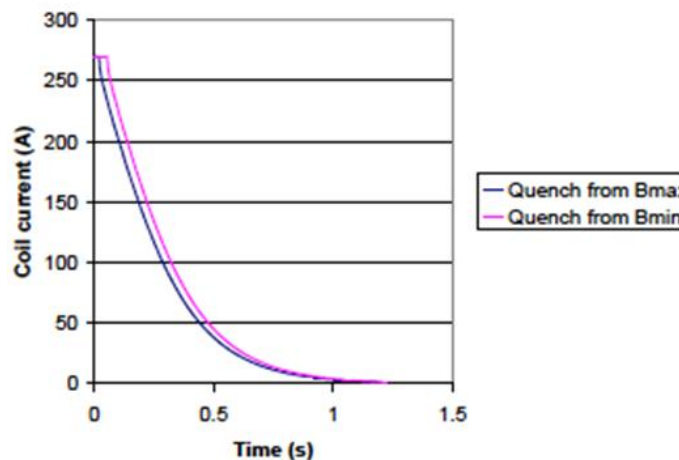


Figure C.7 Coil current

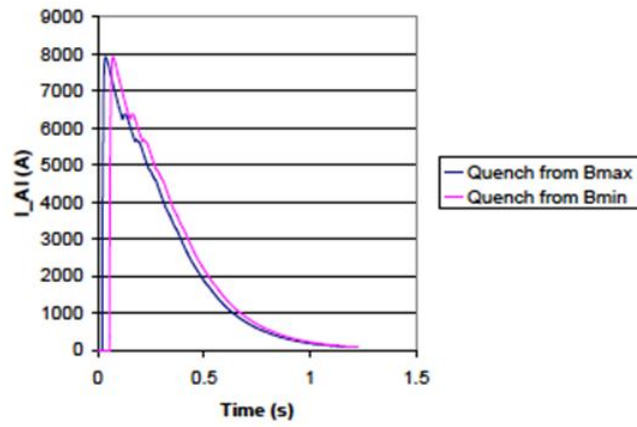


Figure C.8 Aluminum bobbin current

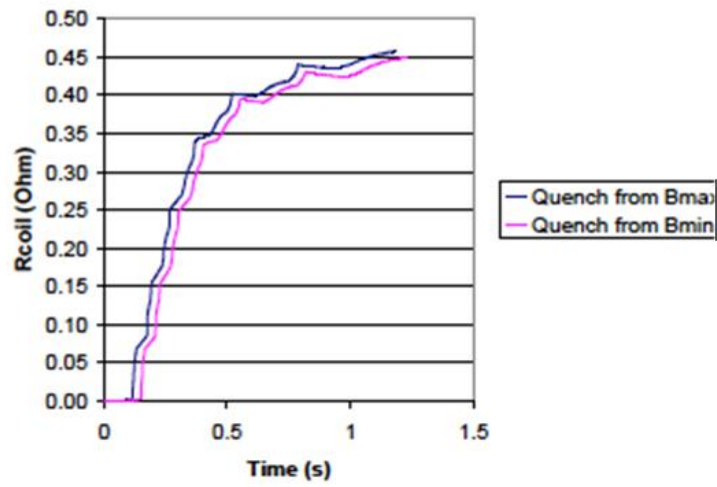


Figure C.9 Coil resistance

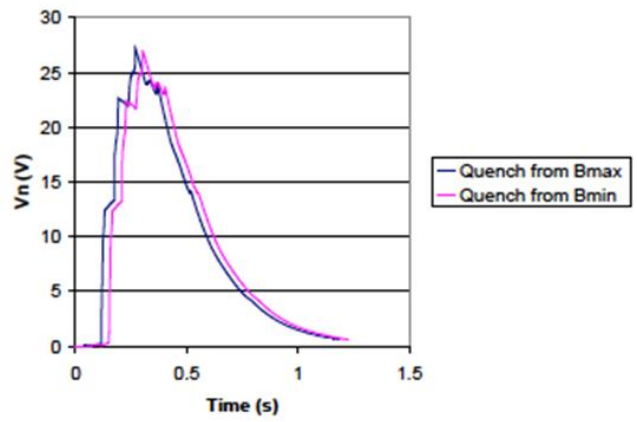


Figure C.10 Coil normal zone voltage

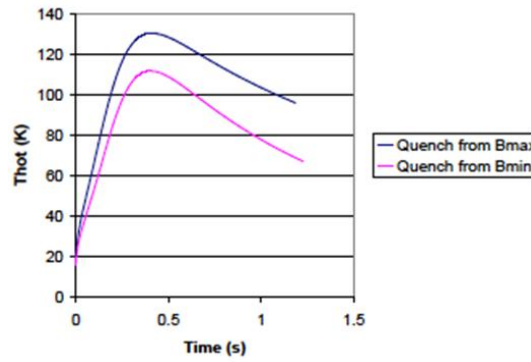


Figure C.11 Coil hot spot temperature

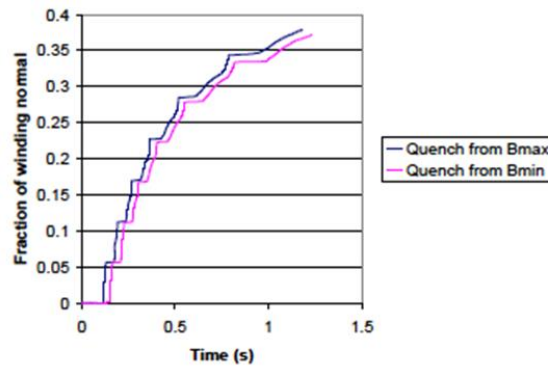


Figure C.12 Fraction of coil that is normal

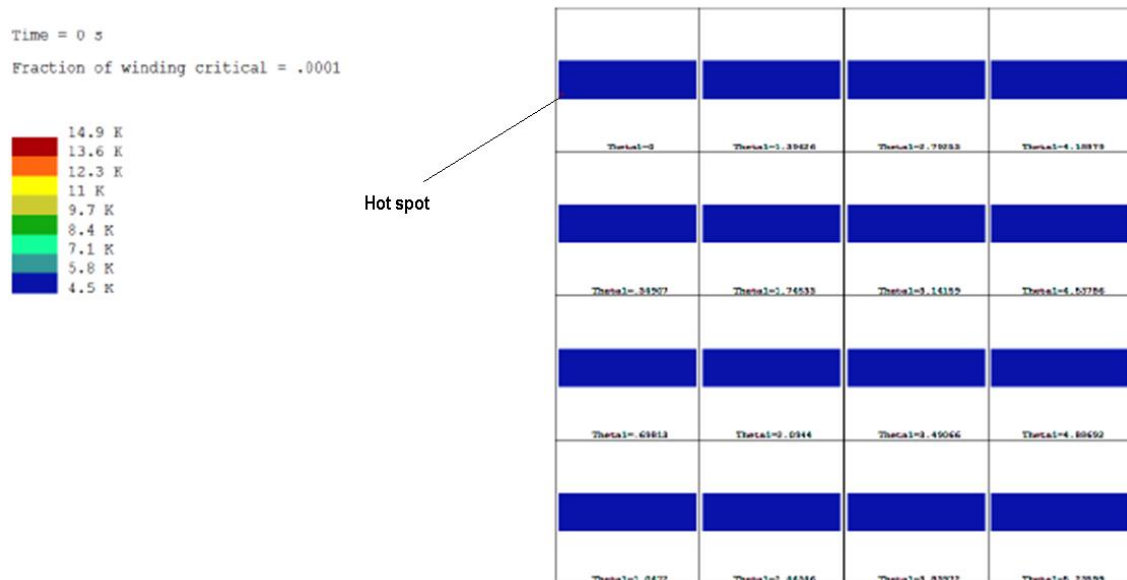


Figure C.13 Temperature distribution in coil winding, at $t = 0$. Each cell on the right represents the winding cross section at the identified aximuthal location. Horizontal is the axial direction and vertical is radial. Note the hot spot origination location at Bmax in the $\theta_1 = 0$ location.

Time = .1 s
 Fraction of winding critical = .0003



Figure C.14 Temperature distribution in coil winding, at $t = 100$ ms. Note that some heating from the aluminum bobbin is already visible in the outer layer of the winding and some outer layer winding elements are normal. Because of the small copper fraction, heating has not yet spread along the conductor in the theta direction.

Time = .5 s
 Fraction of winding critical = .2622

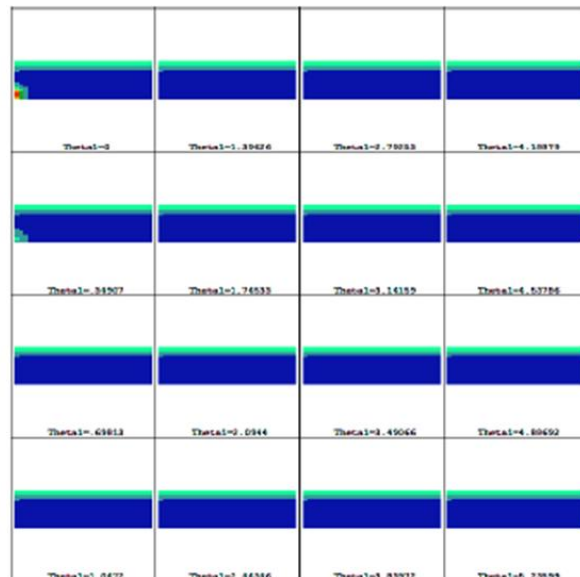
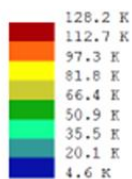


Figure C.15 Temperature distribution in coil winding, at $t = 500$ ms. Quench back is visible in the outer layers and heating has begun to visible spread along the conductor in the theta direction. Hot spot temperature has already been reached and has begun to cool.

Time = 1.1 s
 Fraction of winding critical = .3702

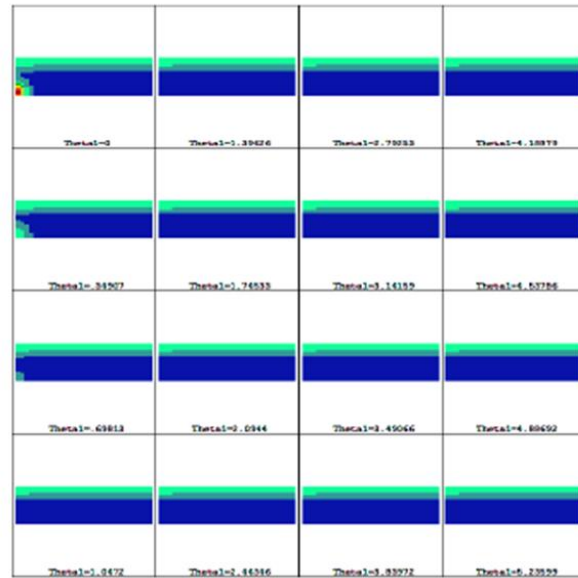
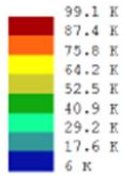


Figure C.16 Temperature distribution in coil winding, at $t = 1100$ ms. The transient is essential over and the winding is slowly starting to return to uniform temperature. Hot spot has cooled below 100 K.

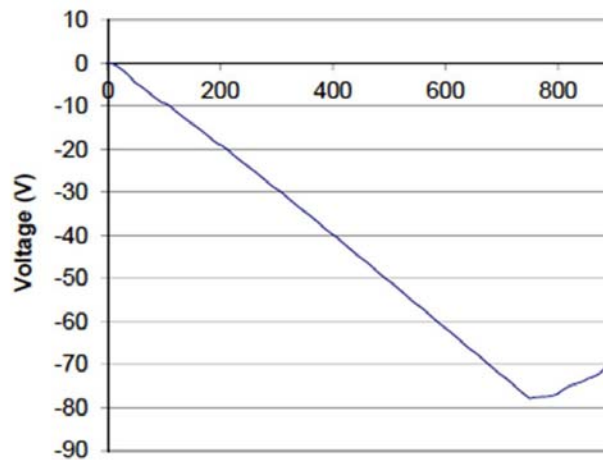


Figure C.17 Approximate cumulative voltage by turn number relative to the voltage at the beginning of the first turn.

Table C.1 Summary of Quench Run Results

Table 1 Summary of Quench Run Results

Case	Current (A)	Dump Resistance (Ω)	Stored Energy (kJ)	Detection Threshold (V_{th}), (mV)	Time Delay (ms)	Time V_{th} Reached (ms)	Current at end of run (A)	Thot or Result (K)	Fraction of coil normal t end of run (%)
1	500	0	32.2	n/a	n/a	n/a	499.9	> 300 in 40 ms	< 0.1
2	500	0.4	32.2	20	20	3	478.3	> 300 in 52 ms	< 0.1
3	400	0.5	21.9	20	20	13	358.6	> 300 in 89 ms	0.1
4	300	0.667	13.1	20	20	33	192.8	> 300 in 221 ms	0.5
5	250	0.8	9.52	20	20	54	1.2	187	2.9
6	200	0	6.42	n/a	n/a	n/a	195	> 300 in 422 ms	1.4
7	200	1	6.42	20	20	88	1.2	65.8	0.8

C.3 Magnetic Model of the Test Coil

A magnetic model of the Synchrocyclotron prototype Test Coil was made using Vector Fields Opera and the results of the field and EM energy calculations are presented below.

Model

General views of a 1/48th model of the “Nano_test” VF model are shown in Figures C.18a, b and c (** 5.4a-5.4c.) The Coil and the Iron Yoke dimensions shown in Figure C.19 (**** 5.5) are defined by Phil Michael.

8/Feb/2012 11:52:25

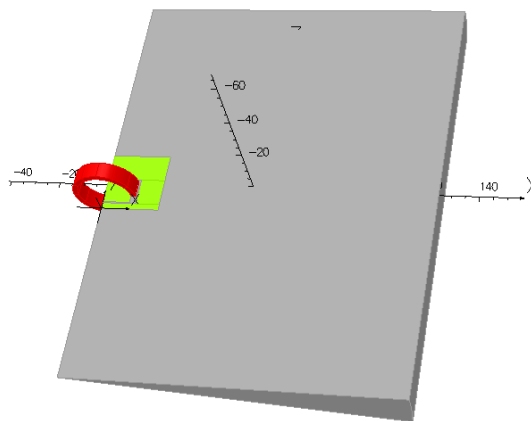


Figure C.18.a 1/48th model with the air

8/Feb/2012 11:54:20

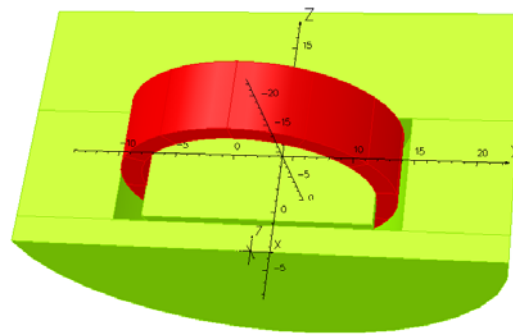


Figure C.18.b Half-iron yoke and the coil

8/Feb/2012 11:56:12

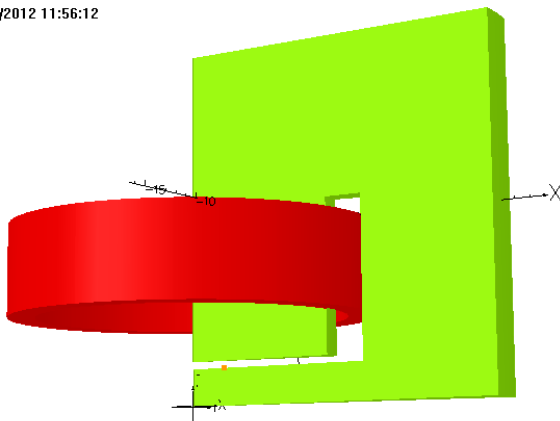


Figure C.18.c Field Monitoring Point (R=2.54 cm, Z=2.50 cm) is marked with an Orange Dot.

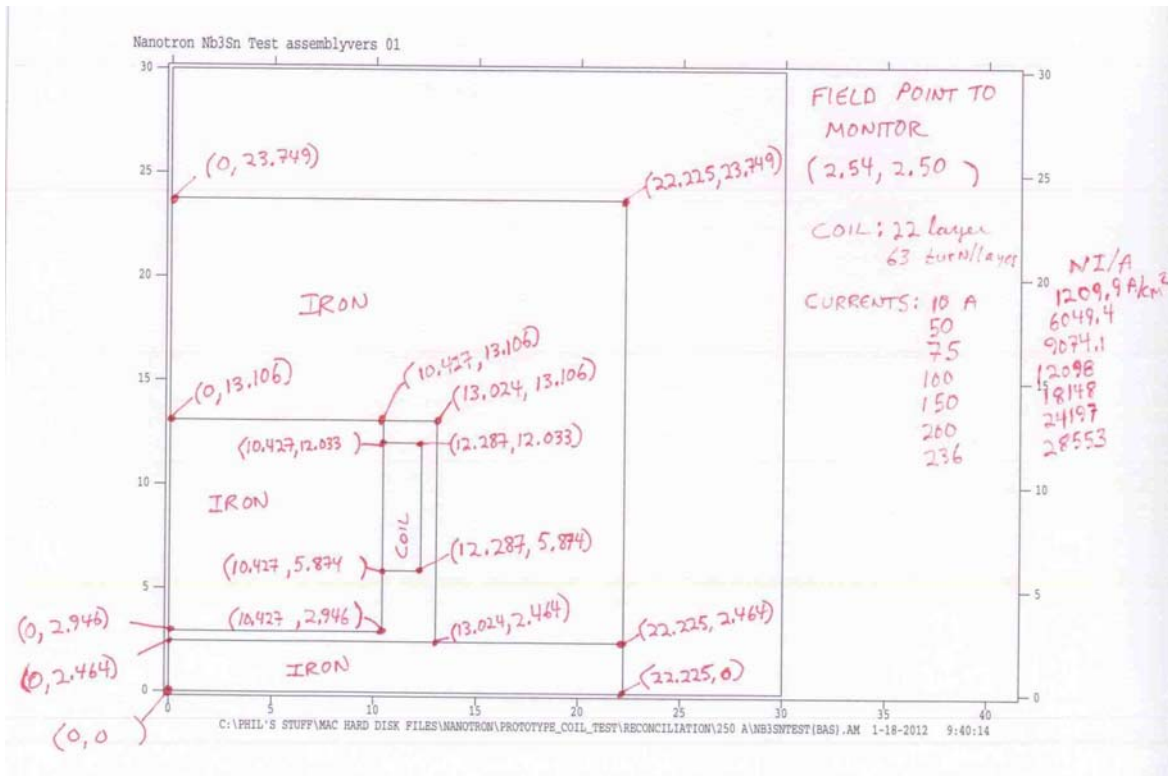


Figure C.19 Iron and Coil Dimensions

Analyses

Results of the analyses are summarized in Table C.2 and depicted in Figures C.20.a, b c and d (*****s. 5.6a – 5.6d.)

Table C.2 Results Summary

Ic	B(R=2.54 cm, Z=2.50 cm)	E	L
A	G	J	H
Coil with Iron			
5	10505	139	11.106
10	11989	280	5.605
50	17466	1328	1.062
75	20245	2501	0.889
100	22207	4090	0.818
150	25098	8442	0.750
200	27750	14267	0.713
236	29626	19280	0.692
Coil w/o Iron			
236	31453	14894	0.535

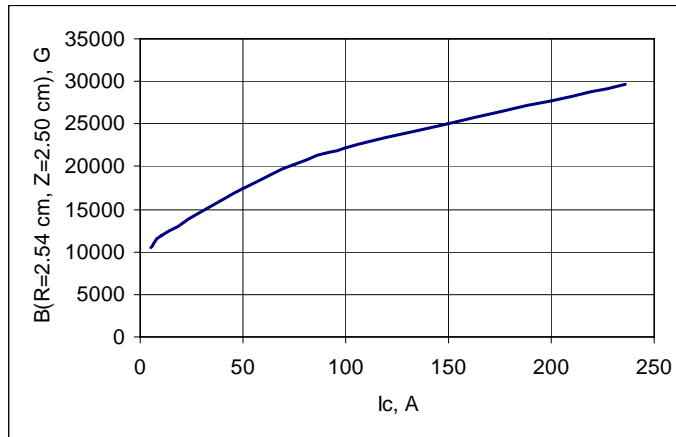


Figure C.20.a Field at the Hall probe Location vs. Coil Current

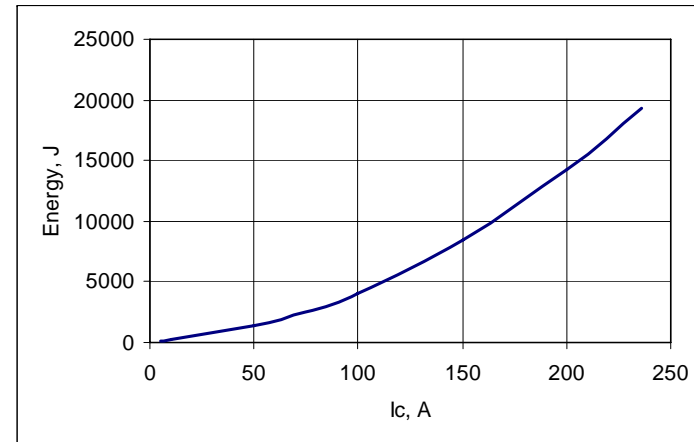


Figure C.20.b System EM Energy vs. Coil Current

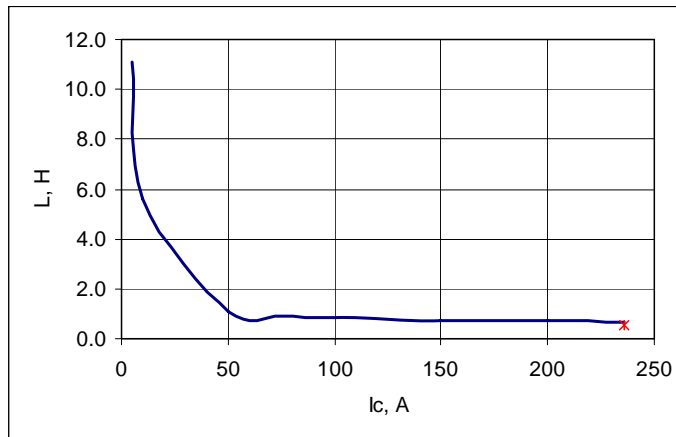


Figure C.20.c Inductance vs. Coil Current

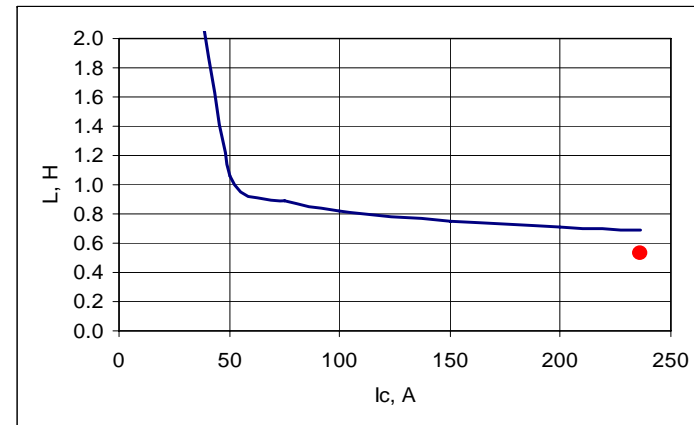


Figure C.20.d Inductance vs. Coil Current (fine scale)
Red dot – coil w/o the Iron

C.4 Test Coil Results

The test details and results are reported in great detail in a separate report authored by Philip Michael, PSFC/JA-12-7: Test of a conduction-cooled, prototype, superconducting magnet for a compact cyclotron, P.C. Michael, March 2012.

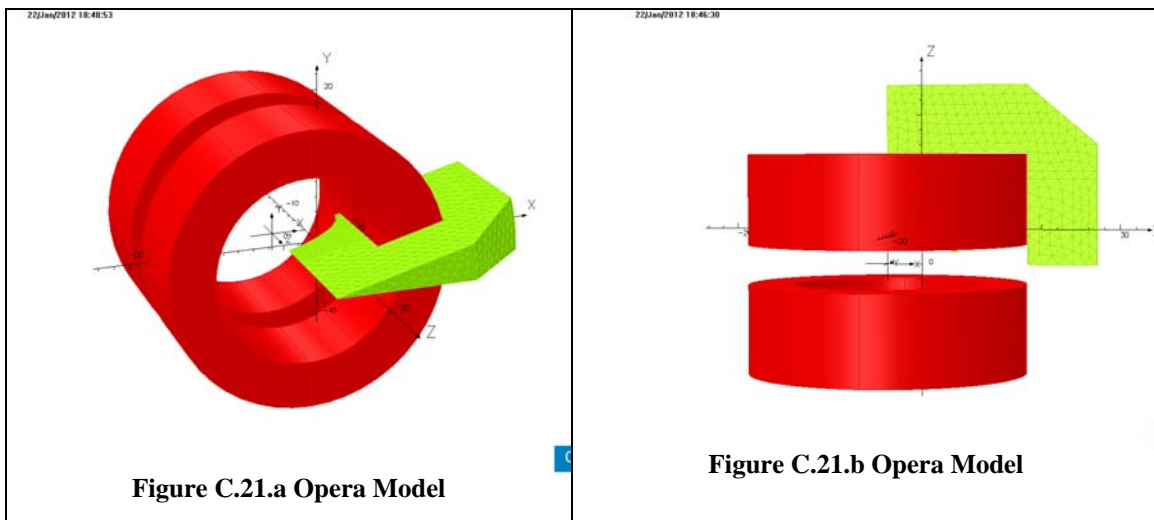
Newest Winding Pack Design

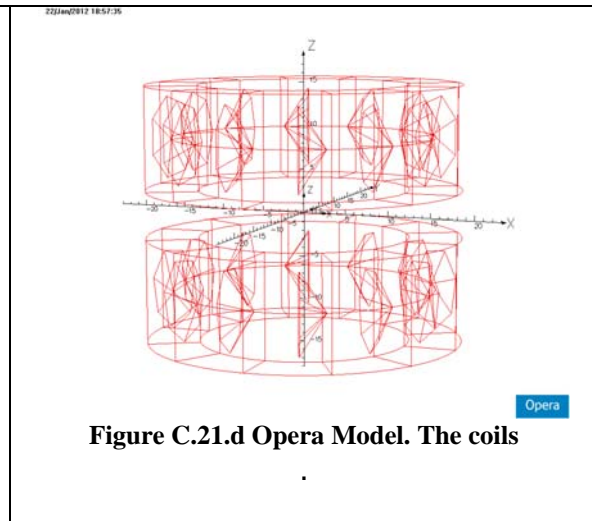
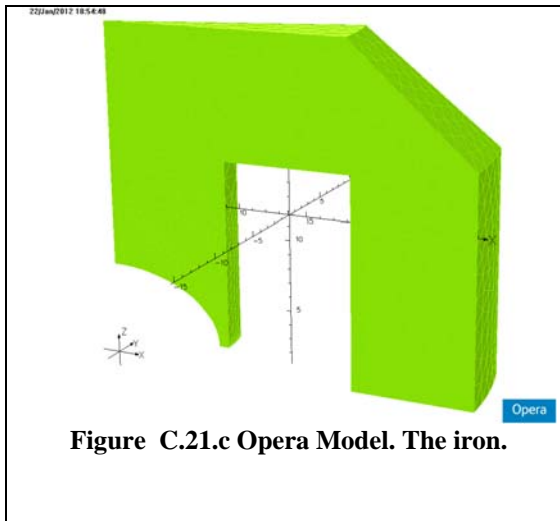
The results of the coil test and the accompanying quench analysis made it clear that the operating current density in the winding, and particularly in superconducting composite strand stabilizing copper, was much too high to safely protect the coil from quench without damage. We decided that the conductor and winding pack should be redesigned with a factor of 4 lower winding pack current density. This magnetic field analysis was performed by A. Radovinsky for this new case.

This magnetic design of the Synchrocyclotron prototype magnet system calculated using the Opera program corresponds to our specifications by most parameters, except for the winding pack current density, which was reduced from 400 A/mm² as in to the vicinity of 100 A/mm².

Model

General views of the 1/48th model of the nano7c build are shown in Figures C.21.a – d (**** 5.10a-5.10d). The model has a 1/24 rotational symmetry and half-symmetry due to a reflection about Z=0.





The iron was modeled using a BH curve defined below.

The shape of the iron is defined by the characteristic points shown in Figure C.22 and Table C.3. Note that the curve between points 9 and 10 is a $1/4^{\text{th}}$ of an ellipse.

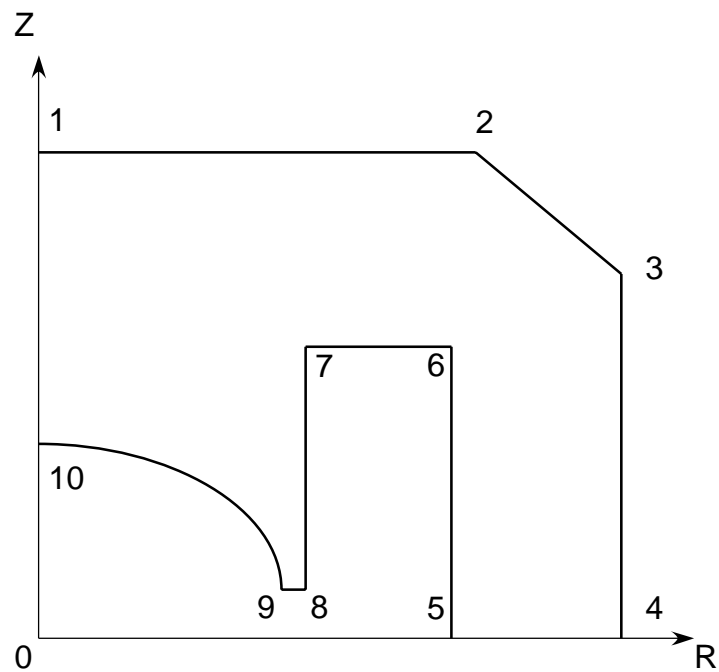


Figure C.22 Iron Yoke Characteristic Points

Table C.3 Iron Yoke Characteristic Points (model nano7c)

Point #	R	Z
	cm	cm
1	0.0	24.0
2	18.0	24.0
3	27.0	16.0
4	27.0	0.0
5	18.3	0.0
6	18.3	15.0
7	9.0	15.0
8	9.0	1.7
9	8.3	1.7
10	0.0	6.7

Analyses

General design parameters of system are listed in Table C.4. Formulae in Addendum B were used for calculating characteristics of the beam and the RF system.

Table C.4 Model Summary

Model		7c
Coil		
Rc	cm	15.0
Zc	cm	8.7
dR	cm	6.0
dZ	cm	12.0
Jwp	A/mm ²	111.50
Bpeak	T	6.04
Fz	kN	218
Energy	kJ	240
Proton Beam		
Rex	m	0.0800
Bex	T	5.692
Rigidity	T-m	0.455
gamma		1.011
E	MeV	10.03
RF		
f_min	MHz	85.88
f_max	MHz	88.38

Figures C.23 - C.29 depict variation of the controlled characteristics versus radius and of nuz (nur) with respect to the resonant combinations.

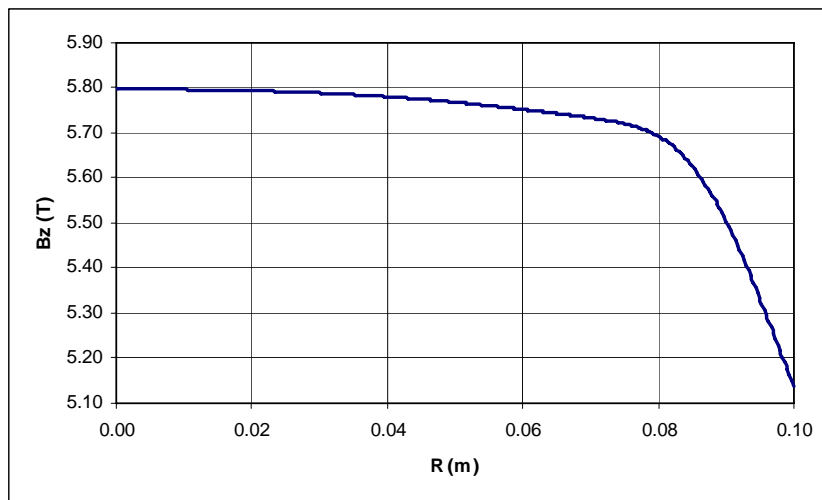


Figure C.23 Field vs. radius

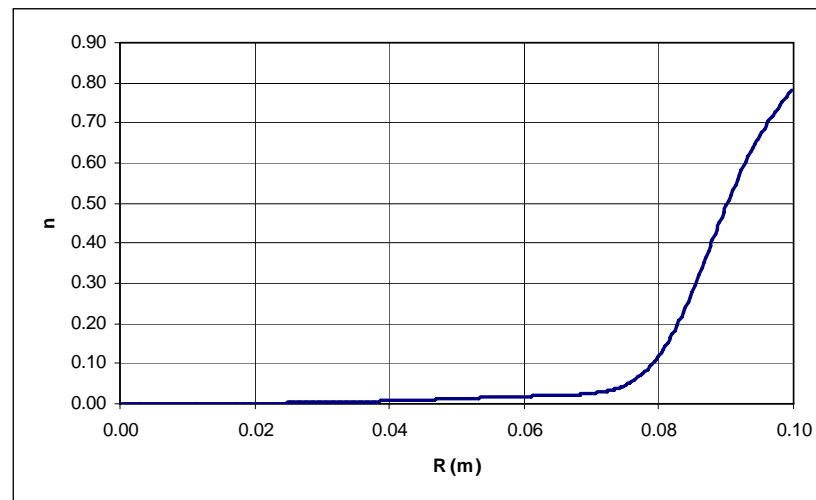


Figure C.25 Index vs. radius

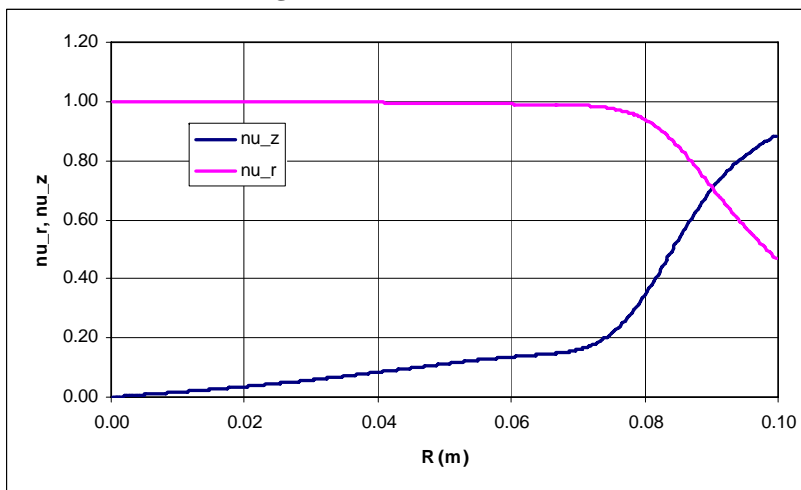


Figure C.24 nur and nuz vs. radius

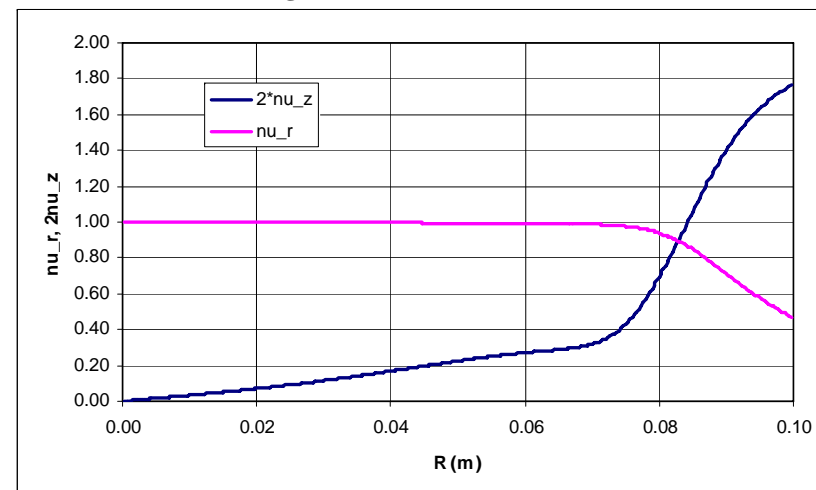


Figure C.26 $n=0.2$ ($n_r=2*n_z$ intersect) at $R=8.3$ cm

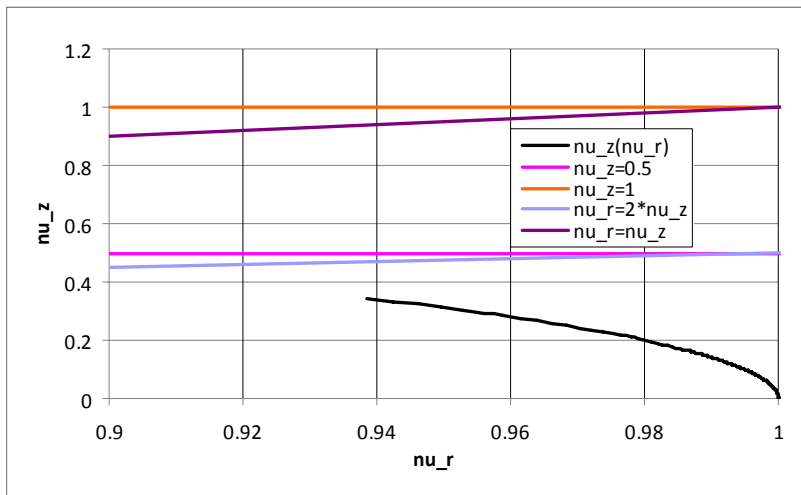


Figure C.27 $\nu_z(\nu_r)$ vs. resonances

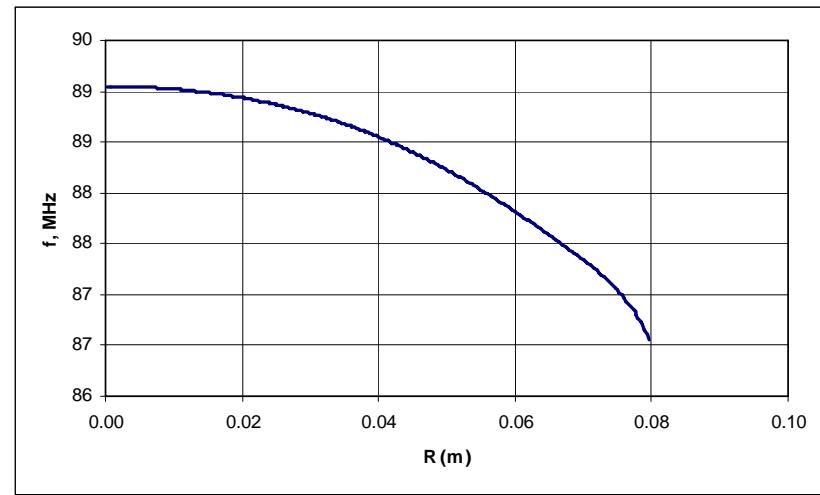


Figure C.29 RF frequency vs. radius

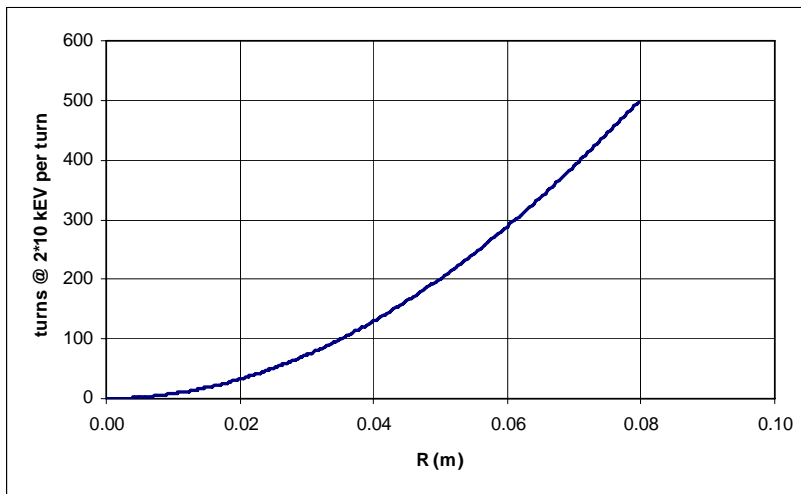


Figure C.28 Turn count at $2 * 10$ keV per turn

C. 5 Conclusion

General sizing of a synchrocyclotron magnet system has been performed according to our specification. The proposed design corresponds to the specs by most parameters, except for the winding pack current density, which was reduced from 400 A/mm^2 to the vicinity of 100 A/mm^2 . Compared to the most recent reference design this resulted in increasing the cross section of the coil by about 2x2 and respectively reshaping of the iron yoke to accommodate this, bigger, coil. The beam extraction radius, $R=8 \text{ cm}$, and the proton beam energy, $T=10 \text{ MeV}$, stayed unchanged.

D. HTS Potential for cyclotrons

HTS can be used for cyclotron improvement. There are two main forms of the HTS that can impact cyclotrons: HTS tapes, and HTS bulk.

HTS bulk has been described in Section B.

HTS tapes can be used as the material for the main cyclotron windings. They offer the potential of both higher field operations, as well as higher temperature operation. By operating at higher temperature, it is possible to decrease the power required from the refrigerator. The cryogenic load is not sensitive to the temperature of operation, but the power required to cool it is. At 20 K, it is possible to reduce the refrigerator power by a factor of 5 (for cooling the cold region). However, a large fraction of the load occurs at higher temperatures, for cooling the current lead. We are investigating the possibility of using joints that would allow to disengage the current leads from the magnet. The magnet would not be persistent, because of the finite resistance of the joint, but the decay would be long and would allow for operation without the need for substantial cooling at the higher temperatures.

In addition, we are exploring the possibility of using low current for driving the cyclotron. Low current operation makes protection difficult, in that the voltage required for dump (before the superconductor is damaged) is high. Instead, we are investigating means of quenching the magnet and providing a uniform energy dump (internal dump). Two means are being investigated, through the use of heaters and through the use of inductive quench.

This is a summary presenting a magnetic design of a 2 GeV Isochronous Proton Cyclotron Accelerator utilizing HTS tiles for creating the flutter field configuration for the strong focusing of the beam in the accelerator region.

We have developed preliminary numbers for the potential of the technology (HTS main coil and flutter field). The basic parameters of an isochronous magnetic field are summarized in Table D.1.

Table D.1. Design Specification

Parameter	Units	Value
T	GeV	2.073
R_ex	m	1.00
B_ex	T	9.56
B_0	T	2.97
alpha	m	1.0524
gamma_ex		3.213

Parameters of the flutter field are derived from the most critical limitation requiring that ν_z shall not be smaller than a given number epsilon,

$$(1) \quad \nu_z^2 = n + f^2(1 + 2(R/A)^2) \geq \epsilon^2,$$

where

$$n = 1 - \gamma, \quad \gamma = 1/\sqrt{1 - (R/\alpha)^2} \text{ and}$$

$$f^2 = 1/2\pi \int_0^{2\pi} [(1 - B/B_{av})^2] d\theta = s/4 (dB/B_{av})^2,$$

is presented as a function of the shaping factor, s , and the range of the flutter field variation, $dB = B_{max} - B_{min}$.

Condition (1) shall be satisfied over the whole range of acceleration, $0 < R < R_{ex}$.

Assuming that

- the shape of the flutter field is defined by an Archimedes spiral with shaping parameter, $A = R_{ex}/3 = 0.33$ m.
- $\epsilon = 0.2$,
- flutter field shaping factor, $s = 0.7$

we can calculate the required dB from the following equation yielding from (1) (where $\nu_z = \epsilon$)

$$(2) \quad dB = 2B_{av} \sqrt{[(\epsilon^2 + \gamma^2 - 1)/(2(R/A)^2 + 1)]}$$

Figures D.1 and D.2 show the targeted profiles of the isochronous magnetic field, B_{av} , and the amplitude of the flutter field, dB , as a function of the radius. Figure D.3 shows ν_z and ν_r as a function of the radius.

Let us assume that the NTS tiles forming the flutter field are an ideal paramagnetic shaped so that after applying the isochronous magnetic field, B_{av} , they will extrude the field by the law, which complies with the assumed above shaping factors, A and s , and the required dB as a function of the radius. The coil system was designed using Vector Fields (VF) Opera, which can create the required isochronous field. It is shown in Fig. D.4. Fig D.5 shows the target B_{av} and the field of the coil system shown in Fig. D.4. A small discrepancy between the designed and the target field can be easily eliminated in the future.

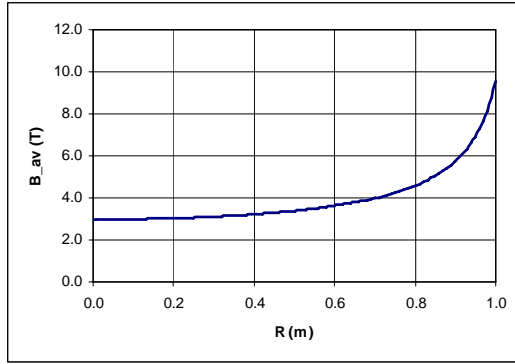


Fig. D.1 Target Isochronous Field

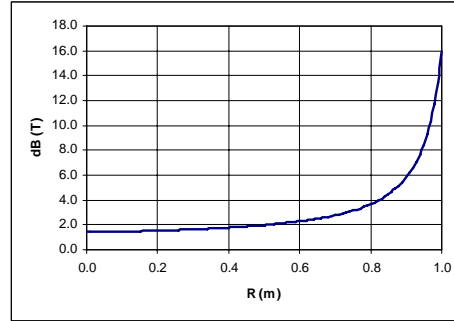


Fig. D.2 Target Amplitude of Flutter Field

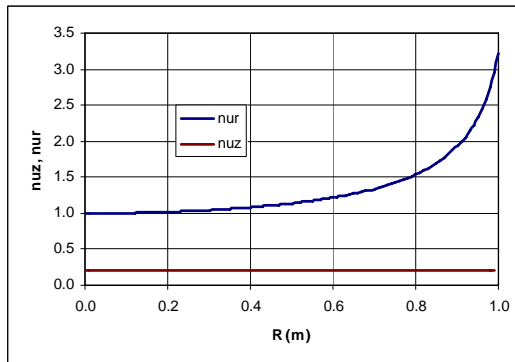


Fig. D.3 Corresponding nu_r, nu_z

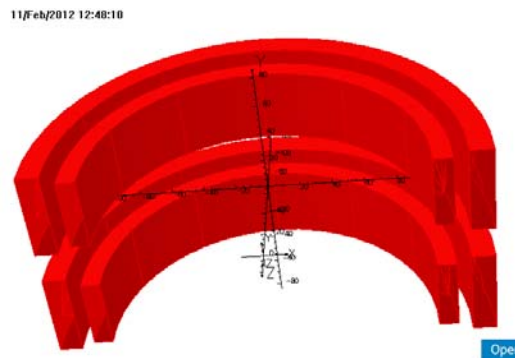


Fig. D.4 VF Coil Model (1/2 shown)

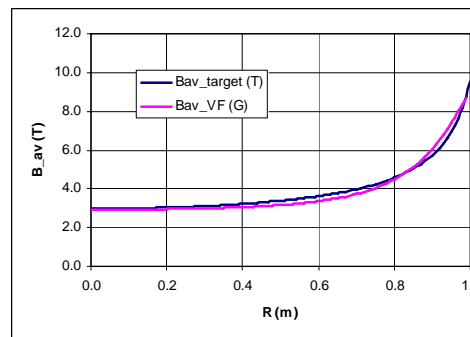


Fig. D.5 Targeted and Modeled Isochronous field

Comments

1. The peak field in the coils shown in Figure 5 is 27 T. Current density is 200 A/mm². Note that the problem of providing flutter even at these extremely high fields has been addressed by the use of HTS monoliths.

2. A similar design of the Megatron (T=250 MeV) with inductively charged or driven HTS coils shaped as Archimedes spirals has a chance. It will be scalable, at least theoretically, and the fields are much less challenging.

E. Evolution of proton bunches in high intensity cyclotrons: a preliminary study on space-charge effects

This work was carried in collaboration with Drs. Antoine Cerfon, Buddy Gardineer, Felix Parra, and Jeffrey Freidberg.

E.1 Introduction

In this task, we focus on understanding the evolution of proton bunches in isochronous cyclotrons in a regime sometimes referred to as the “high-intensity regime”. This is a regime in which the bunch density is so high that electrostatic space-charge forces cannot be neglected, and modify the dynamics of the bunch as calculated from single-particle theories.

E.2 Geometrical effects

The approach that we follow here can be qualified as “bottom-up”. Specifically, we do not start by constructing a very complicated numerical solver, which would account for all the geometrical intricacies of an isochronous cyclotron, but perhaps not yield many insights. Instead, we choose to build our physical intuition of the physical processes at stake little by little. In the first stage of our analysis, we will therefore ignore all the possible complications arising from the cyclotron geometry: we will study the evolution of the proton bunch in a classical cyclotron.

In fact, in the preliminary stage which we describe below, we will do even simpler than that. We will assume that the cyclotron magnetic field is homogeneous in space, and study space-charge and temperature effects on a proton bunch which is drifting in this homogeneous magnetic field. We will see that this extremely simple case already yields some very interesting insights. The next steps, not described in this report, will be to add the accelerating gaps, then the spatial variations of the magnetic field, etc.

E.3 Physical models for the evolution of the proton bunch

Beside the complications due to the geometry of the cyclotron, there also are several possible levels of complication for the equations used to describe the evolution of the bunch.

A. Kinetic description

Ideally, we would solve for the phase-space distribution function of the proton bunch, $f(\vec{r}, \vec{v}, t)$, such that $f(\vec{r}, \vec{v}, t)d\vec{r}d\vec{v}$ is the number of proton particles

near point \vec{r} , having velocity \vec{v} , at time t . Indeed, if we found a way to compute f for any time, at any place, and for any velocity, we would then exactly know all the bunch physical quantities which could be of interest. For instance, the density of the bunch at any point in time and any point in space is

$$n(\vec{r}, t) \equiv \int f(\vec{r}, \vec{v}, t) d\vec{v}$$

the flow velocity is

$$\vec{V}(\vec{r}, t) \equiv \frac{1}{n(\vec{r}, t)} \int f(\vec{r}, \vec{v}, t) \vec{v} d\vec{v}$$

and the pressure is

$$\vec{p} \equiv m \int f(\vec{v} - \vec{V})(\vec{v} - \vec{V}) d\vec{v}$$

In the absence of Coulomb collisions between the protons (usually a good assumption for bunches in cyclotrons), and assuming that relativistic effects can be neglected, the equation for the distribution function is

$$\frac{\partial f}{\partial t} + \vec{v} \cdot \nabla f + \frac{e}{m} (\vec{E} + \vec{v} \times \vec{B}) \cdot \nabla_{\vec{v}} f = 0 \quad (0.1)$$

This equation can be seen as a consequence of Liouville's theorem. It simply states that the proton distribution function must be constant along the particle trajectories, given by

$$\frac{d\vec{r}}{dt} = \vec{v}; \quad \frac{d\vec{v}}{dt} = \vec{a} = \frac{e}{m} (\vec{E} + \vec{v} \times \vec{B})$$

Eq.(0.1) looks deceptively simple, and one may be tempted to think that it can be solved easily. The reason it is not so is three-folds:

1. The unknown function f depends on 7 independent variables: 3 for space, 3 for the velocities, and 1 for time

2. The equation is nonlinear. Indeed, as f changes in time, the electric field \vec{E} and the magnetic field \vec{B} also evolve, since the charge density and the electric current density are given by

$$\rho(\vec{r}, t) = e \int f(\vec{r}, \vec{v}, t) d\vec{v} \quad \vec{J}(\vec{r}, t) = e \int f(\vec{r}, \vec{v}, t) \vec{v} d\vec{v}$$

3. The equation describes processes occurring over very different length scales (e.g. the typical length scale of the bunch vs. the radius of the bunch orbit) and time scales (e.g. the cyclotron frequency vs. the slow time scale associated with the expansion of the bunch due to space-charge effects)

The bottom line is that a kinetic treatment quickly becomes fairly involved, and computationally intensive. Still, in many cases, it cannot be avoided. For example, beam phase-space instabilities, or viscosity effects can only be treated properly if one uses a kinetic description of the proton bunch. In the future, we are therefore very likely to use such a kinetic description to develop a proper theory for the MEGATRON. For this preliminary stage however, we will use a simplified fluid treatment of the proton bunch to get our first insights into space-charge and temperature effects.

B. Fluid description

By taking moments of the kinetic equation, *exact* fluid equations can be derived. For example, by integrating the kinetic equation over all velocities, we have:

$$\frac{\partial n}{\partial t} + \nabla \cdot (n \vec{V}) = 0 \quad \text{conservation of mass} \quad (0.2)$$

where n and \vec{V} , the density and the flow velocity, have been defined above. Multiplying the kinetic equation by \vec{v} and integrating over all velocities, we have

$$mn \left(\frac{\partial \vec{V}}{\partial t} + \vec{V} \cdot \nabla \vec{V} \right) + \nabla \cdot \vec{p} = en (\vec{E} + \vec{V} \times \vec{B}) \quad \text{conservation of momentum} \quad (0.3)$$

where \vec{p} has been defined previously.

With these two equations, a well-known problem associated with taking moments of the kinetic equation becomes apparent. It is often called the *closure problem*, and can be explained as follows.

Eq.(0.2) is an equation for the density n , but we also need to know the flow velocity \vec{V} to solve it. Eq.(0.3) is such an equation for \vec{V} (also involving n), but we need to know the pressure tensor \vec{p} to solve it (provided \vec{E} and \vec{B} are known through Maxwell's equations, which we did not write here). To determine \vec{p} , we would thus need to take a higher moment of the kinetic equation, and obtain a fluid-like equation for this tensor. Unfortunately, such an equation would also involve another new unknown physical quantity, sometimes called the stress flux tensor, for which we would need a new equation as well. There is clearly no end to this infinite process.

In other words, the closure problem is the somewhat discouraging observation that each exact fluid moment depends on the next higher moment.

There are several strategies to avoid this fundamental obstacle. One of them is to treat the problem fully kinetically, i.e. to solve the kinetic equation (Eq.(0.1)), with all the advantages and disadvantages described in the previous section.

Another strategy is *truncation*. The idea is to assume more or less arbitrarily (depending on the level of accuracy that one desires) that since high-order moments of the kinetic equation carry information which only leads to slight modifications of the quantities defined in the low-order moment equations (typically density, velocity, and pressure), they are negligible. The moments that are kept in the analysis and considered as relevant depend on the level of accuracy that one desires for the calculation.

In the present case, we will only retain the first two moments of the kinetic equation, Eq.(0.2) and Eq.(0.3). To close the system of equations, we will assume that the pressure tensor \vec{p} is isotropic, so that $\vec{p} = p\vec{I}$ and $\nabla \cdot \vec{p} = \nabla p$. Furthermore, we will assume that the pressure of the bunch behaves in the same way as the pressure of an ideal monoatomic gas, so that

$$\frac{\partial p}{\partial t} + \vec{V} \cdot \nabla p + \gamma p \nabla \cdot \vec{V} = 0 \quad \text{with } \gamma = \frac{5}{3} \quad (0.4)$$

Note that with this approximation, Equations (0.2), (0.3) and (0.4) form a set of 5 equations for 5 unknowns, so the problem is now well-posed, and we can try to solve it.

In several types of plasmas, the assumptions that the pressure tensor is isotropic and that the scalar pressure evolves as in Eq.(0.4) are not valid. This is in particular the case for the non-neutral plasma of interest in our case: with the beam parameters of the proton bunch in the MEGATRON and the magnitude of the electromagnetic fields, the two assumptions used to write Eq.(0.4) cannot be rigorously justified. This is the reason why a kinetic treatment of the problem will probably be necessary in later stages of this project.

Still, Eq.(0.4) remains an reasonable choice for this preliminary study, for the following reasons:

- It is simple
- We are mostly interested in space-charge effects, and in the proton bunch, forces associated with space-charge effects dominate forces associated with temperature effects, with a ratio of about 4 to 1 (see Section II below)
- At zero temperature ($p=0$), Eq.(0.2) and Eq.(0.3) are *exact*, i.e. they would take exactly the same form in a fully kinetic treatment of the problem
- As we will show in section III.3.B, when the pressure tensor is assumed to be isotropic the exact details of Eq.(0.4) do not have any effect on the evolution of the bunch density. They only matter for the evolution of the pressure itself

C. Electromagnetic fields

We will initially ignore relativistic effects. Therefore, the self-electric field due to the proton charges is very well approximated by an electrostatic electric field, determined by solving Poisson's equation:

$$\vec{E} = -\nabla\phi \quad \nabla^2\phi = -\frac{en}{\epsilon_0}$$

If we ignore relativistic effects, then we can also ignore the self-magnetic field of the moving proton bunch, and consider that the magnetic force on the bunch is purely that of the known externally applied magnetic field.

Summary

In summary, in this preliminary study we will study the evolution of a proton bunch drifting in a homogeneous externally applied magnetic field \vec{B} , and subject to space-charge and temperature effects. In the lab frame, the fluid equations describing this evolution self-consistently are the following:

$$\begin{aligned} \frac{\partial n}{\partial t} + \nabla \cdot (n \vec{V}) &= 0 \\ mn \left(\frac{\partial \vec{V}}{\partial t} + \vec{V} \cdot \nabla \vec{V} \right) &= en \left(-\nabla\phi + \vec{V} \times \vec{B} \right) - \nabla p \\ \frac{\partial p}{\partial t} + \vec{V} \cdot \nabla p + \gamma p \nabla \cdot \vec{V} &= 0 \\ \nabla^2 \phi &= -\frac{en}{\epsilon_0} \end{aligned} \tag{0.5}$$

E.4 Starting fluid equations: Non-dimensional equations in moving frame

From Eq.(0.5), one can easily derive the following set of normalized equations, describing the bunch as a warm fluid in the frame rotating at the cyclotron frequency:

$$\begin{aligned} \frac{dn}{dt} + n \nabla \cdot \vec{v} &= 0 \\ \frac{d\vec{v}}{dt} + \vec{v} \times \vec{e}_z &= -\epsilon^2 \left(\nabla\phi + \frac{\alpha^2}{n} \nabla p \right) \\ \frac{dp}{dt} + \gamma p \nabla \cdot \vec{v} &= 0 \\ \nabla^2 \phi &= -n \end{aligned} \tag{0.6}$$

The following quantities are involved in Eq.(0.6):

$$\begin{aligned}
\frac{d}{dt} &= \frac{\partial}{\partial t} + \vec{v} \cdot \vec{\nabla} & t &= \Omega t' \\
\vec{r} &= \frac{\vec{r}'}{a} & \nabla &= a \nabla' \\
\vec{v} &= \frac{\vec{v}'}{a\Omega} & n &= \frac{n'}{N_0} \\
p &= \frac{p'}{N_0 T_0} & \phi &= \frac{\epsilon_0}{e N_0 a^2} \phi' \\
\epsilon^2 &= \frac{\omega_p^2}{\Omega_c^2} & \omega_p^2 &= \frac{N_0 e^2}{m \epsilon_0} \\
\alpha^2 &= \frac{T_0}{m a^2 \omega_p^2} = \frac{\lambda_D^2}{a^2}
\end{aligned} \tag{0.7}$$

a is the characteristic size of the proton bunch (its radius if the bunch is spherical), N_0 the peak density of the bunch, and T_0 its peak temperature. For the MEGATRON parameters, ϵ^2 is a very small number: $\epsilon^2 \approx 0.0028$. We also have $\alpha^2 \approx 0.23$.

All the $'$ quantities correspond to the “real” physical quantities, *i.e.* the quantities measured in the lab units, but in the moving frame, which was defined by the following transformation:

$$\begin{aligned}
r' &= \bar{r} & \theta' &= \bar{\theta} + \Omega t \\
z' &= \bar{z} & t' &= \bar{t} \\
v_r' &= \bar{v}_r & v_\theta' &= \bar{v}_\theta + r\Omega \\
v_z' &= \bar{v}_z & n' &= \bar{n} \\
p' &= \bar{p} & \phi' &= \bar{\phi}
\end{aligned} \tag{0.8}$$

In Eq.(0.8), we have introduced the natural cylindrical coordinates associated with the cyclotron geometry: the z -direction is along the magnetic field, r is the radial coordinate in the plane perpendicular to the magnetic field, and θ the angle coordinate in that plane. All the quantities with the symbol $\bar{}$ over them refer to quantities measured in the (non-moving) lab frame.

E.5 Ideal focusing model

For this analysis, as a first step, we will work with a model which can be described as the *ideal focusing model*. It assumes that there is a perfect focusing force parallel to the magnetic field, which is in the z direction. Consequently, for all times, we have $v_z(\vec{r}, t) = 0$. This assumption simplifies the analysis, and is partly justified by the fact that cyclotron engineers usually do not encounter any difficulties in focusing the bunch in the vertical direction. If in the future

experimental evidence shows that there in fact is a strong coupling between the vertical beam dynamics and the dynamics in the plane perpendicular to the magnetic field, we may have to get rid of this assumption, and consider the motion of the bunch in the z direction.

A. Asymptotic analysis: Asymptotic expansion

Given the difference in the time scale associated with the betatron oscillation and that associated with the expansion of the beam due to electrostatic and thermal forces, we perform an asymptotic analysis of the equations (0.6). The asymptotic expansion is carried out by means of a multiple time scale expansion. Each quantity Q is assumed to vary according to the different time scales as follows:

$$Q(\vec{r}, t) = Q(\vec{r}, t_0, t_2, t_4, \dots) = Q(\vec{r}, t, \epsilon^2 t, \epsilon^4 t, \dots) \quad (0.9)$$

With this formal expansion, we have

$$\frac{\partial Q}{\partial t} = \frac{\partial Q}{\partial t_0} + \epsilon^2 \frac{\partial Q}{\partial t_2} + \dots \quad (0.10)$$

It is convenient for the rest of the calculation to separate the quantities Q into the sum of a rapidly oscillating part \tilde{Q} varying due to the betatron oscillations, and a slow monotonic evolution \bar{Q} due space charge and thermal effects:

$$Q(\vec{r}, t_0, t_2, \dots) = \tilde{Q}(\vec{r}, t_0, t_2, \dots) + \bar{Q}(\vec{r}, t_2, \dots) \quad (0.11)$$

Now, under the assumption that the betatron oscillations are small in amplitude, the appropriate expansion for the relevant physical quantities is the following:

$$\begin{aligned} n &= \bar{n}_0 + \epsilon(\tilde{n}_1 + \bar{n}_1) + \epsilon^2(\tilde{n}_2 + \bar{n}_2) + O(\epsilon^3) \\ p &= \bar{p}_0 + \epsilon(\tilde{p}_1 + \bar{p}_1) + \epsilon^2(\tilde{p}_2 + \bar{p}_2) + O(\epsilon^3) \\ \phi &= \bar{\phi}_0 + \epsilon(\tilde{\phi}_1 + \bar{\phi}_1) + \epsilon^2(\tilde{\phi}_2 + \bar{\phi}_2) + O(\epsilon^3) \\ \vec{v} &= \epsilon\tilde{v}_1 + \epsilon^2(\tilde{v}_2 + \bar{v}_2) + \epsilon^3(\tilde{v}_3 + \bar{v}_3) + O(\epsilon^4) \end{aligned} \quad (0.12)$$

Asymptotic analysis

We now introduce this expansion in the set of equations given by Eq.(0.6), and solve order by order in ϵ . We start with Poisson's equation. To lowest order, we have

$$\nabla^2 \bar{\phi}_0 = -\bar{n}_0 \quad (0.13)$$

As we will later see, this is all we need to know from Poisson's equation.

We now turn to the continuity equation. The first non-trivial equation comes to first order in ϵ , and we have

$$\frac{\partial \tilde{n}_1}{\partial t_0} + \nabla \cdot (\bar{n}_0 \tilde{\vec{v}}_1) = 0 \quad (0.14)$$

This equation describes the evolution of the density on the fast time scale, due to the betatron oscillations. To next order, the mass conservation equation takes the form:

$$\frac{\partial \tilde{n}_2}{\partial t_0} + \frac{\partial \bar{n}_0}{\partial t_2} + \nabla \cdot \left[(\tilde{n}_1 + \bar{n}_1) \tilde{\vec{v}}_1 + \bar{n}_0 (\tilde{\vec{v}}_2 + \bar{\vec{v}}_2) \right] = 0 \quad (0.15)$$

Averaging this equation over the fast time scale, we get, because of the periodicity of the $\tilde{}$ quantities in t_0 :

$$\frac{\partial \bar{n}_0}{\partial t_2} + \nabla \cdot \left(\langle \tilde{n}_1 \tilde{\vec{v}}_1 \rangle + \bar{n}_0 \bar{\vec{v}}_2 \right) = 0 \quad (0.16)$$

where we have introduced the notation

$$\langle Q \rangle = \frac{1}{2\pi} \int_0^{2\pi} Q dt_0$$

Eq.(0.16) describes the evolution of the bunch density on the slow time scale. This is where the influence of the electrostatic effects and the beam temperature will come in, and this is therefore all we need from the continuity equation.

In a very similar way, we obtain the following equations for the evolution of the pressure, to order ϵ and ϵ^2 :

$$\frac{\partial \tilde{p}_1}{\partial t_0} + \tilde{\vec{v}}_1 \cdot \nabla \bar{p}_0 + \gamma \bar{p}_0 \nabla \cdot \tilde{\vec{v}}_1 = 0 \quad (0.17)$$

$$\frac{\partial \bar{p}_0}{\partial t_2} + \langle \tilde{\vec{v}}_1 \cdot \nabla \tilde{p}_1 \rangle + \bar{\vec{v}}_2 \cdot \nabla \bar{p}_0 + \gamma \bar{p}_0 \nabla \cdot \bar{\vec{v}}_2 + \gamma \langle \tilde{p}_1 \nabla \cdot \tilde{\vec{v}}_1 \rangle = 0 \quad (0.18)$$

This is all we need from the energy equation. We finally look at the momentum equation. The first equation that is not trivially satisfied is of order ϵ :

$$\frac{\partial \tilde{\vec{v}}_1}{\partial t_0} + \tilde{\vec{v}}_1 \times \vec{e}_z = \vec{0} \quad (0.19)$$

This is the expected equation determining the velocity of the betatron oscillations. To next order, we have

$$\frac{\partial \tilde{\vec{v}}_2}{\partial t_0} + \tilde{\vec{v}}_1 \cdot \nabla \tilde{\vec{v}}_1 + (\bar{\vec{v}}_2 + \tilde{\vec{v}}_2) \times \vec{e}_z = -\nabla \bar{\phi}_0 - \frac{\alpha^2}{\bar{n}_0} \nabla \bar{p}_0 \quad (0.20)$$

In the same way as it was done before, we can now average over the fast time scale, to find

$$\bar{\vec{v}}_2 = \langle \tilde{\vec{v}}_1 \cdot \nabla \tilde{\vec{v}}_1 \rangle \times \vec{e}_z + \nabla \bar{\phi}_0 \times \vec{e}_z + \frac{\alpha^2}{\bar{n}_0} \nabla \bar{p}_0 \times \vec{e}_z \quad (0.21)$$

At this point, all the relevant equations have been derived. Indeed, Eq.(0.13), Eq.(0.14), Eq.(0.16), Eq.(0.17), Eq.(0.18), Eq.(0.19), and Eq.(0.21) form a set of 9 equations for the 9 unknowns $\bar{\phi}_0$, \bar{n}_0 , \tilde{n}_1 , \bar{p}_0 , \tilde{p}_1 , $\tilde{\vec{v}}_1$ and $\bar{\vec{v}}_2$.

B. Solving the equations

We now solve the set of 9 equations derived previously. The calculation can be decomposed in two parts: 1) a first part corresponding to the description of the betatron oscillations to lowest order, and their effect on the bunch pressure and the bunch density; 2) a second part describing the combined influence of the betatron oscillations and the electrostatic and temperature effects on the slow time scale evolution of the bunch density and bunch pressure.

The betatron oscillations

The subset of equations describing betatron oscillations to lowest order are repeated below for convenience:

$$\begin{aligned} \frac{\partial \tilde{\vec{v}}_1}{\partial t_0} + \tilde{\vec{v}}_1 \times \vec{e}_z &= \vec{0} \\ \frac{\partial \tilde{n}_1}{\partial t_0} + \nabla \cdot (\bar{n}_0 \tilde{\vec{v}}_1) &= 0 \\ \frac{\partial \tilde{p}_1}{\partial t_0} + \tilde{\vec{v}}_1 \cdot \nabla \bar{p}_0 + \gamma \bar{p}_0 \nabla \cdot \tilde{\vec{v}}_1 &= 0 \end{aligned} \quad (0.22)$$

The first equation in (0.22) is the equation of a particle immersed in a uniform magnetic field. It is easily solved:

$$\tilde{\vec{v}}_1(\vec{r}, t_0, t_2, \dots) = \vec{u}_1 \cos t_0 + \vec{e}_z \times \vec{u}_1 \sin t_0 \quad (0.23)$$

where $\vec{u}_1(\vec{r}, t_2, \dots)$ is the “initial” betatron velocity, i.e. \vec{v}_1 at time

$$\begin{aligned}\tilde{n}_1 &= \tilde{N}_1(\vec{r}) - \vec{\xi}_1 \cdot \nabla \bar{n}_0 - \bar{n}_0 \nabla \cdot \vec{\xi}_1 \\ \tilde{p}_1 &= \tilde{P}_1(\vec{r}) - \vec{\xi}_1 \cdot \nabla \bar{p}_0 - \gamma \bar{p}_0 \nabla \cdot \vec{\xi}_1\end{aligned}$$

The second and third equations in (0.22) are most easily solved by introducing the displacement vector $\vec{\xi}_1(\vec{r}, t_0, t_2, \dots)$ associated with the betatron oscillations, defined by

$$\vec{v}_1 = \frac{\partial \vec{\xi}_1}{\partial t_0}; \quad \vec{\xi}_1(\vec{r}, t_0 = 0, t_2, \dots) = \vec{0} \quad (0.24)$$

Indeed, the second equation in (0.22) then takes the form:

$$\frac{\partial}{\partial t_0} \left[\tilde{n}_1 + \nabla \cdot (\bar{n}_0 \vec{\xi}_1) \right] = 0 \quad (0.25)$$

and the third equation in (0.22) is

$$\frac{\partial}{\partial t_0} \left(\tilde{p}_1 + \vec{\xi}_1 \cdot \nabla \bar{p}_0 + \gamma \bar{p}_0 \nabla \cdot \vec{\xi}_1 \right) = 0 \quad (0.26)$$

These two equations can be solved immediately:

$$\begin{aligned}\tilde{n}_1 &= \tilde{N}_1(\vec{r}) - \vec{\xi}_1 \cdot \nabla \bar{n}_0 - \bar{n}_0 \nabla \cdot \vec{\xi}_1 \\ \tilde{p}_1 &= \tilde{P}_1(\vec{r}) - \vec{\xi}_1 \cdot \nabla \bar{p}_0 - \gamma \bar{p}_0 \nabla \cdot \vec{\xi}_1\end{aligned} \quad (0.27)$$

where \tilde{N}_1 and \tilde{P}_1 are the initial density and pressure of the bunch at time $t_0 = 0$. $\vec{\xi}_1$ is just as easily calculated, by integrating Eq.(0.24) using (0.23). We find

$$\vec{\xi}_1 = \vec{u}_1 \sin t_0 + \vec{u}_1 \times \vec{e}_z (\cos t_0 - 1) = (\vec{v}_1 - \vec{u}_1) \times \vec{e}_z \quad (0.28)$$

We thus showed how to calculate \vec{v}_1 , \tilde{n}_1 and \tilde{p}_1 . Since we now know \tilde{n}_1 , we could also compute $\tilde{\phi}_1$, through Poisson's equation, $\nabla^2 \tilde{\phi}_1 = -\tilde{n}_1$, and we would therefore know all the physical quantities associated with the betatron motion to lowest order.

As we will see in the next section, it turns out that $\tilde{\phi}_1$ is not necessary to determine what we are really interested in: the slow time scale evolution of the

lowest order density \bar{n}_0 and lowest order pressure \bar{p}_0 due to space-charge and temperature effects.

The slow time scale evolution

In this section we use the results derived in the previous section, describing the betatron motion to lowest order, to determine the equations which we will have to solve to determine the evolution of the bunch density and pressure on the slow time scale.

We start with the time-averaged (over the fast time scale) density equation, Eq.(0.16), repeated here for convenience:

$$\frac{\partial \bar{n}_0}{\partial t_2} + \nabla \cdot (\langle \tilde{n}_1 \tilde{v}_1 \rangle + \bar{n}_0 \bar{v}_2) = 0$$

where \bar{v}_2 was given by Eq.(0.21):

$$\bar{v}_2 = \langle \tilde{v}_1 \cdot \nabla \tilde{v}_1 \rangle \times \vec{e}_z + \nabla \bar{\phi}_0 \times \vec{e}_z + \frac{\alpha^2}{\bar{n}_0} \nabla \bar{p}_0 \times \vec{e}_z$$

Using the results derived previously, we find

$$\langle \tilde{n}_1 \tilde{v}_1 \rangle = \frac{1}{2} \left[\nabla \cdot (\bar{n}_0 \vec{u}_1) \vec{u}_1 \times \vec{e}_z - \nabla \cdot (\bar{n}_0 \vec{u}_1 \times \vec{e}_z) \vec{u}_1 \right] \quad (0.29)$$

and

$$\langle \tilde{v}_1 \cdot \nabla \tilde{v}_1 \rangle \times \vec{e}_z = \frac{1}{2} \left[\vec{u}_1 \cdot \nabla \vec{u}_1 + (\vec{e}_z \times \vec{u}_1) \cdot \nabla (\vec{e}_z \times \vec{u}_1) \right] \times \vec{e}_z \quad (0.30)$$

Combining Eq.(0.29) and Eq.(0.30), we find:

$$\langle \tilde{n}_1 \tilde{v}_1 \rangle + \bar{n}_0 \langle \tilde{v}_1 \cdot \nabla \tilde{v}_1 \rangle \times \vec{e}_z = \frac{1}{2} \nabla \times (\bar{n}_0 u_1^2 \vec{e}_z) \quad (0.31)$$

This is a very nice result: it shows that when we order the betatron oscillations as small (they only come to first order in our expansion), they do not play any role in the slow time evolution of the bunch! Indeed, the divergence of a curl is always zero, so Eq.(0.16) can now be written

$$\begin{aligned} \frac{\partial \bar{n}_0}{\partial t_2} + \nabla \cdot (\bar{n}_0 \nabla \bar{\phi}_0 \times \vec{e}_z) + \alpha^2 \nabla \cdot (\nabla \bar{p}_0 \times \vec{e}_z) &= 0 \\ \Leftrightarrow \frac{\partial \bar{n}_0}{\partial t_2} + \nabla \bar{\phi}_0 \times \vec{e}_z \cdot \nabla \bar{n}_0 &= 0 \end{aligned} \quad (0.32)$$

This is another interesting result. It shows that to lowest order, the slow time evolution of the bunch density is *not* influenced by temperature effects. This is a direct consequence of the choice we made for the pressure equation. By assuming that the pressure was isotropic, we reduced the divergence of the pressure tensor to the gradient of the scalar quantity \bar{p}_0 . And the term $\nabla \bar{p}_0 \times \vec{e}_z$ which appears in the density equation can be written as a curl, which is obviously divergence free.

The bottom line is that to determine the slow evolution of the bunch density, we only have to solve the following two coupled equations:

$$\begin{aligned} \frac{\partial \bar{n}_0}{\partial t_2} + \nabla \bar{\phi}_0 \times \vec{e}_z \cdot \nabla \bar{n}_0 &= 0 \\ \nabla^2 \bar{\phi}_0 &= -\bar{n}_0 \end{aligned} \quad (0.33)$$

Note that the slow time evolution of the bunch pressure can also be obtained by evaluating all the terms in Eq.(0.18), i.e. $\langle \tilde{v}_1 \cdot \nabla \tilde{p}_1 \rangle$, $\tilde{v}_2 \cdot \nabla \bar{p}_0$, $\gamma \bar{p}_0 \nabla \cdot \tilde{v}_2$, $\gamma \langle \tilde{p}_1 \nabla \cdot \tilde{v}_1 \rangle$, using the expressions given in Eqs.(0.23), (0.27), and (0.28). After some straightforward but slightly tedious algebra, one finds:

$$\frac{\partial \bar{p}_0}{\partial t_2} + \left(\nabla \bar{\phi}_0 + \gamma \frac{p_0}{n_0} \alpha^2 \nabla \bar{n}_0 \right) \times \vec{e}_z \cdot \nabla \bar{p}_0 = 0 \quad (0.34)$$

In principle, after calculating the evolution of \bar{n}_0 and $\bar{\phi}_0$ for all time steps, we could evolve \bar{p}_0 using Eq.(0.34). However, the information we would get from doing this would be limited, and perhaps even misleading. Indeed, the energy equation we used for the closure of the fluid equations (the third equation in (0.6)) is hard to justify in the physical regime of interest.

E.6 Numerical results

In this section, we show the results we obtained when numerically solving the equations for the evolution of the bunch density on the slow time scale. For convenience, we repeat here these two equations:

$$\begin{aligned} \frac{\partial \bar{n}_0}{\partial t_2} + \nabla \bar{\phi}_0 \times \vec{e}_z \cdot \nabla \bar{n}_0 &= 0 \\ \nabla^2 \bar{\phi}_0 &= -\bar{n}_0 \end{aligned} \quad (0.35)$$

The first equation in Eq.(0.35) has a simple interpretation: it describes the convection of the density profile in the velocity field $\vec{E} \times \vec{B} / B^2$, the so-called

$\vec{E} \times \vec{B}$ velocity (there is no - sign in front of $\nabla \bar{\phi}_0$ because the Lorentz force is in the opposite direction in the moving frame, see Eq.(0.6)).

This is not very surprising. In the absence of accelerating gaps, the effect of the betatron oscillations on the density profile averages out to zero on the slow time scale. Thus, the density profile simply follows the slow, averaged motion of the ions. In a homogeneous magnetic field, in the presence of an electric field created by the charges in the bunch themselves, this slow motion is just the $\vec{E} \times \vec{B}$ motion.

A. Numerical method

In order to solve Eq.(0.35) numerically, we first rewrite it in conservative form:

$$\begin{aligned} \frac{\partial \bar{n}_0}{\partial t_2} + \nabla \cdot (\bar{n}_0 \nabla \bar{\phi}_0 \times \vec{e}_z) &= 0 \\ \nabla^2 \bar{\phi}_0 &= -\bar{n}_0 \end{aligned} \tag{0.36}$$

The first equation in (0.36) is hyperbolic, and we integrate it using a scheme known as the *leap-frog method*, which has the advantage of being non-dissipative. At each time step, the density profile changes, so the electrostatic potential has to be recalculated. We use the integral form of Poisson's equation (second equation in Eq.(0.36)) to perform this task.

For the boundary conditions, we assume that at any time step, the density is exactly zero on all the edges of the computational domain.

Note that the integration of Poisson's equation is the step which is the most time consuming in the numerical procedure. In order to keep the computing time somewhat low, we have decided to assume that the beam is two-dimensional, and infinite in the z -direction. Since for our analysis we have already assumed that $v_z = 0$ at all times, this additional simplification should not significantly change the beam dynamics. And reducing the numerical integration from three dimensions to two dimensions represents a substantial gain in computing time.

Because the bunch is now considered to be infinite in the z -direction, a round bunch will be called *cylindrically symmetric*, as we will see in the next section.

B. Numerical results: Cylindrical bunch

If we start with a bunch density profile which is cylindrically symmetric, i.e. such that the bunch density is only a function of the distance from the center of the bunch ($\bar{n}_0 = \bar{n}_0(r)$), then the initial electrostatic potential due to the charges in the

bunch will also be cylindrically symmetric: $\bar{\phi}_0 = \bar{\phi}_0(r)$. This implies that the initial electric field will be purely in the radial direction: $\vec{E} = E_r \vec{e}_r$. And the convective velocity $\nabla \bar{\phi}_0 \times \vec{e}_z$ will be purely in the azimuthal direction, i.e. in the \vec{e}_θ direction. We thus expect the density profile to rotate around the center of the bunch. Since this density profile is cylindrically symmetric, a rotation of the profile around the center will leave the profile invariant. In other words, the space charge forces on a cylindrically symmetric bunch in a purely drifting region are such that the bunch properties are kept constant.

These predictions are confirmed by the numerical simulations. In Figure E.1, we see the initial profile of the normalized bunch density; in Figure E.2 it is the density profile after 100 revolutions; Figure E.3 shows the profile after 500 revolutions, and Figure E.4 the profile after 1000 revolutions. It is clear that apart from the very small differences which are associated with the error due to the numerical leap-frog scheme, the bunch profiles are exactly identical in all four cases.

C. Numerical results: Elliptic bunch

The situation is different for an elliptic bunch, since the cylindrical symmetry is then broken. Nevertheless, the electric field far away from the bunch still has cylindrical symmetry (far away, the bunch is seen as a point charge). We thus expect the $\vec{E} \times \vec{B}$ convection to act in such a way as to make the bunch conform with this cylindrical symmetry. This is precisely what happens in the numerical simulation.

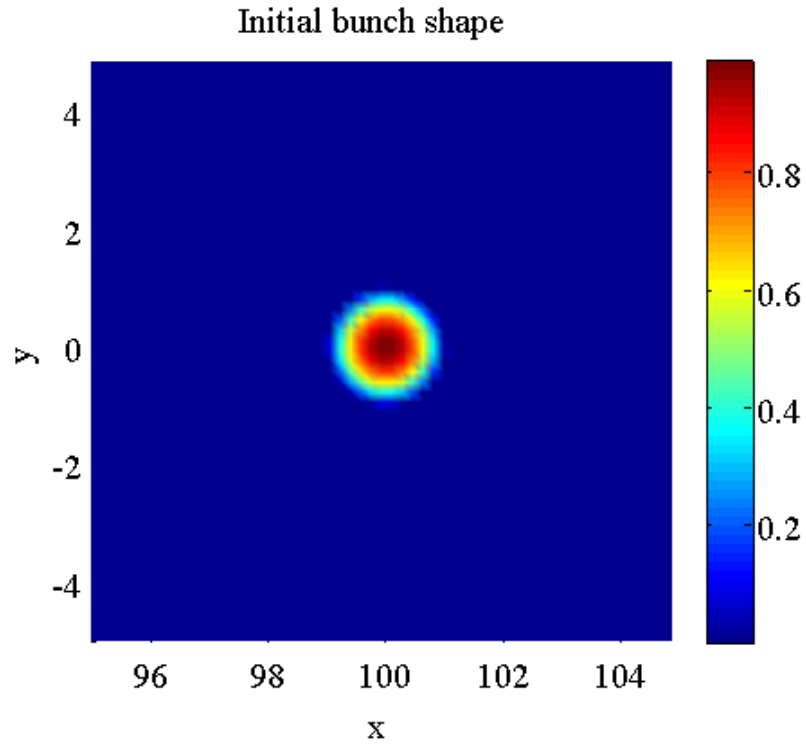


Figure E.1. Initial bunch density profile - cylindrically symmetric case

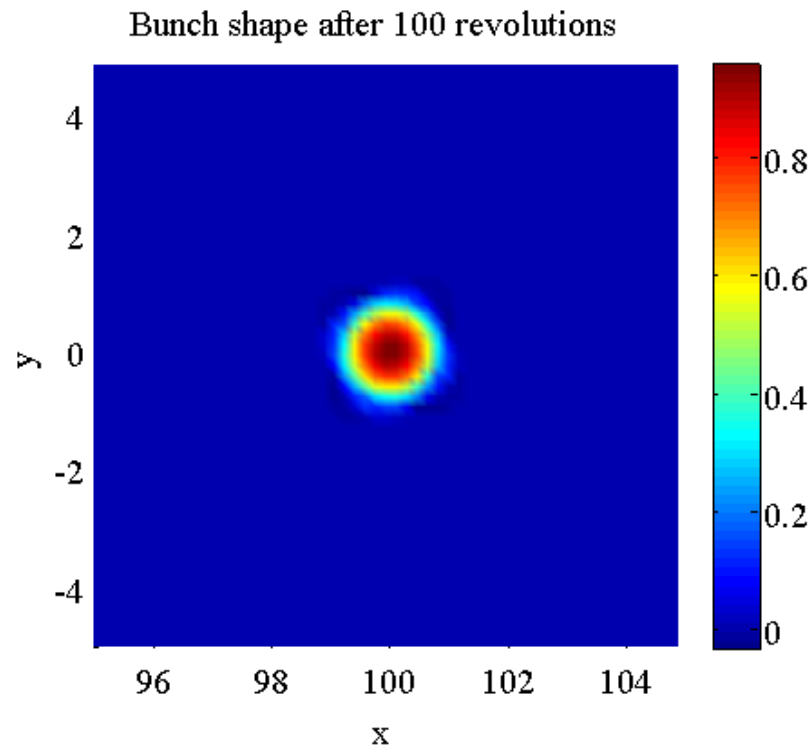


Figure E.2. Bunch density profile after 100 revolutions - cylindrically symmetric case

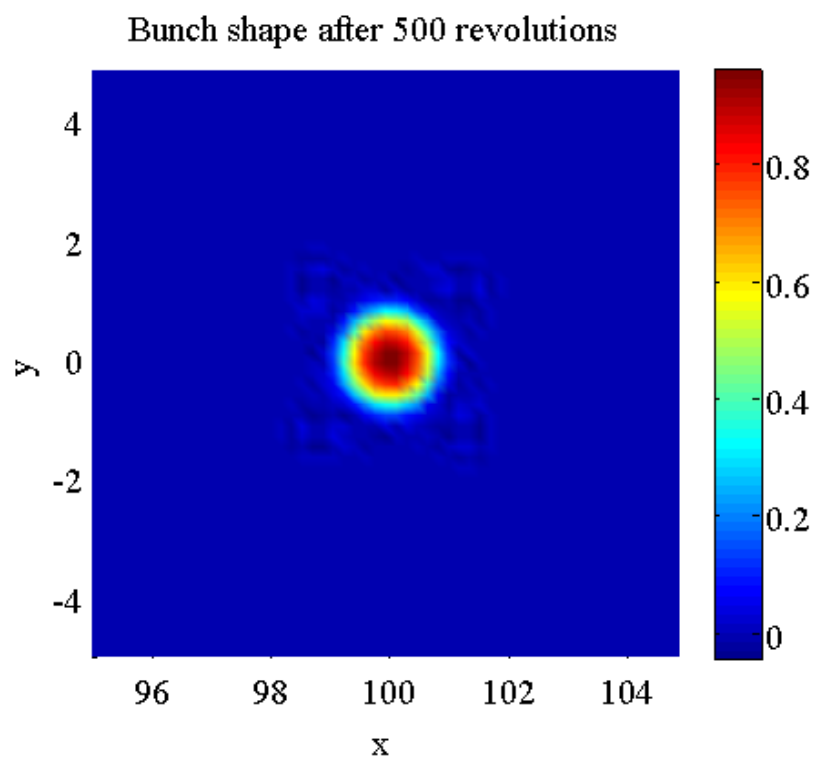


Figure E.3. Bunch density profile after 500 revolutions - cylindrically symmetric case

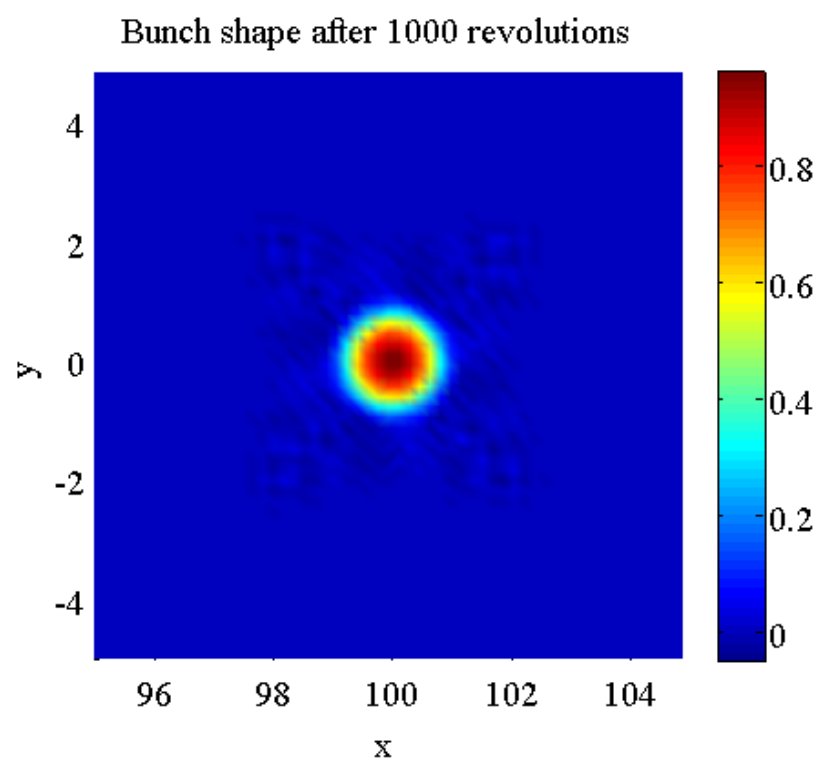


Figure E.4. Bunch density profile after 1000 revolutions - cylindrically symmetric case

We start with an elliptically shaped density profile, as shown in Figure E.5. The $\vec{E} \times \vec{B}$ convection then distorts and rotates the bunch, as we can see in Figure E.6 (snapshot taken after 100 cyclotron revolutions) and Figure E.7 (500 revolutions). After about 1000 revolutions, the bulk of the bunch has already reached a shape that is nearly cylindrically symmetric, and a small part of the bunch fills “galactic arms” (Figure E.8). These qualitative features are kept until the end of the simulations, so that after 2000 revolutions, the bulk of the bunch density profile is almost perfectly cylindrically symmetric, and the rest of the bunch is in the galactic arms which have extended further, and are closing on themselves (Figure E.9 and Figure E.10).

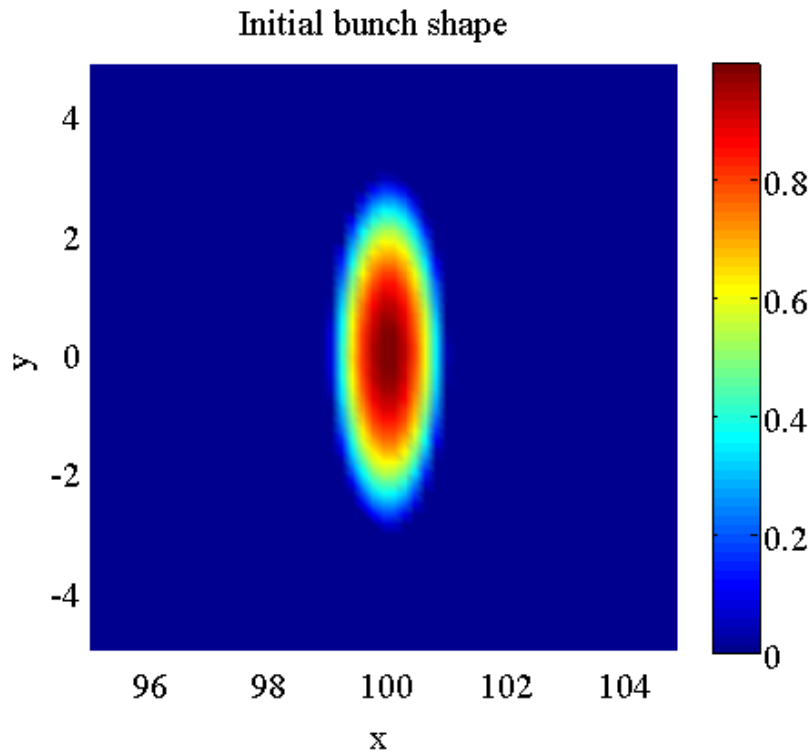


Figure E.5. Initial bunch density profile - Elliptic initial density profile

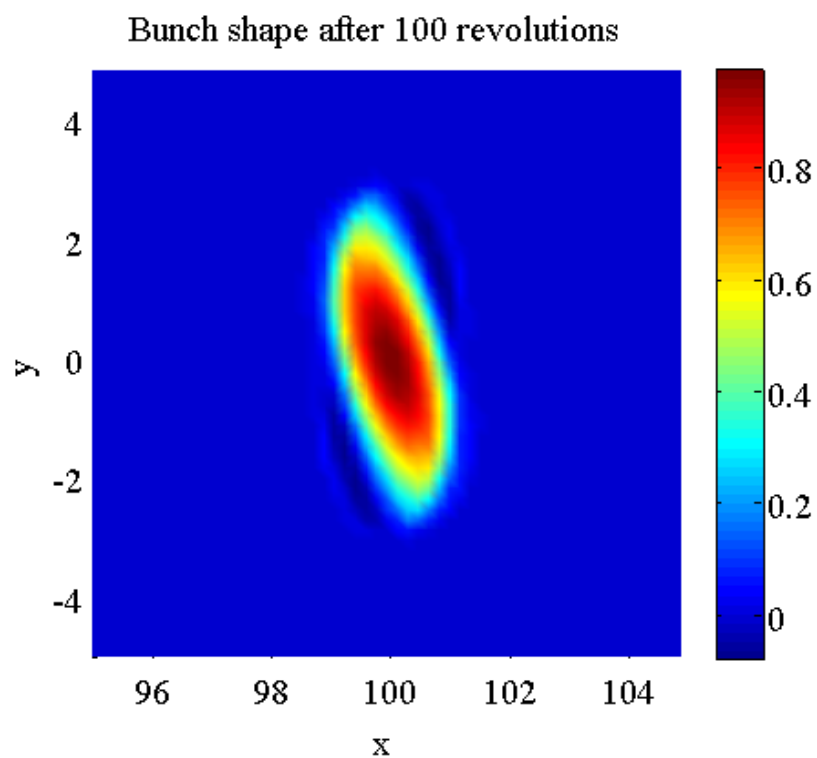


Figure E.6. Bunch density profile after 100 revolutions - Elliptic initial density profile

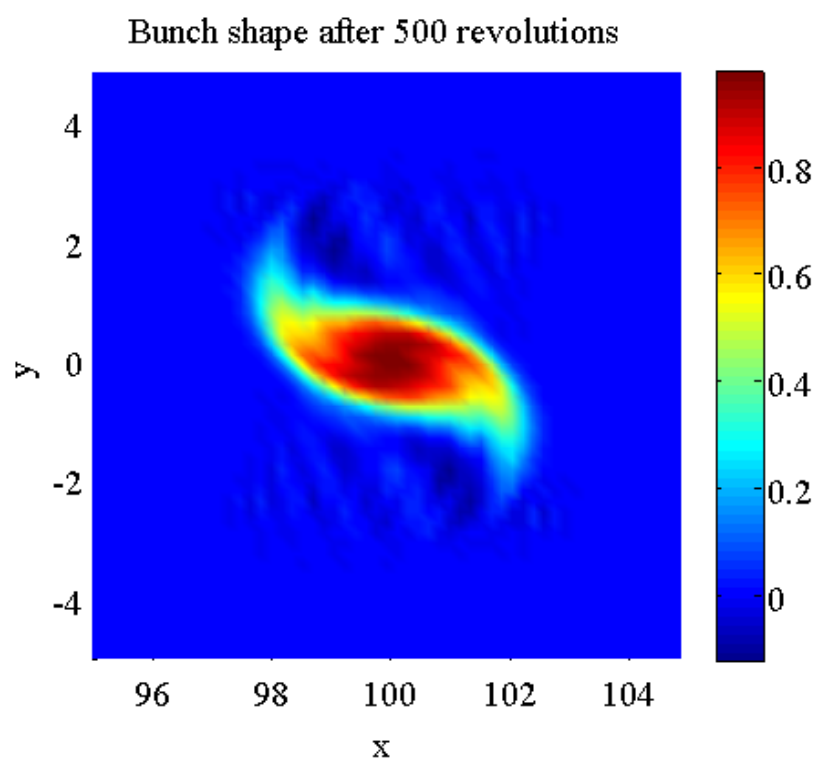


Figure E.7. Bunch density profile after 500 revolutions - Elliptic initial density profile

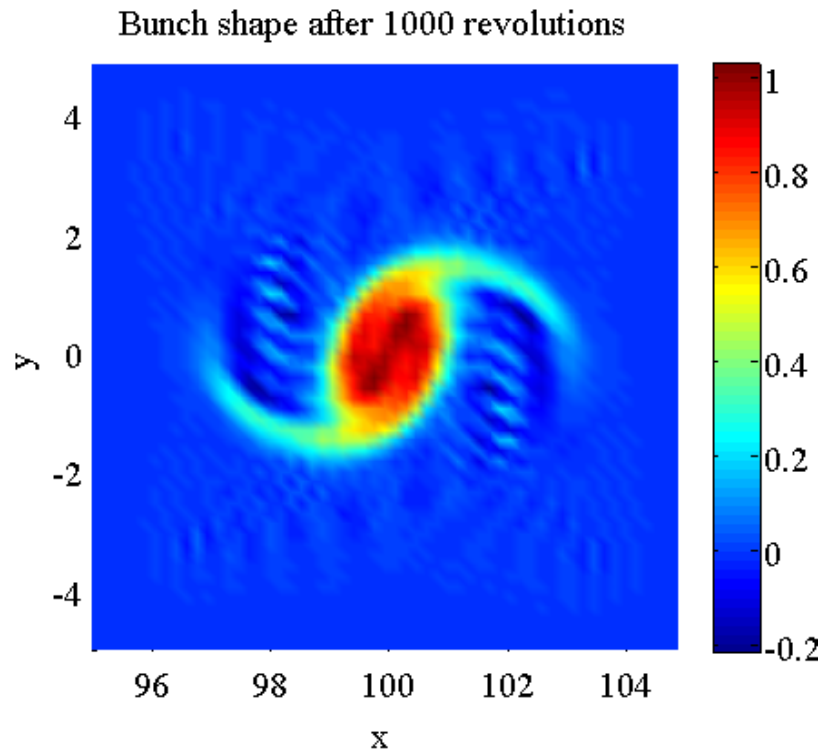


Figure E.8. Bunch density profile after 1000 revolutions - Elliptic initial density profile

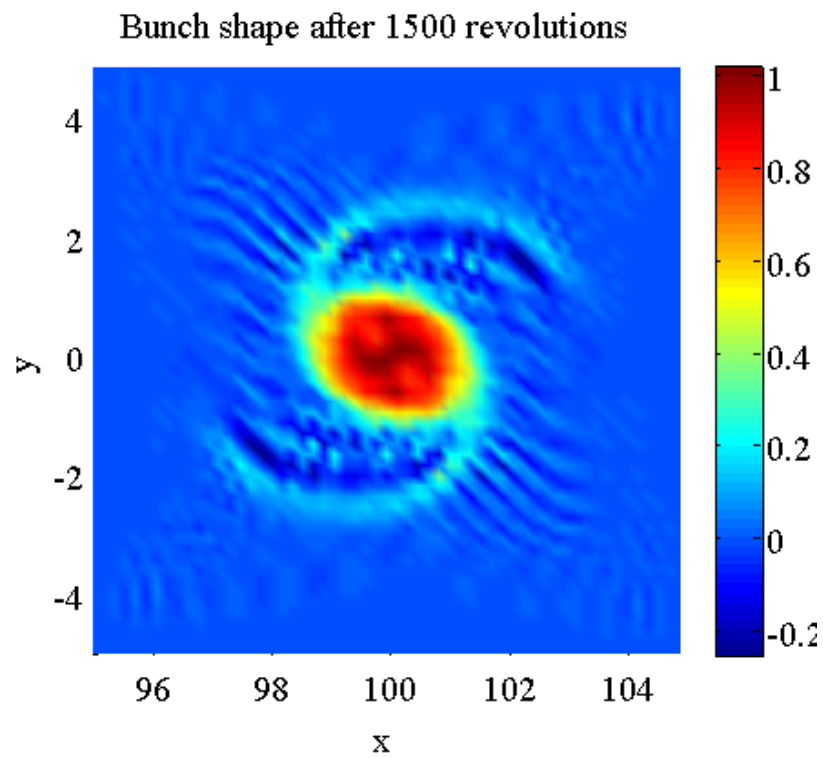


Figure E.9. Bunch density profile after 1500 revolutions - Elliptic initial density profile

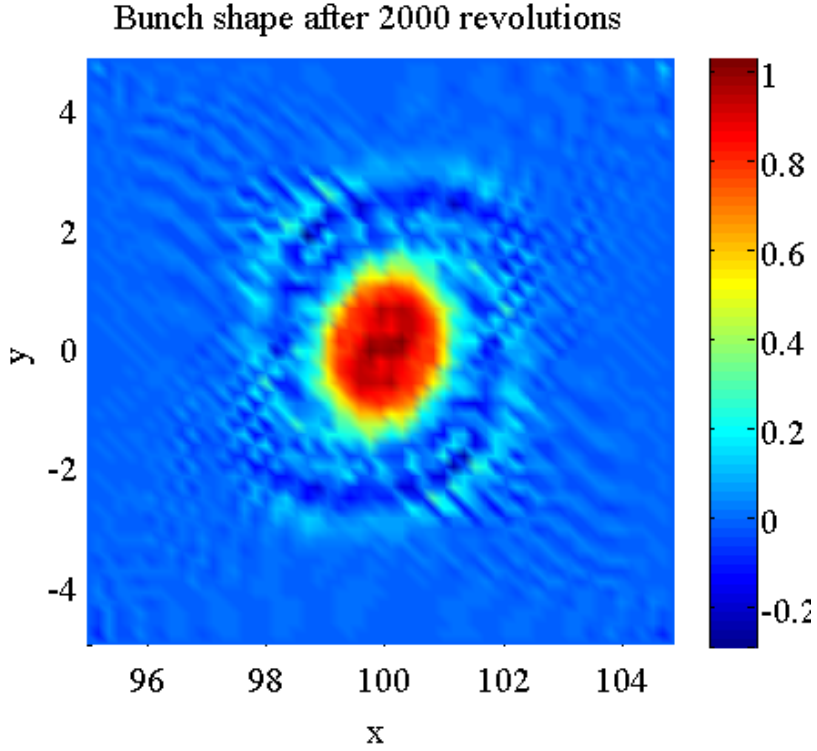


Figure E.10. Bunch density profile after 2000 revolutions - Elliptic initial density profile

E.7 Future plans

The simple 2D warm fluid model of a drifting bunch we considered here gave us some important insights on the role of space-charge forces in the drift sections of high beam intensity cyclotrons. Specifically, we have been able to highlight the fundamental role of the $\vec{E} \times \vec{B}$ convection in the deformation of the bunch.

Our goal is to extend this analysis to describe situations in better match with the MEGATRON experiment. Below, we describe the steps we will take towards that goal:

- Inclusion of the accelerating gaps
- Kinetic description of the bunch, in order to identify possible effects due to temperature anisotropies and phase-space instabilities
- Inclusion of the dynamics in the direction along the magnetic field
- Inclusion of the spatial dependence of the external magnetic field
- Inclusion of relativistic effects

F. Ion Sources Of High Current Proton Cyclotrons

For applications to compact cyclotrons, efficient ion sources are needed. Requirements are stability, sufficient life time, low gas requirements, high ionization, and for some applications, high ratio of H^+ to H^{2+} . In this program, a Hollow cathode Discharges was discussed.

F.1 Hollow Cathode Discharges

Hollow cathode discharges have been used for about 40 years as simple means of efficiently producing high density, stable, steady state plasmas in a range of gases. Although most commonly used gases are mixtures of Argon and hydrogen, it is possible to use hydrogen alone.

These type of sources have high gas ionization efficiency, decreasing the pumping needs. Because of the high density, on the order of a few times $10^{13}/\text{cm}^3$, these sources are ideal of use in high current cyclotrons.

The geometry of the source is shown in Figure F.1. The source consists of a hollow tube, about 3 mm diameter (1/8 in) when operating at or near atmospheric pressure, made of a refractory metal, such as tantalum. Due to ion bombardment, areas of the tantalum tube (which operates as the cathode) become very hot, and become a source of thermionic emission of electrons. As the electrons travel down the tube they ionize the background gas. Because of the high temperature, the number density of neutrals is down (at constant pressure) and the gas viscosity is high. This allows the support of a large pressure difference between the region upstream from the plasma to the regions downstream from the hot cathode. Pressure differentials of 3-4 orders of magnitude are feasible. However, it is likely that the limit pressure occurs when the Knudsen number becomes close to one, that is, when the gas flow becomes molecular and fluid viscosity decreases. This occurs at pressures on the order of a few mTorr, and substantial vacuum pumping will be required to remove the residual gas. However, one advantage of this approach is that the gas jet that can be generated by the nozzle is severely disrupted, eliminating the presence of a supersonic gas stream that is mostly-forward directed as is the case with more diffuse ion sources.

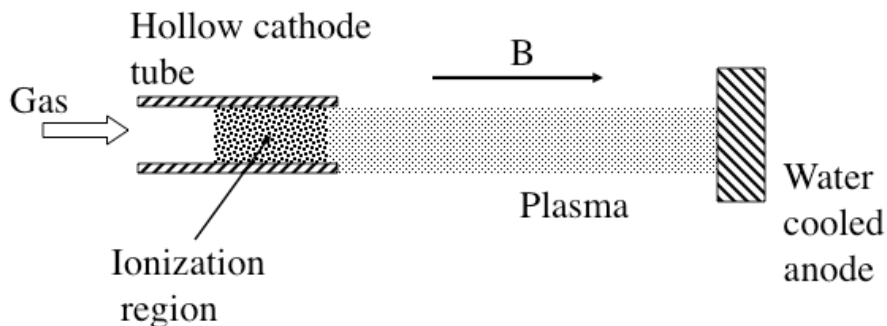


Figure F.1 Hollow cathode ion source.

The HCD sources are relatively simple and inexpensive, but they have reliability issues. The cathode lasts 10's of hours, on average, but with substantial spread. The loss of cathode is statistical, which means that the cathode may have to be replaced, in a small number of cases, after short operating time. Thus periodic maintenance of the unit must be performed. And there are issues of plasma startup, as a substantial damage to the electrode happens during the current startup.

There are alternative means for starting the plasma that does not require the large voltage breakdown, which in a few cases destroys the cathode. An electron beam could be introduced through the center of the hollow cathode, from an external, thermionic source. The purpose of this cathode is to lower the breakdown voltage. It only needs to be energized during the start up, but we would investigate the performance during steady state to see if it aids in stabilization of the HCD discharge, and maybe even allow the operate at lower cathode temperatures (which should increase the life of the cathode).

Figure F.2 shows a cathode from an HCD. Large amount of erosion has occurred, to the point where it is no longer a cylinder. This cathode was exposed to an Ar-Cu plasmas, at 1 Torr and at 200 mA, after only 15 hours. [Reproduced from P. J. Slevin and W. W. Harrison, *Appl. Spectrosc. Reviews* **10**, 201 (1975)]



Figure F.2 Cathode after 15 hours of operation.

F.2 Status and summary

We have carried an extensive search of the limitations of the cathodes for the HCD. It has been determined that tantalum is the best material, in terms of durability. However, it is estimated that the lifetime of these cathodes can be measured in

hours and in a few cycles (meaning less than 10). Thermal transients during transients (start-ups/shutdown) seem to be the reason for the short cyclic lifetime.

Although this plasma is ideal for the cyclotron application (very high ion density, high protonic concentration, high gas efficiency), we have determined that this source is not applicable to cyclotron applications, which require stable operation during substantial lengths of time, because of the cathode lifetime.

F.3 Electron Cyclotron Resonance Ion Source.

A. Source Design and Assembly

Microwave heating of electrons bypasses the complications of providing for a hot cathode and supplying anode power. It also minimizes impurity generation from exposure of metal wall electrodes to energetic ions in the hot plasma.

The mechanical design is based upon a 2.54 GHz electron resonant heated plasma in the presence of an axial magnetic field. The assembly is currently in vacuum testing after issues involving vacuum integrity and high voltage have been addressed. In particular, seals are now made with elastomers instead of Indium wire while the design of the high voltage break in the waveguide has been modified.

Figures F.3 and F.4 show details of the ion source being built. This unit will be tested later in the third year, and in the option I, if continued.

The water cooled coils have been wound and are waiting to be tested. It should be noted that the purpose of using water cooled coils is to provide flexibility to the measurements. Once the source parameters have been optimized, a magnetic design using permanent magnets will be used.

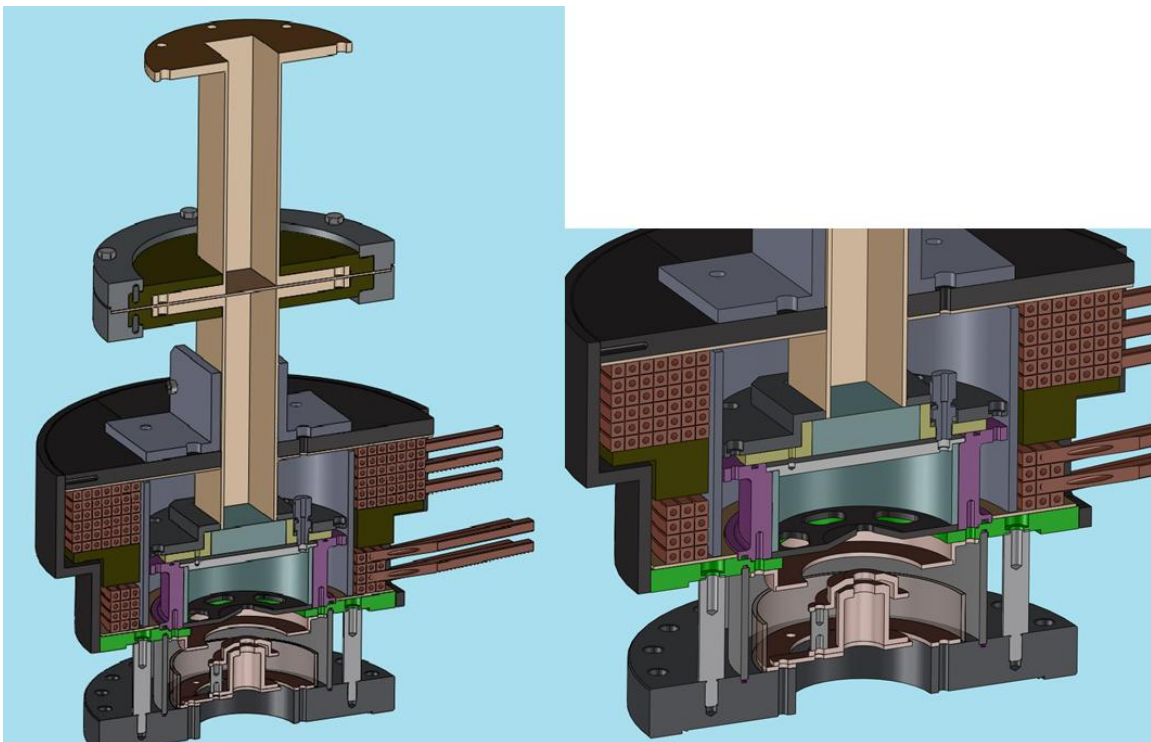


Figure F.1 CAD isometric model of the modified ion source being built.

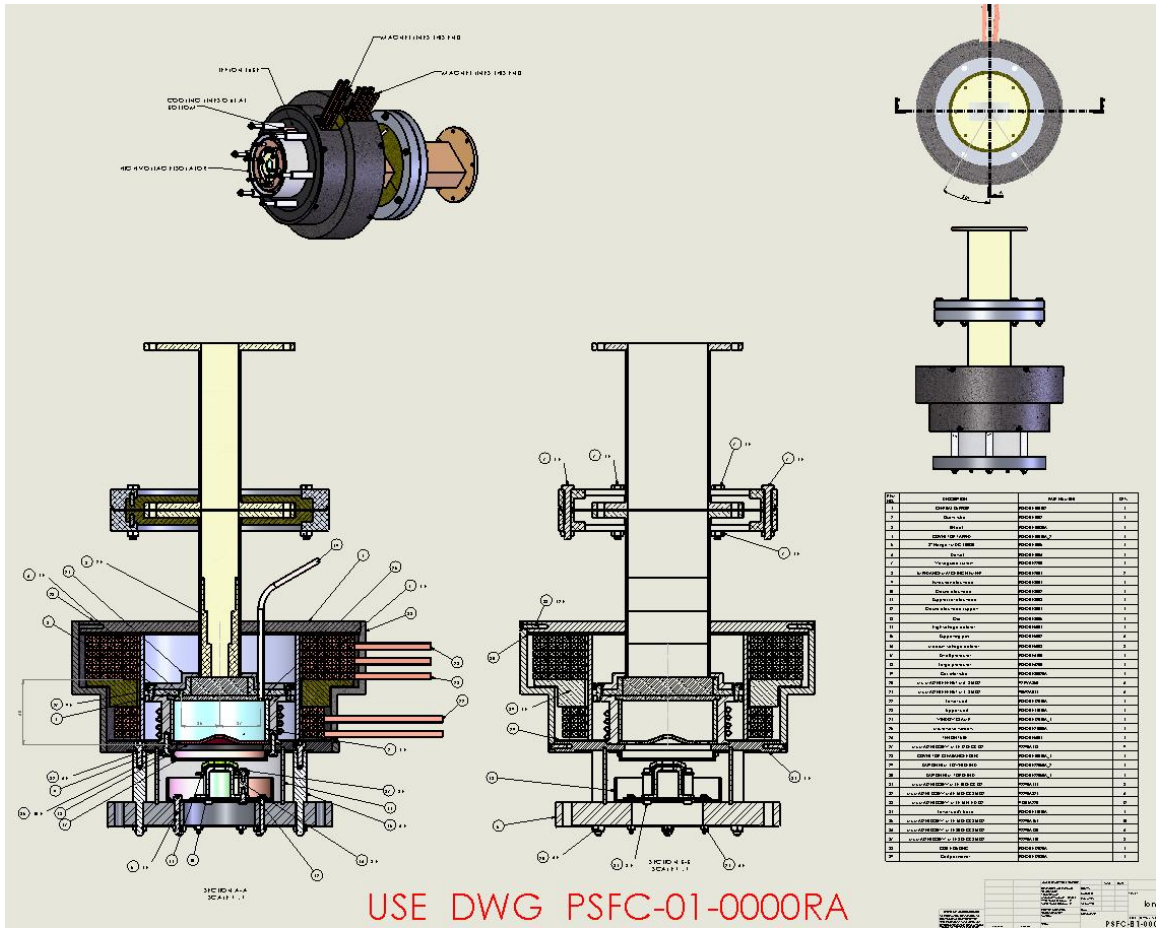


Figure F.2 CAD model of the ion source.

B. Power Supplies

The RF generator is in-house. The equipment consists of 1.2 kW 2.5 GHz generator with dummy load and circulator. It has been operated at low power into a dummy load. RF leakage at waveguide joints has been quantified with a field meter. We may need a 3-stub tuner for Z matching of the ionizer chamber to the RF source. However, our experience is that once the plasma has been created, the plasma load removes the need for matching network. We may need it only for the initial breakdown.

Extraction power supply (30 kV, 50 mA), electron suppressor supply, and magnet supplies are also in house.

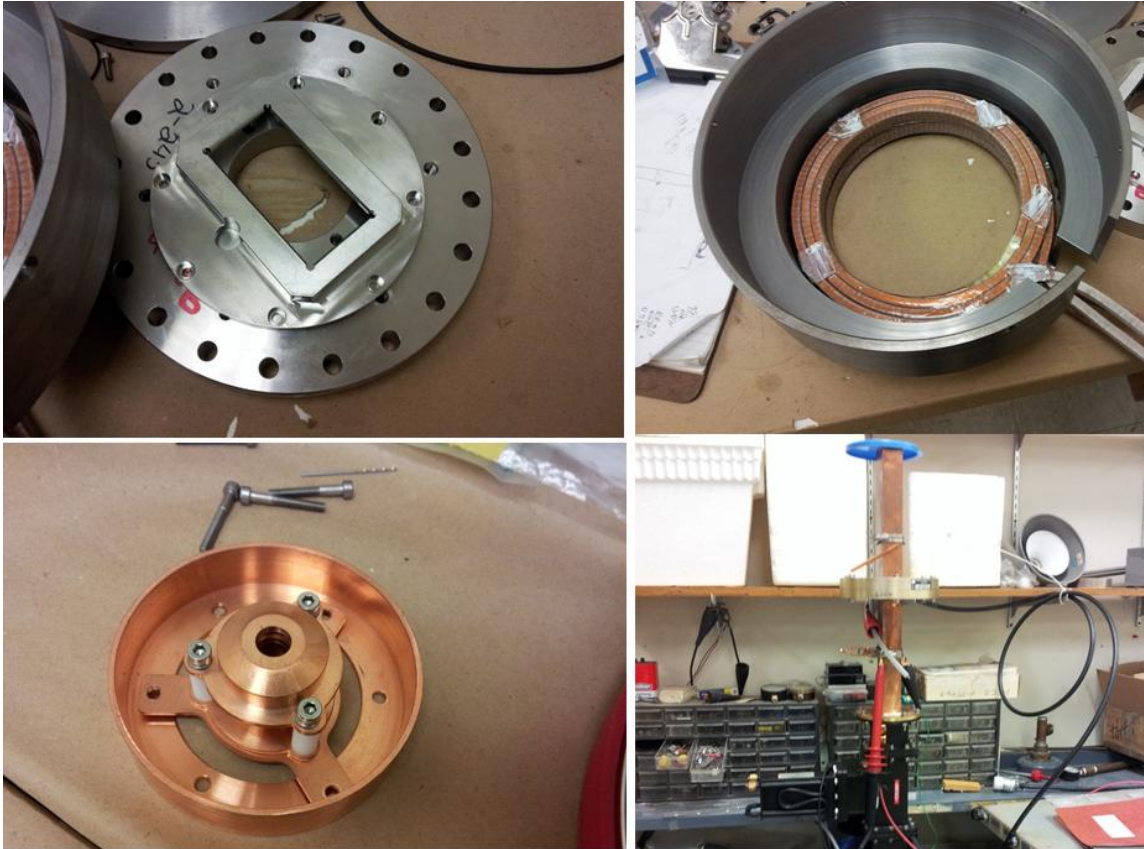


Figure F.5 shows some of the components for the ion source to be tested. Top left shows the sapphire window in the microwave waveguide, the top right shows the magnetic shield with the small coils, the bottom left shows the extractor and bottom right the test rig for testing the microwave source and the dummy load.

C. Characterization of the Ion Beam

The ion source will be placed on top of a 7 Tesla superconducting magnet test facility available for this program. Figure F.6 and F.7 show the magnetic field lines and the magnetic field contours, respectively, for a source with a magnetic shield.

Initially, the extracted beam intensity and shape will be monitored with a retractable, segmented Faraday cup currently in design stage. These measurements will allow us to “tune” the ion source

Once ion source-extractor operation is documented, the beam will be injected into the 4 in bore of the large magnet. Diagnostics placed inside the magnet bore will be used to characterize beam emittance.

Measured characteristics of the ion beam – intensity, proton fraction, and emittance - will be compared with simulations. Modeling of the plasma generator is described below.

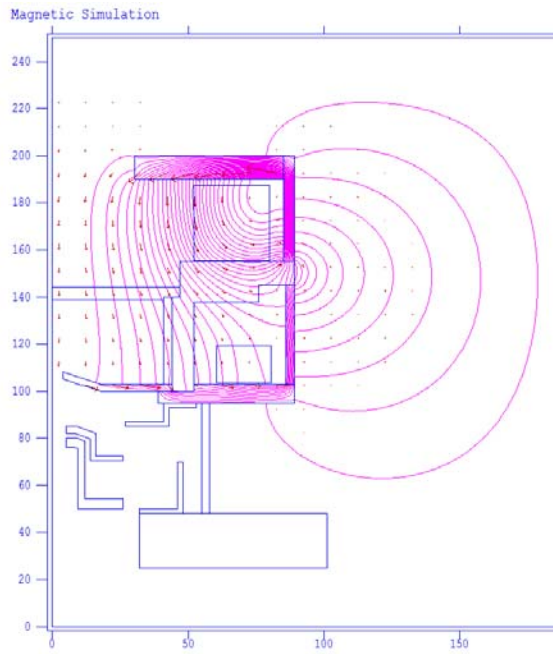


Figure F.6 Magnetic field surrounding the source, with the magnetic shielding

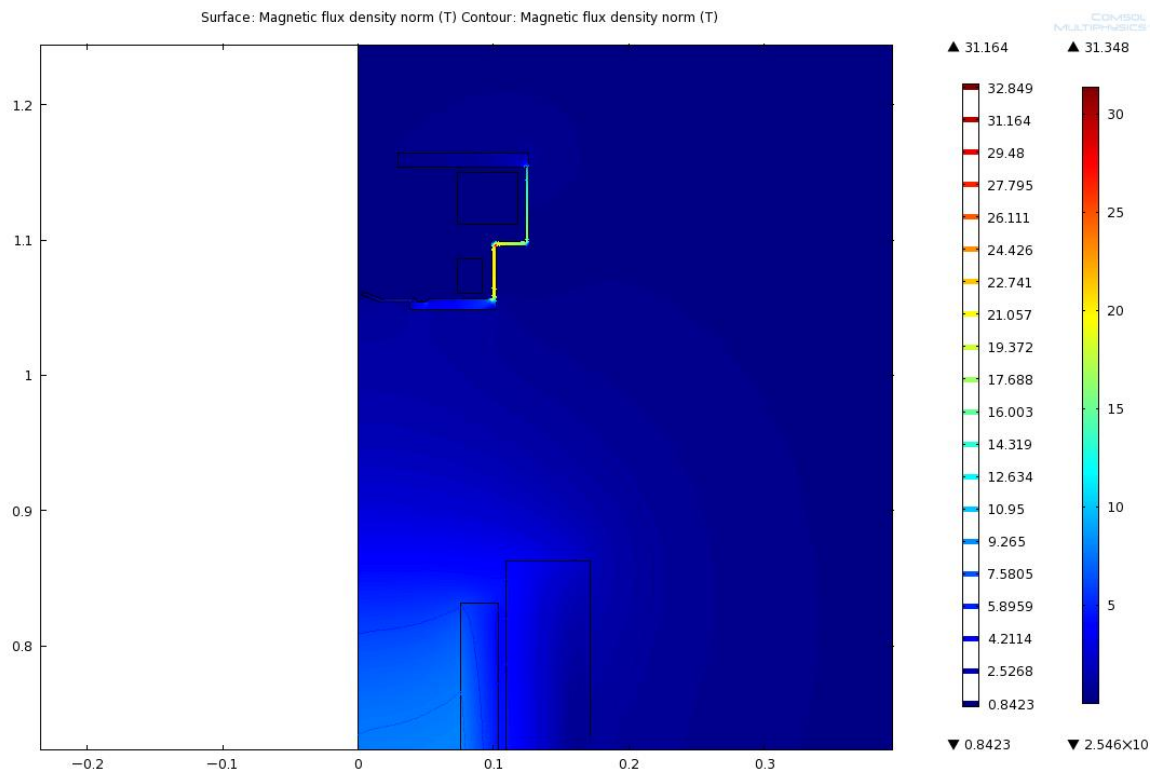


Figure F.7 Magnetic field contours of the superconducting magnet in the region below the ion source. The magnetic shield of the ion source can be seen in the top left of the figure.

We are in the process of modeling the source. The most important information that we expect to obtain is the composition of the extracted ions (protons vs molecular hydrogen ions), as well as ion temperature.

F.4 Theory of ion composition for low pressure discharges

In this task, we propose to model the performance of the source, including the ion species. For applications where the beam is not analyzed (as in a bending magnet), it is of interest to maximize the production of the single charge ions, as others are just increasing the space charge from the critical central region of the cyclotron.

Low-pressure discharges can be used to produce better, optimized plasma sources from which to extract many amperes of positive ions. One of the recently developed sources is the ECRIS. However, there has been no theoretical model that predicts its performance, including protonic charge species. There has been substantial modeling to understand the highly-charged composition of the source, but not to determine the composition of protonic species.

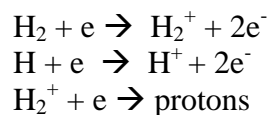
Theoretical models for several high pressure (~100 mTorr) discharges have been developed during the past two decades. However, the theory is not developed to the extent that the plasma characteristics can be described self-consistently, and several parameters need to be experimentally determined.

For low pressure discharges, the situation is different. The theory of these discharges has received relatively little attention. We have developed a relatively simple model from which we can predict the discharge current, plasma density and plasma electron temperature. In a low pressure, extending the theory to several ion species.

The gas can be either hydrogen or deuterium. The pressure is 10-20 mTorr. The extracted ion beam is composed of H^+ , H_2^+ , H_3^+ , with about 60-80% of the current being H^+ .

Mathematical Formulation of the Model

The spatially dependent ion densities and speeds are calculated using a simplified one-dimensional model, instead of the zero-dimensional model used before [A. R. Martin and T. S. Green, Culham Lab. Report CLM-R169 (1976) (as the experimentally measured radial gradients are small. The one dimensional approximation is good), We assume only two ion species, H^+ and H_2^+ , We neglect the presence of H_3^+ because the proton yield is not very dependent on the H_3^+ density (at the pressure at which the source operates), In the case of hydrogen, the important processes are



The cross sections for these processes are taken from Brown 14 and Peart 15, Other

possible processes have been neglected because of small cross sections, We assume that the electrons doing the ionization are fast electrons, accelerated by the RF but that the proton production from H_2^+ is due mainly to plasma electrons, since this process requires < 3 eV (depending on the vibrational state of the molecule).

The one dimensional moment equations for two collisionless ion species are

$$\frac{d}{dz} n_{1i} v_1 = G_1 + G_{21}$$

$$\frac{d}{dz} n_{2i} v_2 = G_2 - G_{21}$$

for the first moments and

$$n_{1i} v_1 \frac{dv_1}{dz} + v_1 (G_1 + G_{21}) = -\frac{e}{M} n_{1i} \frac{d\phi}{dz} - \nu_1 n_{1i} v_1$$

$$n_{2i} v_2 \frac{dv_2}{dz} + v_2 (G_2 - G_{21}) = -\frac{e}{2M} n_{2i} \frac{d\phi}{dz} - \nu_2 n_{2i} v_2$$

for the second moments, where

$$G_1 = n_p n_{o1} \sigma_1 v_p$$

$$G_2 = n_p n_{o2} \sigma_2 v_p$$

$$G_{21} = n_e n_{2i} \langle \sigma_{21} v_e \rangle$$

For the plasma electrons, we assume a Maxwellian distribution, while there is a fast, partially decoupled population of fast electrons driven by the RF (in the case of the ECRIS). Here n_{1i} , v_1 are the concentration and speed of protons, n_{2i} and v_2 are the concentration and speed of molecular ions, ϕ is the electric potential ($\phi=0$ at the center of the discharge), n_p and n_e the fast and thermal electron populations, n_{o1} and n_{o2} are the densities of atomic and molecular hydrogen, σ_1 and σ_2 are the Ionization cross sections for atomic and molecular hydrogen by the fast electrons, and σ_{21} is the combined cross section for proton production by dissociative Ionization and excitation. ν_1 and ν_2 are the frequencies for collisions with neutral hydrogen of H^+ and H_2^+ respectively. M is the Ion mass and v_p is the fast electron speed. σ_{21} is the reaction rate for proton production from H ; by electron collision, calculated using a Maxwellian electron distribution. G_1 and G_2 are the creation rates of H^+ and H_2^+ by ionization of atoms and diatomic molecules, respectively. z is the axial distance along the discharge.

Using the normalization

$$\eta = -\frac{e\phi}{kT_e} ,$$

$$n_1 = \frac{n_{1i}}{n_{eo}} ;$$

$$n_2 = \frac{n_{2i}}{n_{eo}} ,$$

$$u_1 = v_1 / (2kT_e / M)^{1/2} ,$$

$$u_2 = v_2 / (kT_e / M)^{1/2} ,$$

and

$$s = \frac{n_p n_{o2} \sigma_2 v_p}{n_{eo} (kT_e / M)^{1/2}} z$$

$$v_2' = \frac{2^{1/2} v_1 n_{eo}}{G_2} ,$$

$$v_1' = \frac{2 v_2 n_{eo}}{G_2} ,$$

$$K_1 = \frac{n_{eo}^2 \langle \sigma_{21} v_e \rangle}{n_p n_{o2} \sigma_2 v_p} .$$

then the equations reduce to

$$2^{1/2} \frac{d}{ds} u_1 n_1 = \frac{n_{o1}}{n_{o2}} \frac{\sigma_1}{\sigma_2} + K_1 e^{-\eta} n_2$$

$$\frac{d}{ds} u_2 n_2 = 1 - K_1 e^{-\eta} n_2$$

$$\frac{d}{ds} n_1 u_1^2 = \frac{1}{2} n_1 \frac{d\eta}{ds} - v_1' u_1 n_1$$

$$\frac{d}{ds} n_2 u_2^2 = \frac{1}{2} n_2 \frac{d\eta}{ds} - v_2' u_2 n_2$$

K_1 represents the ratio between the production rate of H^+ by dissociation of the H_2^+ ion, and the creation rate of H_2^+ . The proton yield will be large if K_1 is large.

The Ion current densities at the walls (which determine the Ion currents that can be extracted) are given by

$$J_1 = e n_{e0} (2kT_e/M)^{1/2} n_1(s_s) u_1(s_s)$$

for the H^+ Ion current density and

$$J_2 = e n_{e0} (kT_e/M)^{1/2} n_2(s_s) u_2(s_s)$$

for the H_2^+ ion current density. Here $n_1(s_s)$, $v_1(s_s)$ are the normalized density and speed of H^+ at the sheath and $n_2(s_s)$, $v_2(s_s)$ the corresponding values of H_2^+

We are implementing the ion source model in COMSOL.

G. Ironless Cyclotrons

G.1 Background

Cyclotrons are used for high energy particle production. Cyclotron technology has been developed over many decades, and today it is considered a mature technology.

The present approach for making cyclotrons includes the use of magnetic iron poles and iron return yokes, to decrease the requirements of the electromagnets needed to generate the magnetic field. In addition, magnetic iron poles are used for shaping the field. It is well known that the radial and azimuthal field dependence is very relevant for particle acceleration and for particle stability. For synchrocyclotrons, the field needs to decrease with increasing radius, for particle stability. For isochronous cyclotrons, the average magnetic field needs to increase in order to balance the increase in mass with energy of the particle due to relativistic effects, and the field must vary azimuthally in order to provide beam stability.

The use of superconductivity in cyclotrons opens the potential for compact, high field devices. The use of iron is not as attractive in these applications, as most magnetic materials saturate at a field of about 2 T. In addition, the use of the iron results in heavy machines.

Stray field screening is also difficult in these machines, in particular in the high field machines, and in particular along the axis of the machine.

Yoke-free cyclotron concepts have been proposed in the past, for isochronous cyclotrons. [Martin N. Wilson, Martin F. Finlan, *CYCLOTRON WITH YOKELESS SUPERCONDUCTING MAGNET*, US patent 4943781] The field shaping for the isochronous cyclotron was achieved by a combination of coils at large radii and iron pole tips in the bore of the coils, limiting the flexibility of field shaping by coils that are above/below the beam chamber. The patent does not mention magnetic shielding requirements.

G.2 Iron-less or minimum-iron cyclotron concepts.

A. Magnetic shielding

The first application of the replacement of iron by coils is in magnetic shielding. Magnetic shielding is required in the case of cyclotrons used for proton radiotherapy for patient treatment. It is desired to produce magnetic fields that decrease rapidly away from the device to minimize stray field effects in the clinical environment. It is also desirable to decrease the magnetic field away from the cyclotron for other non-patient applications, in order to minimize access requirements or to enable location of cyclotrons in close proximity to magnet-sensitive equipment.

There are several options of decreasing the stray field with coils. The first one has a set of coils, with current flowing generally in the direction opposite to that of the main coils of the cyclotron, to reduce the dipole field and higher magnetic field moments produced by the main coils. In this case, it is possible to have the fields decay much faster than dipoles.

Figure G.1.a shows a schematic of the conventional approach [Antaya, Timothy, High-field superconducting synchrocyclotron US Patent 7541905; T. A Antaya, Radovinsky A.L, Schultz J.H., Titus P.H., Smith B.A, Bromberg L., *Magnet structure for particle acceleration*, U.S. Patent 7656258]. Coils 102 and 104, wound on structural elements (bobbins) 110 and 112, represent the main coils for the cyclotron, which produces magnetic field in the midplane 120 as well as stray fields away from the cyclotron that need to be shielded. The beam chamber is located at the midplane of the machine. The magnetic yokes or poles 130 and 132 are used to increase the magnetic field on the midplane of the device 120, to shape the field in this region, as well as to shield the magnetic field away from the machine. The use of iron is particularly effective at low fields, as the iron saturation results in more effective field increment, field shaping and magnetic field shielding than in higher magnetic fields needed for compact machines where the iron is driven over saturation.

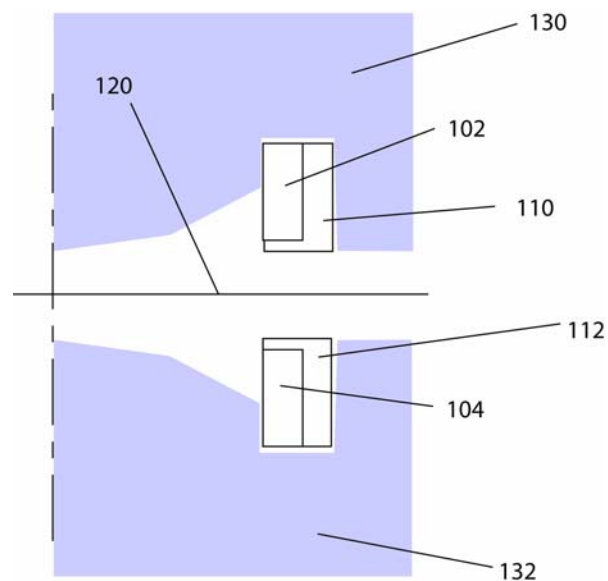


Figure G.1.a Conventional approach with iron for field shaping and shielding.

Figure G.1.b shows an illustrative design of the iron geometry. The bobine on which the coils is wound is not shown.

In the case of the iron, the field profile contour is substantial away from the device, and the field is particularly hard to shield along the axis of the cyclotron, as the

magnetic shielding material has some, but limited impact, on fields normal to be main chord of the iron shield. The 5 Gauss contour for a 250 MeV, 9 T central field cyclotron is shown in Figure G.2.

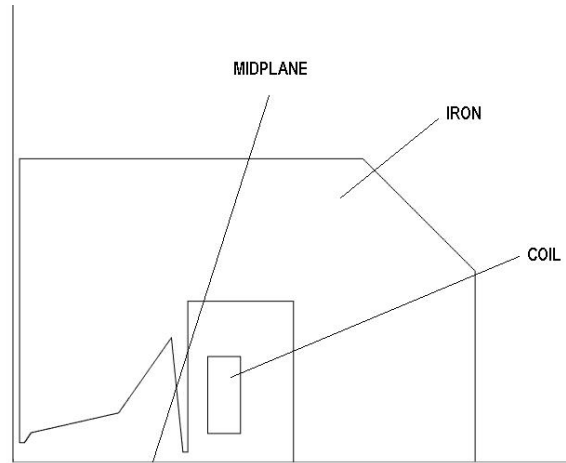


Figure G.1.b Diagram of K-250 cyclotron used for illustrative analysis and comparison; Model includes the “finger” for modification of the field allowing for beam extraction.

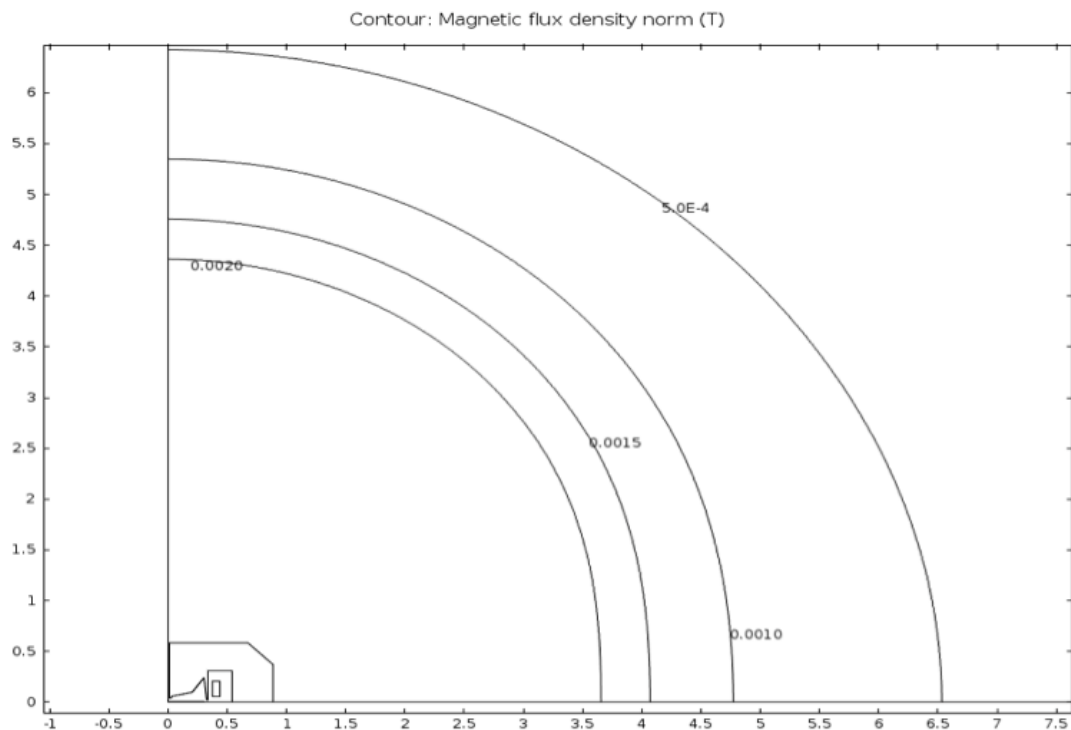


Figure G.2. Contour of 5, 10, 15 and 20 Gauss field for conventional synchrocyclotron with iron shielding (250 MeV, 9 T central field).

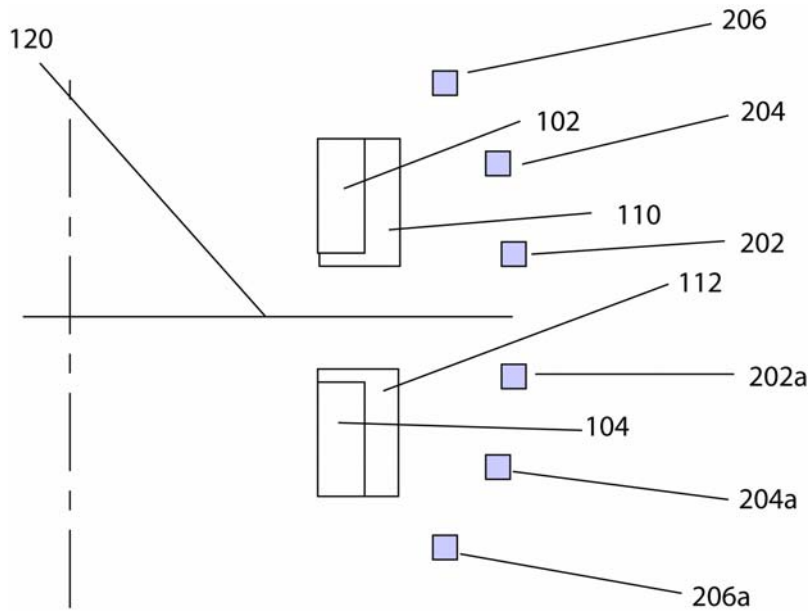


Figure G.3 Schematic diagram of a ironless cyclotron with one set/layer of coils for shielding the magnetic field from a cyclotron.

Figure G.3 shows the approach where the iron for shielding is replaced by a single set (layer) of coils. It is referred to as a single layer, as multiple layers will be explored further below. We have performed calculations to illustrate the potential of the approach of the single layer of coils. For illustrative purpose, the case of the single set of shielding coils is shown in Figure G.4, using the field profile requirements (on the midplane) as for that calculated in Figure G.2. In this case, all the iron has been removed. In Figures G.3 and G.4, there is only one set of main coils. The coil structural elements (bobbins) are non-magnetic, and are not included in the computational model. In this case, the net dipole moment of the main set of coils is approximately balanced by the net dipole moment of the shielding coils.

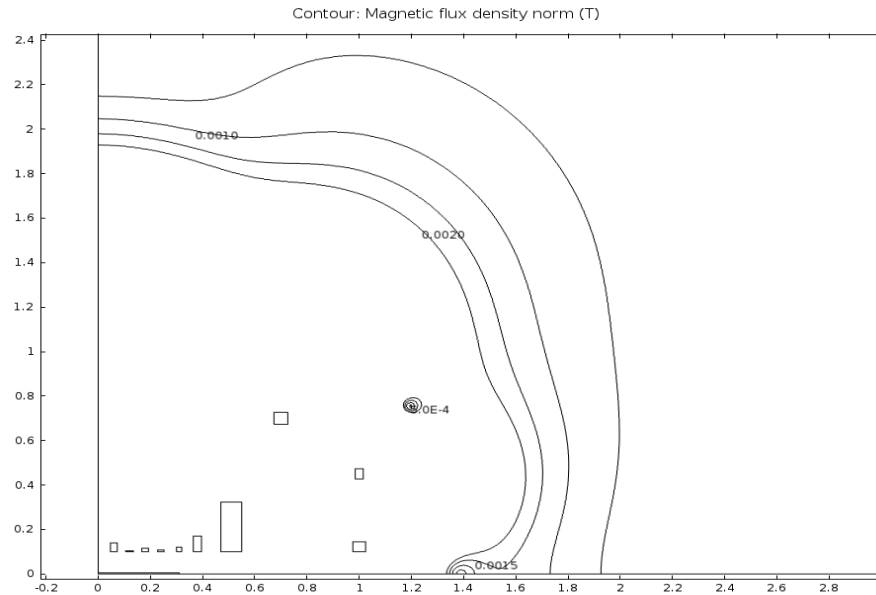


Figure G.4 Contour of 5-10-15-20 Gauss for the illustrative case of a single set of shielding coils, corresponding to the geometry of Figure G.3. Note that this case has a set of coils for shaping the field on the midplane, to be discussed later.

One of the main problem of the options shown in Figure G.3 and G.4 with a single set of shielding coils is that the set of shielding coils reduces the value of the magnetic field on the midplane of the cyclotron, the region of interest. In order to compensate for the reverse field due to the shielding coils, the main cyclotron coils need to be driven to higher currents (and associated fields). In the case when the cyclotron is designed such that the main fields are close to the maximum allowed by the field-current-temperature space (for a superconducting cyclotron), the reverse field from the shielding coils results in a substantial increase in difficulty in the design of the main coils.

One way to avoid this problem is to have two or more sets or “layers” of shielding coils, as illustrated in Figure G.5 (shown for 2 layers). In this case, the currents in the coils are chosen so that the net effect of the two sets of shielding coils on the midplane is small. In addition, the currents in the shielding coils are chosen so that the net dipole moment from the two sets of shielding coils balances the far-field magnetic field dipole moment from the main cyclotron coils. Although more coils are needed in this case, and with higher current, it is not necessary to increase the current/field of the main cyclotron coils, which are the most demanding coils.

In this case, the return flux of the cyclotron is guided into the region between set of coils 200's (202-204-206 and symmetrical coils 202a, 204a and 206a), and set of coils 300's (302-304-306 and symmetrical coils 302a-304a-306a). The current flowing in set of coils 200'a is in the same general direction as that in the main cyclotron coils, while the currents flowing in the set of coils 300's is in the general opposite direction as the main dipole coils.

Figure G.6a shows the magnetic field lines for the case of the two sets/layers of shielding coils, with shaping coils. Note that most of the flux from the beam chamber region is channelled through the two sets of shielding coils. Figure G.6b shows magnetic flux leakage for the case of two sets/layers of shielding coils.

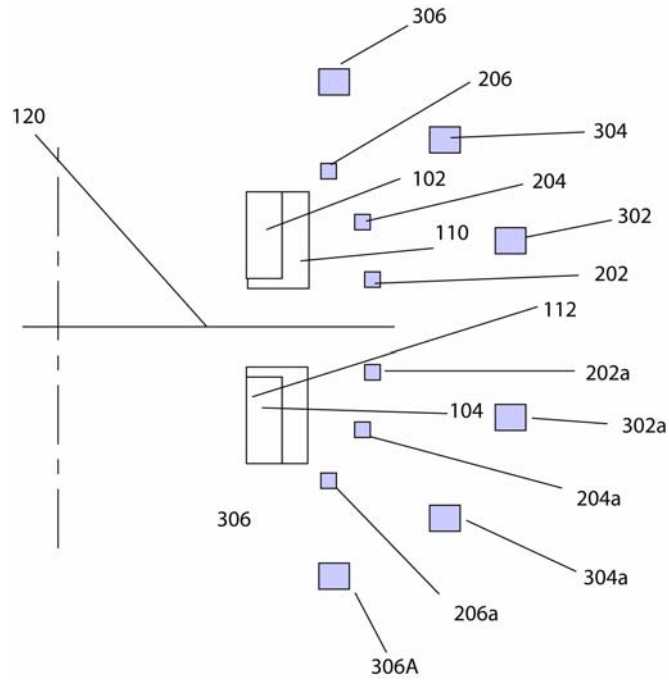


Figure G.5 Schematic diagram of an ironless cyclotron with two set of coils for shielding the magnetic field from a cyclotron.

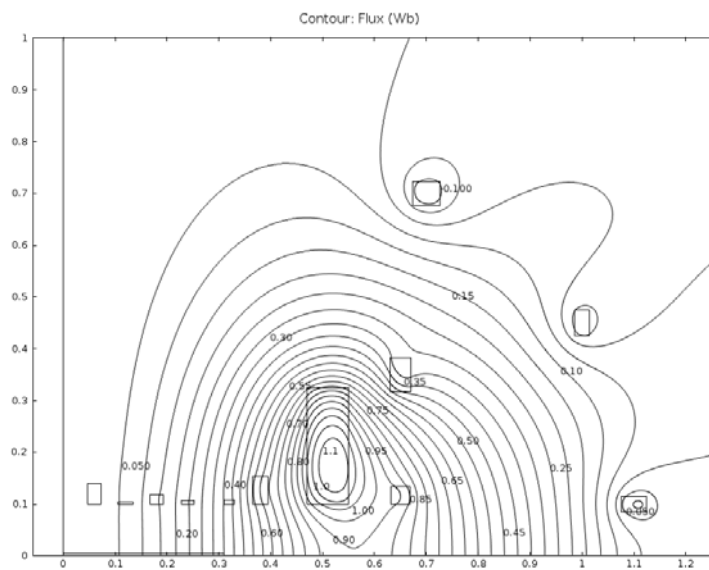


Figure G.6a Illustrative results of the case with two sets/layers of shielding coils, with shaping coils.

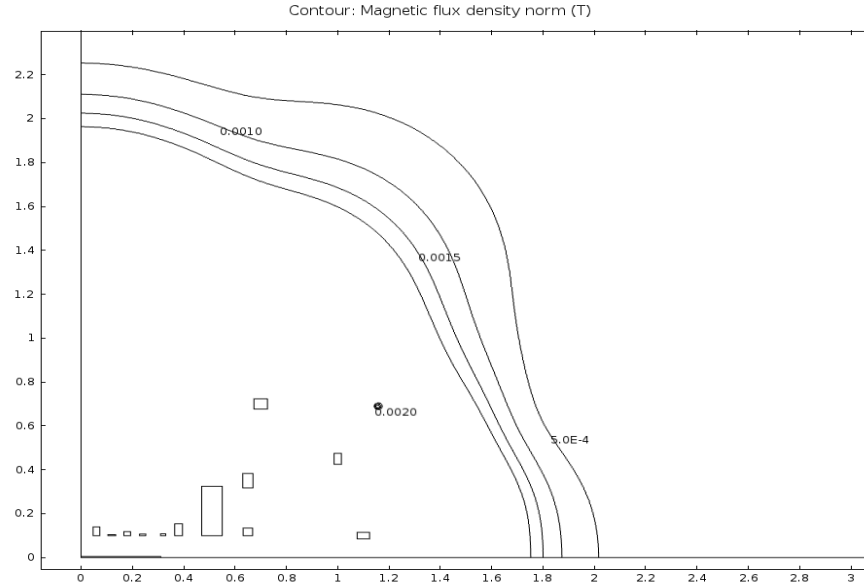


Figure G.6b 5, 10, 15 and 20 Gauss contour for illustrative case with two sets of coils for shielding the magnetic field from a cyclotron.

The not fully optimized cases show an increased peak field in the case of the single layer, of about 0.1 – 0.2T, compared to the field in the 2 layer case.

Although we mention only dipole moment cancellation, it is to be understood that with multiple coils, it is possible to balance not only the dipole moment, but also higher order moments, resulting in increased rate of decay of the field. For an n th-pole field, the field magnitude sufficiently away from the device decreases as $B \sim 1/r^{n+1}$, so cancelling higher order moments results in a faster rate of decay of magnetic field. In the case of symmetric sets of coils, n is even. If only the dipole is cancelled, the next largest magnetic field moment is the quadrupole moments, which decreases as $1/r^5$. This process is applicable when the coils are axisymmetric. If there are errors in the coil axis (that is, the axis of the coils is not aligned), or if the coils are not circles, there will be magnetic flux leakage that decays slower. However, in practice, the errors are small, and the magnetic flux leakage in the region of interest is dominated by non-cancelling moments.

It is possible to use this magnetic shielding technique for all cyclotrons, both isochronous cyclotrons and synchrocyclotrons, although the illustrative calculations were performed for a synchronous machine.

Although we have described mostly axisymmetric multipoles (*i.e.*, field components that are azimuthally symmetric), the technique is also useful for cancelling non-axisymmetric field components, as for example, those generated by the flutter required for isochronous machines. In this case, field by making the coils non-axisymmetric it is possible to cancel the flutter-like fields away from the machine by using either non-axisymmetric perturbations of the shielding coils described above

(by making either radial or axial “bumps” on the coils) or by placing separate coils. Loops from coils that do not include the axis of the machine can be used to cancel the non-axisymmetric magnetic field modes. The loops can be oriented with axis that are parallel to the main axis of the machine, or perpendicular to it. The loops are not necessarily circular. A method to determine the shape and current amplitude of the components is by expanding the field of the cyclotron in spherical harmonics away from the machine. Appropriate shaped and located loops can be used to cancel individual modes.

B. Establishment of magnetic field shaping in synchrocyclotrons.

The second application of the use of SC coils to remove the iron is for the field shaping. The use of multiple coils can be used to shape the field, in addition to preventing or minimizing the field in regions remote to the cyclotron.

In the case of synchrocyclotrons, the field needs to satisfy some requirements for orbit stability. The value of the magnetic field needs to decrease with increasing radius, while keeping the value of

$$2 v_z < 0.5 v_r$$

where

$$v_z = n^{1/2},$$

$$v_r = (1-n)^{1/2},$$

and

$$n = -d \log(B) / d \log(r)$$

over the accelerating region, and it needs to raise quickly with radius in the extraction region. [M.S. Livingston and .P. Blewett, *Particle Accelerators*, McGraw-Hill, 1962]. B is the magnetic flux density on the midplane and r is the radial location. At the extraction $2*v_z = v_r$ and $n=0.2$ (weak focusing fails for these conditions).

With this type of device, the transient frequency of a beam bunch is dependent on the radial magnitude of the axial magnetic field and the particle energy (due to relativistic effects). Thus, the frequency of the RF varies during the beam acceleration.

Particular radial profiles are required. It is the purpose of this section to demonstrate that adequate field shaping can be achieved with the use of electromagnetic coils instead of being shaped by iron or other ferromagnetic elements. A priori it is not clear that it is possible to achieve the adequate field profiles. In the Helmholtz pair (with an axial separation equal to the coil radii), the axial gradient of the magnetic field is 0 at the central midplane region. With coil

pairs with height between the coils larger than the radius, the field in the midplane decreases radially while increasing along the axis away from the midplane. Thus, it is expected that only with coil heights much larger than the radius it will be possible to generate radially decreasing magnetic fields. We have determined that the field can decrease radially outwards because of the effect of the field at radii larger than the coil radius. Here, the field generated by a set of coils is rapidly decreasing and even reversing sign, even when the coil height is smaller than the coil radii.

We have calculated the current in a set of coils above and below the midplane that provide a field profile similar to that of the K250 cyclotron. Limited optimization of the system was performed, and the calculations are meant to be illustrative. The process of optimization assumed a constant minimum height for the coils to allow clearance in the region for the beam chamber. The coil dimensions were adjusted so that the current density in all the shaping coils, as well as the main coil, was constant, as if the coils were connected in series and the same superconducting cable would be used in all coils. The coil location was adjusted radially in order to minimize the weight of the system. The shielding coils were also adjusted to minimize the weight of the system or to minimize the maximum magnetic field.

Figure G.7 illustrates the field profile of the K250 and that generated by the set of coils also shown in Figure G.4. The shaping coil currents in the design shown in Figure G.7 were not very large currents, or large opposing current. Indeed, it is surprising that relatively small currents are required in order to provide the field shaping.

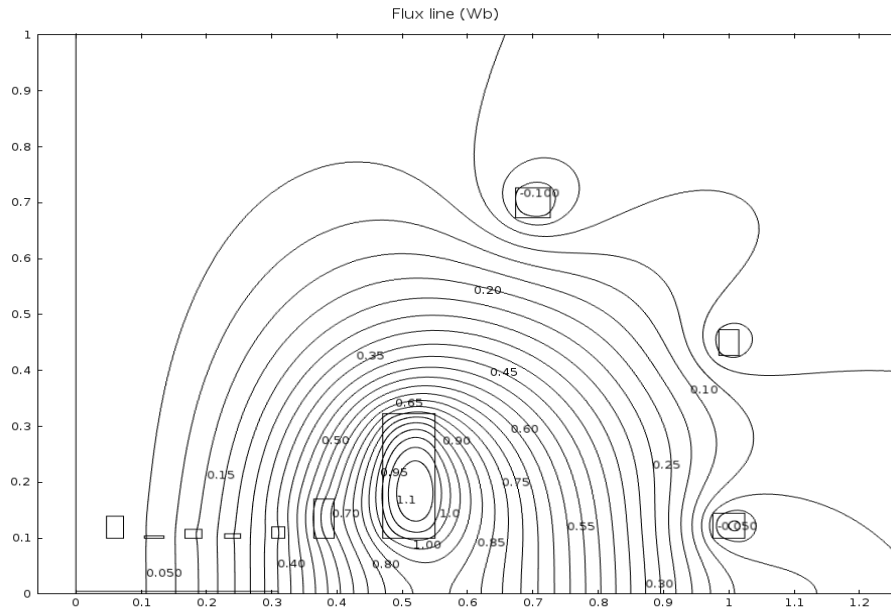


Figure G.7. Magnetic field lines for illustrative case duplicating the K250 field profile on the midplane, but done without iron, corresponding to the illustrative model shown in Figure G.4.

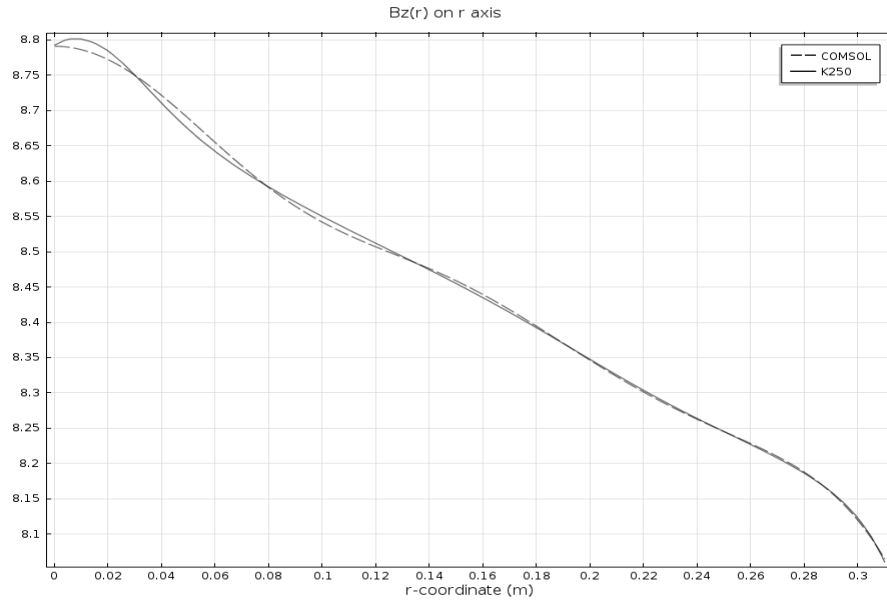


Figure G.8 Field magnitude on the midplane for the case of K250 and that of an iron-less cyclotron, for the case corresponding with Figures G.2 and G.7.

Figure G.8 shows the magnetic field profile on the midplane, for the cases of K250 (with iron) and for the case without iron, with shaping coils and one set/layer of shielding coils. One of the consequences of removing the iron is that it is possible to substantially open the region in the midplane. When iron is used for shaping the field, it is difficult to provide sufficient shaping in compact machines if the gap is large, due to the fact that compact machines run at high magnetic field that saturate the iron. In the case with minimal iron, the iron is only there for shaping, the fields being produced by superconducting coils.

The coil sets are up-down symmetric. They can be positioned with sufficient accuracy to minimize the field errors, and as a consequence they can be manufactured without the need of shimming, which substantially decreases the effort required in manufacturing the cyclotrons (since the shimming, due to inhomogeneous iron, is specific to a given machine).

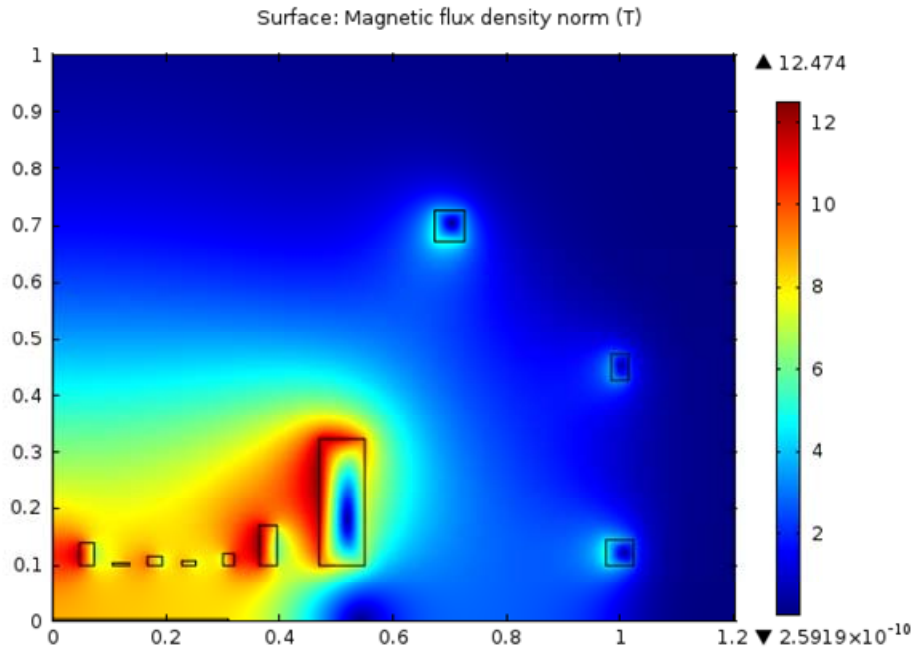


Figure G.9 Contours of magnetic field for the case of a single set of shielding coils and with shaping coils corresponding to the cases shown in Figure G.7 and G.8.

There is the possibility of leaving some iron near the beam chamber to achieve some of the shaping while leaving the shielding to the set of coils. Figure G.10 shows an illustrative model with iron and a single set/layer of shielding coils.

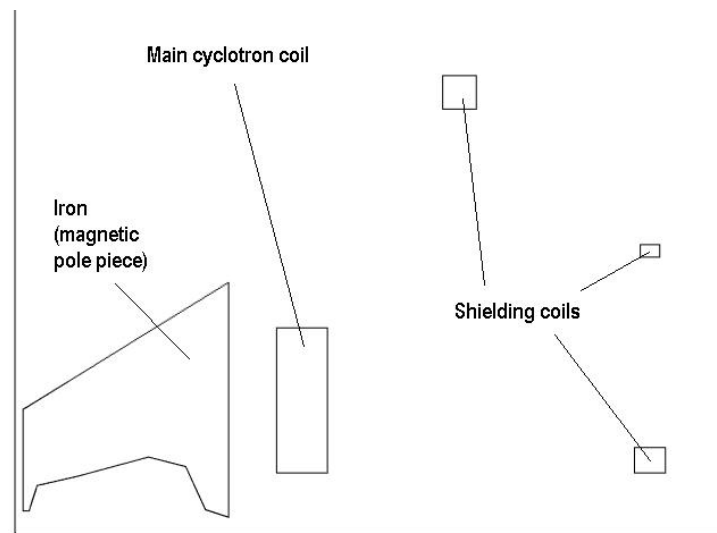


Figure G.10. Illustrative case with iron for shaping (for synchrocyclotron magnetic topology) and shielding coils.

We have investigated multiple cases of cyclotrons that use a single set of shielding coils, a set of shaping coils and the main cyclotron coils. We have also investigated

cyclotrons that use two or more sets/layers of shielding coils, a set of shaping coils, and the main cyclotron coils. And we have investigated the case when there is shaping by the iron, with one or more sets of shielding coils. A case with iron shaping and one set/layer of shielding coils is illustrated in Figure G.10. The shape of the iron is not optimized, and is only used for illustration. However, the magnetic field on the midplane is the same or nearly the same as in the case of the K250 (which uses only iron and no shielding coils, as shown in Figure G.1a). We have performed calculations for both single and multiple sets/layers of shielding coils, but in Figure G.10 only one set/layer of shielding coils is shown.

The magnetic field on the midplane for the case with iron shaping and coil shielding corresponding to Figure G.10 is shown in Figure G.11. Figure G.12 shows the magnetic field leakage away from the machine.

Note that the gap allowed in the midplane region is reduced in the case of the iron, with about 5 cm half-height gap, as compared to the illustrative case with the superconducting shaping coils shown in Figures G.4, G.6, G.7, G.8, G.9, which is 0.1 m for the half-height gap. As discussed above, even though the cases are illustrative, the reason for the larger gap in the case of coils is that there is need for a cryostat between the coils and the beam chamber. In the case with iron shaping, the iron is warm and the gaps required for placing a cryostat are not needed. Thus the iron can be closer to the beam chamber than the superconducting shaping coils. Besides, it permits a room temperature axial access to the midplane, which can simplify axial beam injection would it be given the preference.

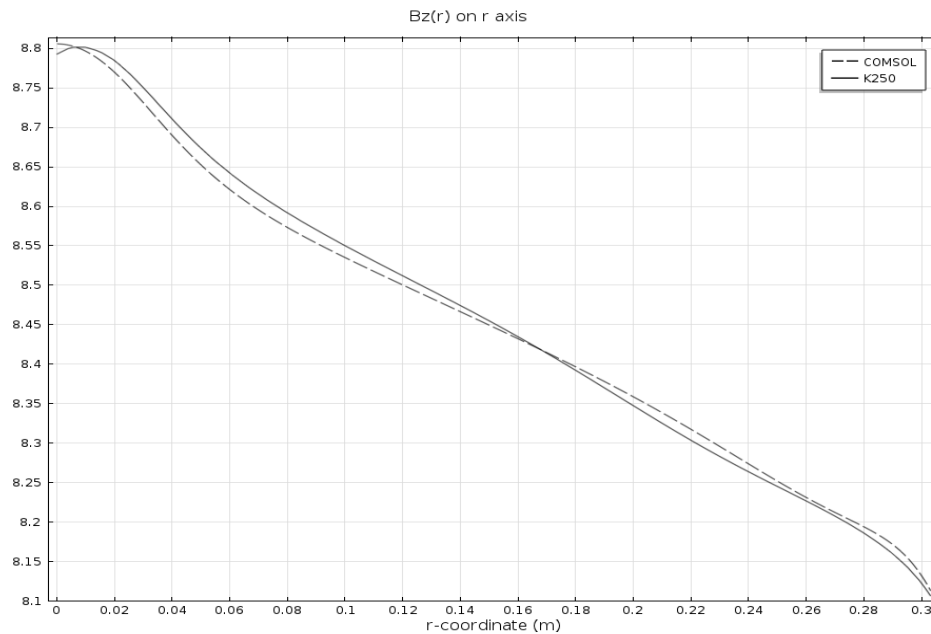


Figure G.11. Magnetic field on the midplane, as a function of radius, for the cases of K250 and for the case with iron shaping, coil shielding shown in Figure G.10.

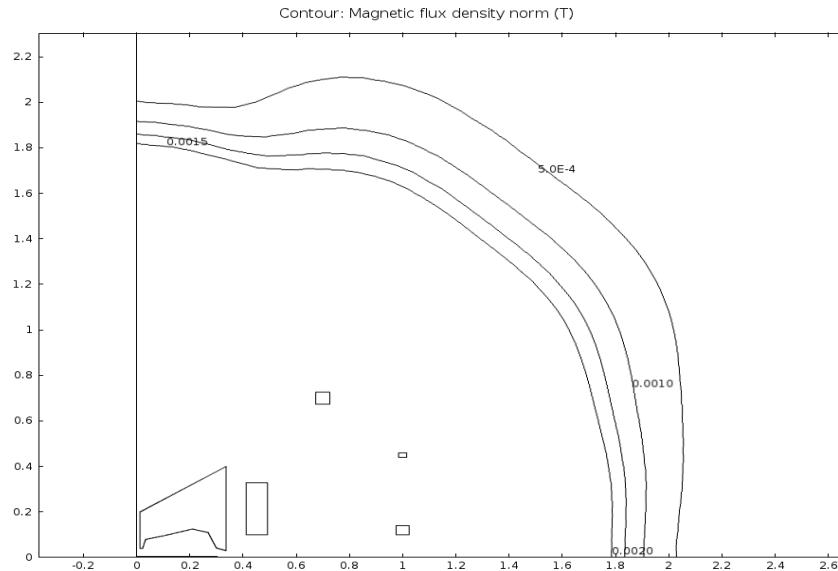


Figure G.12. Contours of 5, 10, 15, 20 Gauss for the case with iron for shaping, coils for shielding, corresponding to the case in Figures G.10 and G.11.

Note that the 5 Gauss region is slightly larger in the illustrative case of the iron shaping/coil shielding case (shown in Figure G.12) than in the case of coil shaping and single set of coil shielding, shown in Figure G.4.

In the cases of Figures I.8 and I.11, the beam stability requirements for the beam are satisfied for both the K250 and the iron shaping, coil shielding case.

Near optimized systems indicate that although the field is slightly higher in the main coil in the case of a single set of shielding coils, the difference is not much, less than about 5%. However, the use of a single set of shielding coils results in a lighter, simpler system.

Discussion

There are several requirements in the design of cyclotrons. They require a specific field in the beam chamber (in the midplane region) for adequate acceleration, while at the same time the magnetic flux leakage away from the machine should be low. The magnitude of the magnetic flux leakage has implication on exclusion zones, for either patients, personnel or the location of equipment that is sensitive to magnetic field.

There are several options for achieving these objectives. Shaping of magnetic field profile in the beam chamber region can be achieved by either iron or by the location of shaping coils. The magnetic field profile in the case of synchrocyclotrons can be provided by a set of coils that is on top and below the beam chamber, as shown by our calculations above. For the case of isochronous cyclotrons, as shown by Wilson *et al*, the coils can be away from the beam chamber.

Shielding to minimize leakage of magnetic flux can be achieved by either using iron, or by using shielding coils. We have described above the use of a single set/layer of shielding coils, and using more than one set/layer. There are advantages and disadvantages, but the use of shielding coils dramatically decreases the weight of the machine.

We have also looked at the implications of using a magnetic cryostat. We have concluded that the impact on the shielding of using a magnetic cryostat (*i.e.*, iron) is small.

In the case of the shielding coils, the size of the cryostat increases substantially. In the case of the shielding coils, the cryostat needs to surround both the main coil and the shielding coils. In the case of the use of shaping coils too, the cryostat also needs to enclose the shaping coils. Although the cryostat could be from magnetic material (*i.e.*, iron), for weight minimization a better approach would be to use an aluminum cryostat. Although there are some concerns with aluminum cryostats, they could be addressed by using an aluminum cryostat with a cladding. The cladding could be from iron or stainless steel. The impact of the iron on the shielding is minimal.

The choice of shaping/shielding depends on what is being optimized and other concerns. The issues are described below.

G.3 Enabling features by ironless and iron-minimized cyclotrons

The removal of the shielding iron allows for very large decrease in weight of the machines, as the weight of the coils and cryostat is a small fraction of the weight of the shielding iron that it replaces. A partially optimized set of parameters is shown in Table G.1. For reference, the weight of the K-250 magnet [Antaya] is about 20 tons

Table G.1.
Weigh of magnetic elements (coils, iron and cryostat) for different designs for a K250-compatible synchrocyclotron (tons)

	Two sets of Shielding coils	Single set of shielding coils
Shaping Coils	3.2	2.9
Shaping Iron		2.5

We have included the weight of the cryostat, as in the case of shielding coils, the outer cryostat weight increases substantially in order to accommodate the shielding coils.

Removal of the iron and replacement with coils that are located approximately at the same location as the edge of the iron (so that the system volume itself is not larger), eases installation of the device in systems that require movement or rotation of the cyclotron. It is much easier to place the device in a gantry that rotates, as taught by Gall [K. Gall, *CHARGED PARTICLE RADIATION THERAPY*, US patent application 2010/0230617, published Sep 16, 2010] and Timmer [J. H. Timmer, H. Goebel, S. Schmidt, Overath, J. Heese and M. Schillo, *IRRADIATION DEVICE*, US patent 8,053,746, issued Nov 8, 2011].

Indeed, the weight of the device is small enough that it may be possible to place the cyclotron on a robotic articulated arm, not on a rotating gantry, increasing the flexibility of placement of the device around a patient or around an object that is being interrogated or irradiated. Custom gantries, required for conventionally shielded cyclotrons for use with patients, are expensive and require heavy counterweights. The light-weight units could be used in a portable arrangement, a proton radiography treatment room on a mobile platform, such as a truck. Modular arrangements can be manufactured and tuned in the shop and shipped for the final installation at the stationary location in the hospital.

In these cases, the weight needs to be minimized. Current leads can be eliminated, using either persistent or near persistent units with removable current leads, or by inductively charged units. In this case of inductively charged units, the charging magnetic field needs to be substantial. Inductive charging has been used at MIT in

the Levitated Dipole Experiment (LDX), using a superconducting charging coil. [A. Zhukovsky, J. Schultz, B. Smith, et al., *CHARGING MAGNET FOR THE FLOATING COIL OF LDX*, in *IEEE Transactions on Superconductivity*, **11** 1873 (2001)]

Alternatively, current leads can be used. The current leads can be either low temperature or high temperature superconductors, or MgB_2 , in a cryostat that connects the fixed current leads, remote to the cyclotron, and the cyclotron. The losses in the superconducting interconnect are small, dominated by radiation losses. By using HTS, the refrigeration requirements to remove the thermal load are minimized. The heat load due to the resistive elements between the room temperature contacts and the superconductors is removed from the cryogenic environment remotely to the cyclotron, in a fixed location. In addition, they can be used in airborne platforms. The latter is important for interrogating objects from airborne platforms. [Hynes, Michael V. (Cambridge, MA, US) Harris, Bernard, Blackburn, Brandon, McElroy, John E., Lanza, Richard C., Antaya, Timothy A., Sheffield, Richard, Mihalczo, John T., Hausladen, Paul A., Hunt, Alan W., Andrews, Hugh R., Johnson, James, *Interrogating hidden contents of a container*, US Patent 7,970,103]

For some applications, it is still necessary to provide continuous cryogenic cooling to the unit, for long term operation of the device. In this case, the use of interconnects does not increase the design complexity, avoiding the need of inductively charging of the cyclotron.

Due to losses of the high energy beam, neutron and gamma radiation is generated that may have to be shielded. Since most material surrounding the cyclotron has been removed, it is possible to use better, lighter shielding materials than iron, close to the device, for improved radiation shield performance. Radiation shielding may be useful for applications with long term exposure (such as for operators of the device) or for devices with high beam currents (and thus high power). For gammas, high-Z materials are desired. For neutrons, light materials, with substantial concentration of hydrogen atoms, would be desired. Water, hydrocarbons, plastics and other light materials, mixed with a neutron absorber, such as boron, can be used, with better radiation shielding properties than iron. In radiation treatment rooms radiation shields can be installed around the cyclotron on the gantry or on the stationary wall separating the gantry from the patient space. However, there are advantages in terms of materials if the radiation source is shielded near the source.

Some of the coils, and in particular the shielding coils, can be made from different superconductors. For the case in Figure I.7, the peak field in the shielding coils is less than 6 T. By comparison, the shaping coils, including the main cyclotron coil, has fields on the order of 9-12 T for the illustrative example in Figure I.7. Thus, the shaping and main cyclotron coils could be made from high performance superconductors, such as Nb_3Sn , high temperature superconductors or MgB_2 . However, the shielding coils can be made from the inexpensive NbTi superconductor.

In the case of shielding coils, the support between the magnets can be cryogenic, to avoid carrying large loads through the cryogenic environment (requiring low thermal conductivity straps). The magnetic loads need to be transferred through the cryogenic environment, but these loads are substantially smaller than the ones due to the magnetic loads between warm iron and cold superconducting coil, as in the case of the K250. Besides, the absence of the room temperature iron removes the requirement that the elastic stiffness of the cold-to-warm supports shall offset magnetic instability due to the interaction between the coils and the iron. In the case of shielding coils, the straps can be made from metals (steel).

There is a large number of coils in the case of a cyclotron with shielding coils and/or shaping coils. There are two potential methods of powering the coils. They can be driven electrically in series, with a single set of current leads. This mode would provide the lowest cryogenic heat load, dominated by the current leads. However, by using multiple sets of leads there can be increased flexibility in adjusting the currents in the different coils. Different circuits would be useful in the process of optimizing the performance of the machine. However, once the machine has been optimized, it is possible to build further units with a single circuit. Trimming coils, at either room temperature or at cryogenic temperature inside the cryostat, could be used to slightly modify the field in mature-design machines, if needed.

The current in the cyclotron coils can be high, to provide protection through external energy dumping. Alternatively, small current could be used, requiring internal energy dump for protection. There are several ways of providing internal quench. Internal heaters in the coils can be energized to initiate a large normal zone in the coils. Alternatively, AC heating can be used, as suggested by inductive quench for magnet protection [Inductive quench for magnet protection, Schultz, Joel Henry, Myatt, Leonard, Bromberg, Leslie, Minervini, Joseph V. and Antaya, Timothy, United States Patent 7701677] It is possible to use AC quench by placing quench-inducing coils that have zero mutual inductance with the superconducting coil set. Because there are multiple coils, providing coils that have zero mutual inductance can be achieved with a wide range of coil or coils locations. By energizing the quench inducing coils with an AC current, it is possible to minimize the reactive power required (without any effect on the main coil currents), while at the same time generating AC fields in the superconducting coils. The heating from the AC fields drive the superconducting coils normal, thus resulting in internal energy dump. Different coil or coil sets can have different quenching mechanisms, with some coils having external energy dump, and the other coils having internal energy dump.

The use of internal energy dump for protection, either by using eddy current quench or by imbedded heaters, allows for low current operation. Low current is attractive in that the cryogenic losses are dominated by the current leads, and these cryogenic losses are reduced by low current operation.

The iron-free (or iron-reduced) concepts are particularly attractive for high field, compact cyclotrons, since the iron would otherwise be saturated in these devices. However, the concept also can be useful for low field machines, for decreasing the weight, if not size of the machine.

Because of the improved beam chamber access and support due to the use of the iron-free or iron reduced concepts, it is possible to easily exchange the beam chamber, or change the internals of the cyclotron, including placing/modifying internal targets, modifying the beam accelerating structure, changing the beam detectors.

The cyclotron superconducting coils (either shaping or shielding coils) can be cooled by conduction cooling to plates that are cooled by flowing helium. Supercritical helium can be used, because it is attractive to use single phase fluid in cyclotrons that change orientation with respect to gravity.

The present application provides significant advantages compared with the present state of the art. In addition to those mentioned above, the large gap around the mid plane that is facilitated by the use of shielding coils allows for easy access to this area through windows between posts connecting upper and lower halves of the cryostat, allowing for easy radial maintenance of the chamber, the ion source, the accelerating structures. In particular, beam chambers can be made replaceable and modular, for different extraction radii and beam energies.

H. Phase-locked loop in

H.1 Background

It is well known that the frequency of the RF in synchrocyclotrons needs to be adjusted as the beam is being accelerated. The cyclotron frequency varies with radius, as the field varies, and also as the mass of the accelerated particles varies due to relativistic effects.

There is literature on the control of the frequency of the RF acceleration. The object of the prior art is to adjust the frequency to match the cyclotron frequency of the beam, while monitoring the beam after extraction [A. Sliski, K. Gall, *Programmable Radio Frequency Waveform Generator for a Synchrocyclotron*, US patent 7828347], or to match a resonant circuit and the RF that it generates to the required frequency. But there is no effort to either monitor the phase of the beam during acceleration, or to match the phase of the RF and the beam during acceleration. If the relative phase drift between the beam and the RF results in substantial phase difference, the RF does not increase the beam energy, but instead decreases the energy of beam by extracting energy from it. The beam continues to lose energy until it has drifted enough in frequency/phase: as the particles are decelerating, they are moving into regions of increasing magnetic field that require increased frequency for synchronism, but the applied RF field is decreasing in frequency, so the particles eventually slow down enough to the point where they are again in phase with the RF field and start accelerating. Although eventually they get accelerated, the beam quality suffers and the average beam current decreases. It would be best if the phase of the RF and the phase of the beam are kept in sync for optimal acceleration.

H.2 Optimized system for accelerating beams in synchrocyclotrons.

In order to best accelerate the particles, it is desired to establish relate the phase of the RF to that of the beam. The phase of the RF, although fixed at the source, varies across the gap, due to the finite velocity of propagation of the electromagnetic waves. At each radial location, the phase of the RF can be identified as $\Delta\phi_{RF}$. It is understood that the phase is a function of the radius of the beam. $\Delta\phi_{RF}$ is the phase shift of the RF, at any given time, from that of the source. It should be noted that $\Delta\phi_{RF}$ is a function of the radial location of the beam (that is, the energy of the beam), depending on how the RF is feed to the accelerating dee's.

In order to be able to best accelerate the beam, it is necessary to monitor the real-time phase of the beam. It is assumed that the beam passes through the detector at times $t_{beam} + \Sigma (2 \pi / \omega_n)$, where ω_n is the cyclotron frequency at the radial location of the beam (at the n^{th} turn). As in the case of the RF, there is a phase lag between when the beam excites the monitoring device (the "detector"), and the point of detection of the phase (the "sensor"). It should be understood that there can be more than one detector element, which when combined are identified as "detector."

In addition, the azimuthal location of the beam monitoring device is removed from that of the RF. The delay from the detector to the sensor is defined as t_{sensor} . It is assumed that the phase of the RF wave, at the source, at the time when the beams is sensed by the system is ϕ_{source} . Thus, the electric field at the RF source when the beam is sensed by the system is

$$E_{\text{source}} = \exp[i \omega (t_{\text{beam}} + \sum (2 \pi / \omega_n) + t_{\text{sensor}}) + i \phi_{\text{source}}]$$

In particular, it may be desirable to measure the beam phase in an azimuthal location that is under the ground electrode, in order to minimize the noise due to the RF.

After the beam crosses the detector, there is a delay until the beam reaches the accelerating gap, referred to as $t_{\text{beam-gap}}$. The RF field in the gap, when the beam crosses the gap, is then

$$E_{\text{gap beam crossing}} = \exp[i \omega (t_{\text{beam}} + \sum (2 \pi / \omega_n) + t_{\text{beam-gap}}) + i \phi_{\text{source}} - i \Delta\phi_{\text{RF}}]$$

The negative sign in the RF is due to the fact that the RF at the gap lags the RF at the source, by $\Delta\phi_{\text{RF}}$.

In order to maximize the acceleration, the phase of the RF, at the source, needs to be adjusted in order to provide maximum acceleration. It is known that relatively narrow range of phase result in best acceleration of the beam, with good phase stability. In particular, the beam should cross the accelerating gap while the electric field in the gap is increasing. In this manner, the particles that are lagging the bulk of the beam will be accelerated stronger than the bulk, and they will catch up to the bulk. Similarly those ahead of the bulk will experience lower electric fields, and thus they will be accelerated less than the bulk and slow down until the bulk catches up with them. We refer to the optimal phase of the electric field in the gap for acceleration of the beam, as ϕ_{optimal} .

Thus, it is desired that the phase of the RF, when the beam reaches the gap, is

$$\omega (t_{\text{beam}} + \sum (2 \pi / \omega_n) + t_{\text{beam-gap}}) + \phi_{\text{source}} - \Delta\phi_{\text{RF}} = \phi_{\text{optimal}}$$

Thus, ϕ_{source} can be obtained as :

$$\phi_{\text{source}} = \phi_{\text{optimal}} + \Delta\phi_{\text{RF}} - \omega (t_{\text{beam}} + \sum (2 \pi / \omega_n) + t_{\text{beam-gap}})$$

Then, the phase of the RF at the source, at the time that the beam is sensed by the system, should be

$$\phi_{\text{sensor}} + \phi_{\text{optimal}} + \Delta\phi_{\text{RF}} - \phi_{\text{beam-gap}}$$

where $\phi_{\text{sensor}} = \omega t_{\text{sensor}}$ is the phase lag between when the beam is sensed by the system and when the beam crosses the detector, and $\phi_{\text{beam-gap}} = \omega t_{\text{beam-gap}}$ is the phase lag required for the beam to reach the accelerating gap after it passes the detector. $\phi_{\text{beam-gap}}$ is just the angle between the location of the detector and the location of the gap.

It is to be understood that the above algorithm is illustrative, and there could be others used to control the phase. In general, the phase at the source that optimizes the beam acceleration is

$$\phi_{\text{source}} = f(\phi_{\text{sensor}}, \phi_{\text{beam-gap}}, \phi_{\text{Beam}}, \phi_{\text{RF}}, \phi_{\text{optimal}})$$

The control system of the RF uses a feedback system in order to control the phase at the gap, keeping it near optimum at all times during the acceleration process.

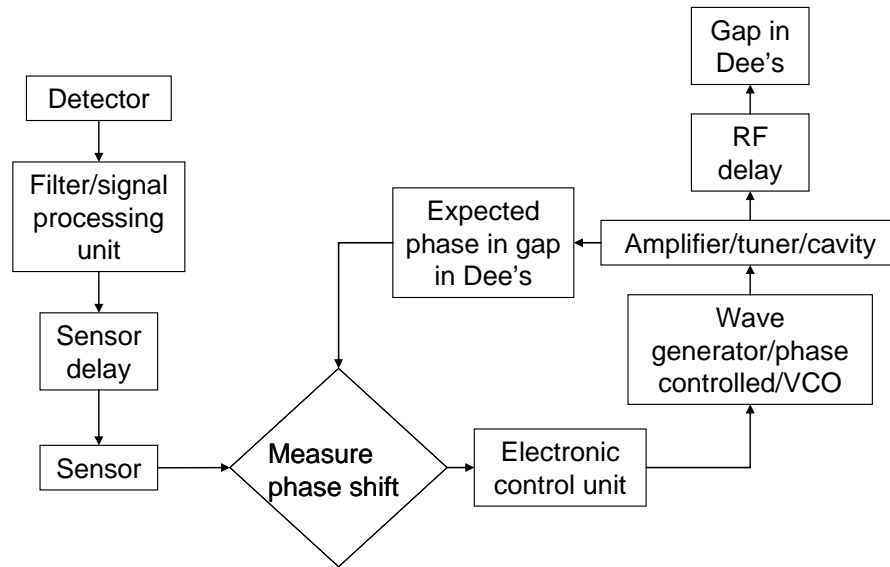


Figure H.1. Schematic of phase-loop control of beam in synchrocyclotron accelerators for optimal beam acceleration.

Figure H.1 illustrates the control system. The detector, which will be described later, is excited by the beam as it passes by. A filter or series of filters process the signal, which has a built-in delay, due to the final speed of propagation of the signal. The signal processing unit could also be an amplifier, or a differential amplifier, or it could combine the signal from multiple detectors. Multiple detectors could be used in order to reduce RF interference, decreasing or eliminating the signal in the detector due to the RF fields, and detecting the beam phasing with increased signal to noise ratio. The signal is sensed by the sensor, which could use advanced signal processing methods, including lock-in-amplification to determine the timing/phasing of the beam and determining the phase with respect to a reference signal, not shown in the figure. The reference signal could be a different signal, but

in this application it may be useful to use the amplified signal as the reference. The electronic control unit senses the shift between the expected signal at the Dee's with that measured by the sensor, and adjusts the wave generator/phase controlled or a VCO (Voltage-Controlled-Oscillator) so that the desired signal will be generated at the gap in the Dee's at the time when the beam is expected to pass through the Dee's.

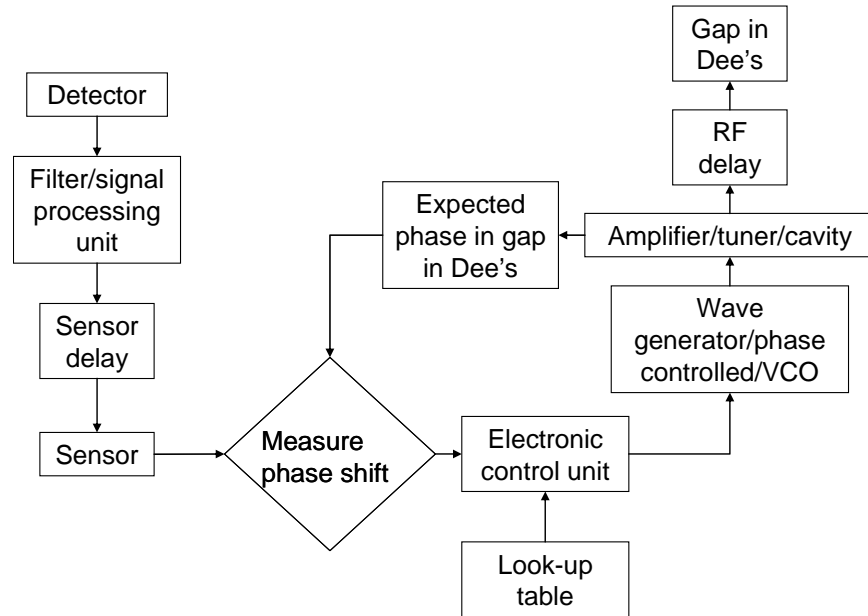


Figure H.2. Schematic showing the presence of a look-up table to provide additional information to the control system.

It is not necessary to monitor the phase every cycle, and an averaging can be used to determine the appropriate phase of the wave, in order to adjust for noise in the system. In addition, a look-up table of required phase/frequencies as a function of the beam energy is used in addition to the feedback. It is used both to assure that the beam is being sensed properly, as well as to provide information when either the signal from the beam is small, or the phase measurement unit is resetting, or during times when the beam phase is difficult to determine, such as immediately following injection of the beam into the accelerating region. Figure H.2 shows the presence of the look-up table for providing the missing information and to assure proper performance of the control unit.

As mentioned above, some of the delays are a function of the beam energy, as the radial location of the beam with respect to both the sensor and the accelerating Dee's changes with beam energy. The look-up table can store the values of the delays, which can be either measured or calculated. In addition, it is possible to vary the optimal phase of the beam with energy, as the stability criteria of the beam changes with energy. Thus, at lower energy it may be desired to adjust the phase for improved bunching of the beam, while at higher energies, once the beams are relatively well bunched, the phase can be adjusted for increased acceleration voltage

per pass in the Dee's. It is possible to determine the beam energy at a given revolution from the frequency of RF, and thus the approximate radius of the electron beam.

In addition to monitoring the beam phase and the average increase in energy, it would be possible to measure the beam "health" (beam pulse height, beam pulse width and beam pulse tail). A narrow beam pulse, with no tail (indicating particles that have fallen off-sync). As the particles lose sync with the RF, they spread in angle, changing the characteristics of the signal measured by the probe (less height, more width of the signal). Further analysis of the relationship between the beam acceleration rate and the beam "health" could avoid the need to adjust for the change in the phase delays of the different elements. The purpose would be to maximize the beam acceleration stably, by monitoring the energy increase per revolution or per a number of revolutions, and then adjust the phase to get maximum stable acceleration with good beam "health." The phase of the RF can be adjusted using the characteristic of the beam (height, width), coupled with the measured rate of increase of energy. This approach could be used instead of using a loop-up table for control of the RF, during at least a portion of the accelerating phase of the beam.

Figure H.3 shows an RF control diagram that illustrates the control. Even though there are still sensor and RF delays, by monitoring the beam parameters and the rate of energy increase it is possible to avoid knowing how the sensor and RF delay vary with energy. The phase is "dithered" slowly around a baseline phase and the impact on the beam acceleration monitored. The baseline phase is reset often during the acceleration process. There can be a look-up table to aid in the acceleration process. The control system can also include a adaptive system that learns, in such a way that some parameters in the look-up table are adjusted actively.

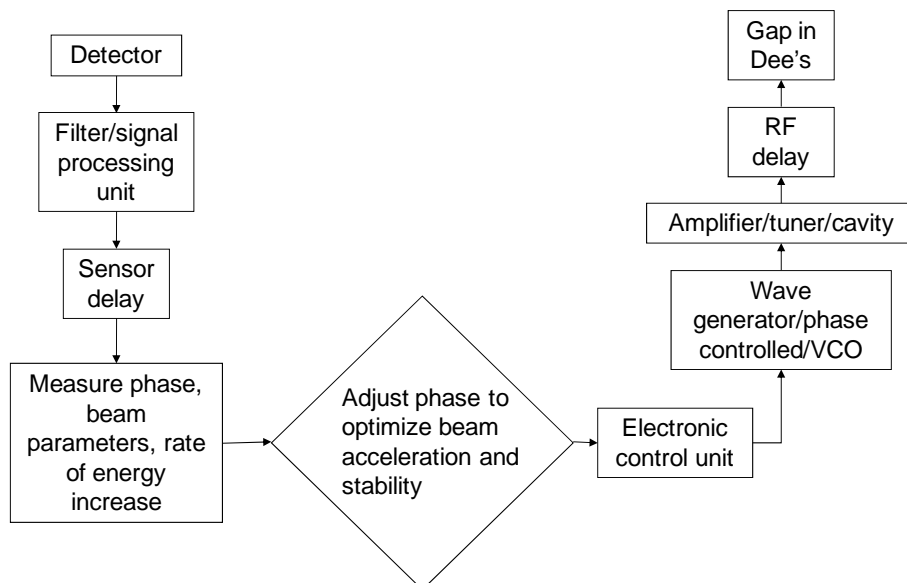


Figure H.3. Schematic showing a monitoring system that determines the beam parameters, including phase and shape. Control system varies (dithers) the phase around a baseline phase to determine the optimal phase, and resets the baseline phase periodically during the acceleration. Because of the large number of turns during the acceleration, the optimal phase does not change significantly from cycle to cycle.

The electronic control unit can either generate the signal with the proper phase, or alternatively it can adjust the parameters of conventional power supplies. For example, if the phase is lagging, it could temporarily increase the frequency of the signal in order to “catch” the phase. Similarly, if it is too advanced, it could reduce temporarily the frequency in order to slow down to the required phase. It should be noted that it is not necessary to provide feedback on the frequency of the signal, as control on the phase is sufficient, and an increase in frequency is similar to an increased in the rate of change of phase. A linear change in frequency can be provided by a quadratic change in phase, at otherwise constant frequency. That is,

$$\exp[i(\omega_0 + \Delta\omega t) t + i \phi_0] = \exp[i \omega_0 t + i (\phi_0 + \Delta\omega t^2)]$$

In principle, it may be possible to adjust the software so that the sensing loop, once the algorithm is determined, the continuous feedback monitoring of the beam is not needed. It is also possible that once done for one machine, it is possible to use the same algorithm in other machines. This approach is particularly of interest in machine that do not require iron for shaping, as it is expected that the field profiles can be reproduced very accurately between machines.

It is also possible to reset the frequency/phase of the equation, in order to prevent very large square times (phase shift scales as time-squared). The look-up table can be useful in this process.

H.3 Beam sensors

It is necessary to determine where the beam is with respect to the RF field. The beam sensor is key to the implementation of this approach.

There are several sensors possible. It is possible to have one or more loops. When the beam goes over one loop, it induces an emf in the loop and delayed into the sensor. It is possible to use one or more loops. The loops can be of either planar shape, or they can be convoluted loops, as in the case of the use of Rogowski coils. A single loop or multiple loops or coils can be used. It would be desirable to place the loop in a region where the electric field induced by the Dee's, during the time of detection, is small, in order to minimize noise. There are region both downstream and upstream of the gap where the field is 0 during the time that the beam is transiting the cyclotron, and the loops can be placed there. Depending on the

definition of ϕ_{optimal} , the detection would occur near $\pi/2 + \phi_{\text{optimal}}$ or $\pi/2 - \phi_{\text{optimal}}$ away from the gap.

Another potential way to decrease noise is to use two loops, placed in such a manner that they are symmetric (and reversed) with respect to the accelerating gap. In this manner, the emf due to the accelerating voltage can be eliminated. In addition, there will be two beam pulses in the sensor per cycle, potentially improving the detection of the phase of the beam.

Another potential location of the loops is rotated in relation to the accelerating gap. There are two angular locations along the beam orbit where the field in the Dee's is going through reversal at the time that the beam is going through them. In these two places, the rate of change of field is small, and although the fields are high, the rate of change of field are small. Sensitivity of the detector is improved when the loop is located in one of these two locations.

Figure H.4 shows the potential locations of the loop or loops.

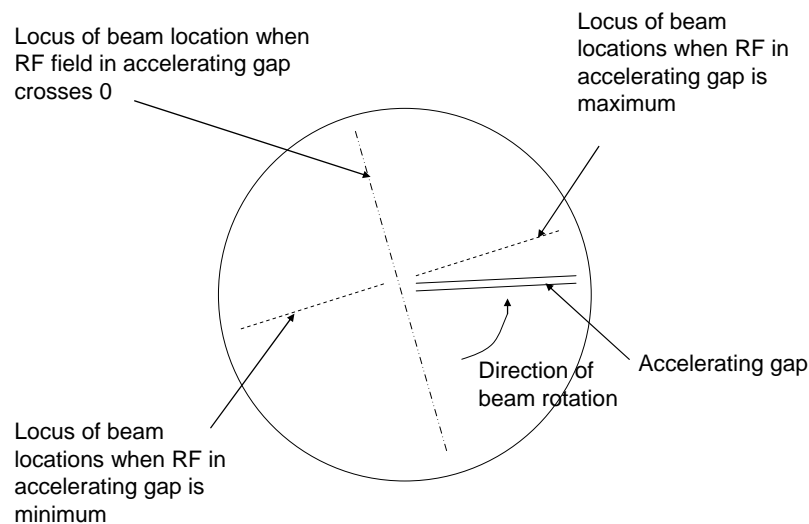


Figure H.4. Locations for the beam with respect to the location of the accelerating gap at different phases of the accelerating RF.

Figure H.4 shows a schematic of the acceleration region of a cyclotron. The location of the accelerating gap is indicated. It is well known that the peak accelerating field in the gap is reached after the beam has passed, for improved beam pulse. The locus of the location of the beam at the time when the accelerating field in the gap is highest is shown. Also shown is the locus of the beam when the decelerating field in the gap is the minimum. The beam is at these loci during the time when the rate of change of field is minimum

Also shown in Figure H.4 are the loci of the beam location when the electric field is 0. It is advantageous to place the sensor at these loci. However, in this case, the rate of change of the electric field is maximum, and if there is RF pick-up, it could generate substantial noise in the detection system.

Figure H.5 shows a detector loop at one of the loci of the beam location when the electric field has the minimum rate of change, which occurs, of course, at both times when the electric field is maximum and minimum.

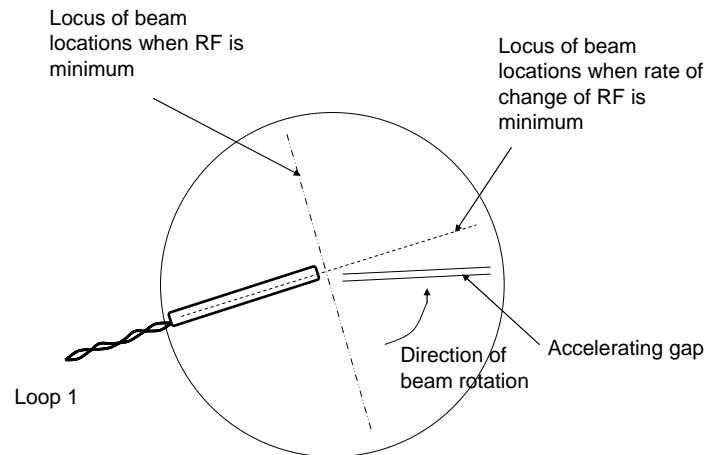


Figure H.5 Potential location of the sensor, in this case a loop sensor is illustrated. At this location the rate of change of the RF is minimum when the beam passes by the sensor.

Figure H.6 shows a detection loop at on of the loci of the beam when the amplitude of the electric field is minimum.

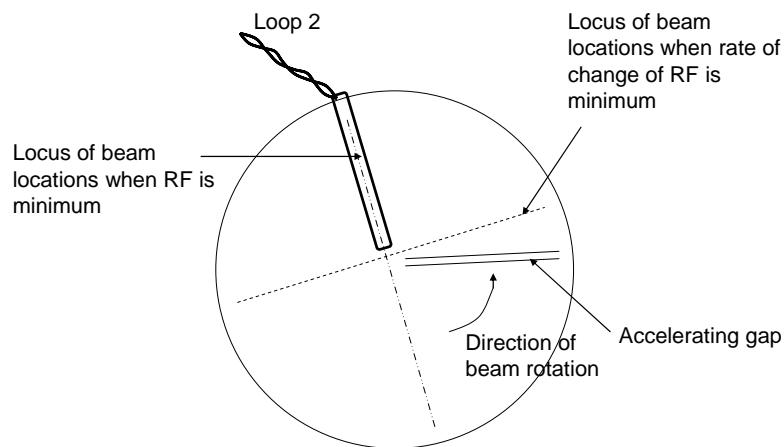


Figure H.6 Potential location of the sensor, in this case a loop sensor is illustrated. At this location the RF is minimum when the beam passes by the sensor.

Figure H.7 shows the case when more than one set of loops is used. In this case, two sets of loops are illustrated. They are arranged so that the rate of change of flux through one is opposite to the other, so they should show minimum coupling with the electric field. They are connected in series. In this case, there are two signals in the detection loop per cycle of the beam around the cyclotron.

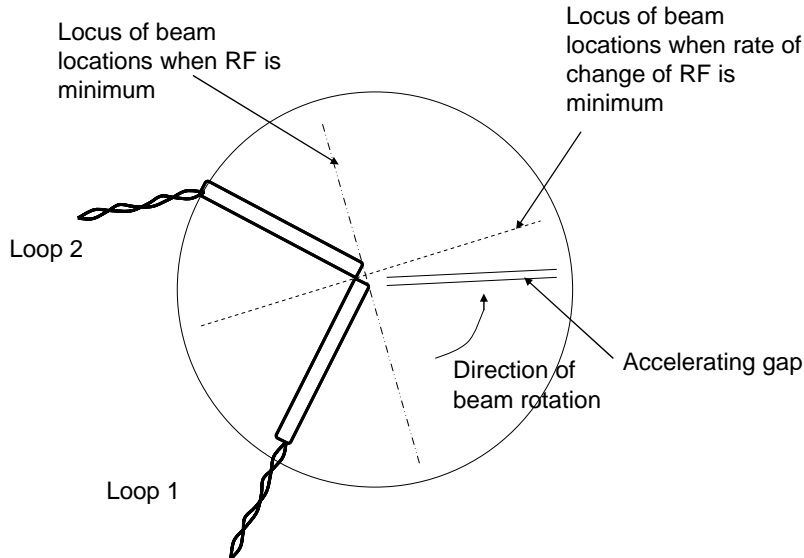


Figure H.7. Location of two sensors located in such a way that the RF pickup by the two sensors cancels each other, and the beam phase can be identified from two signals when the beam passes by each sensor.

It is possible to use the same locations for positioning of dipole antennas, if that is the preferred detector.

It should be understood that loops also refer to Rogowski coils. Although the loops are arranged so that the twisted pair of the current leads occurs in the large radius of the loop, other locations of the twisted pair around the loop are not excluded. Also, although the loop or Rogowski coil is shown in only half of the cyclotron, it could be placed along a diameter. In this case, it is possible to return the coil or loop through the opposite side of the beam chamber, in order to minimize common-noise and increase signal-to-noise ratio.

In the case of dipole antennas, it is possible to make the connection of the antenna between the antenna extremes, as shown in Figure H.8.

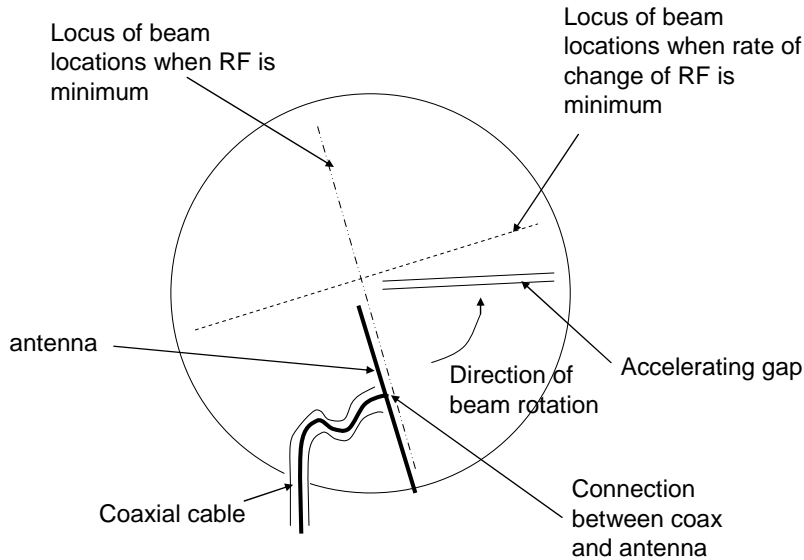


Figure H.8 Location of a dipole antenna for sensing the beam . In this case, the dipole antenna is located at the RF minimum when the beam passes through. The connection to the antenna is not necessarily at the extreme of the antenna, but it could be somewhere along the antenna.

Also, although the beam detector is shown radially, it may be advantageous for the detector to be curved. It would be possible to build in the sensor, by deviating from radial, phase differentials that are dependent on the energy of the beam (higher energy beam rotates at larger radii). In this manner, for example, the change in the sensing delay t_{sensor} that arises due to changes in the beam energy (and changes in radial location of the beam) can be offset by sensing the beam at an appropriate location, and there is no need for software adjustment.

It may also be possible to build into the hardware other phase compensators. One simple one would be to make longer cables or provide differential impedance in the lines.

Although only dipoles and loops have been described, other types of detectors can be used, including solid state detectors, fiber optics, cloud chambers. It is necessary for these sensors to have very fast response in order to determine the phase of the beam.

H.4 Ion sources for synchrocyclotrons

It would be ideal to match the ion source to the acceptance window of the RF in the cyclotrons. This is particularly important for synchrocyclotrons, as the beam acceptance duty cycle is very small. It would also be ideal to use sources without electrodes that have limited lifetime and require frequent maintenance.

There is development of pulsed sources, such as laser ion sources, for the generation of ions for injection into accelerating structures (either cyclotrons or RFQ's). [M. Sekine K. Kondo, M. Okamura and N. Hayashizaki, *A study of H^+ production using metal hydride and other compounds by means of laser ion source*, *Rev. Sci. Instrum.* **83**, 02B318 (2012)] Some of this work is relevant for the generation of protons of low energy.

The choice of material to be ablated is important. The material should have enough opacity that the laser beam does not go through the material. Thus, it has been shown that C-H compounds (beeswax, polyethylene) do not show signs of breakdown when illuminated with about 10^9 W/cm². In this case, there is no proton production. However, when hydrates are used that can absorb the beam energy, charged particle beams are generated, although with low efficiency. Slightly more energy, on the order of 10^{10} W/cm² does result in good emission, even in polyethylene. [L. Torrisi, S. Cavallaro, M. Cutroneo, D. Margarone, and S. Gammino, *Proton emission from a laser ion source*, *Rev. Sci. Instrum.* **83**, 02B310 (2012)] In this case, the ion energy is on the order of 150 eV, still somewhat higher than ideal for use in high performance synchrocyclotrons. In the case of the very high energy, even polyethylene can be used for generation protons. It should be noted that in the case of sufficient power, the addition of materials (nanoparticles) to the polyethylene does not result in improved hydrogen generation.

The issue of breakdown can be addressed by using higher frequency lasers, such as by double or, even better, tripling the frequency of infrared lasers, such as NdYAG or by placement of solid materials in the ablator material, such as nanoparticles or nanotubes. Ideally, the ion energy at the ion source should be low in order to provide higher brightness of the accelerated ion beam. Very high intensity laser ion sources (*i.e.*, around 10^{16} W/cm²) produce very energetic ions (up to several MeV's) and would not be accepted well by the synchrocyclotron. [L. Torrisi, L. Giuffrida, M. Cutroneo, P. Cirrone, A. Picciotto, *Proton emission from thin hydrogenated targets irradiated by laser pulses at 10^{16} W/cm²*, *Rev. Sci. Instrum.* **83** 02B315 (2012)]

For applications to synchrocyclotrons, an ablator that does not result in deposits that involve maintenance operation are desirable. Carbon-hydrogen ablators are not ideal in that the carbon or carbonaceous material may build in components inside the beam chamber. Hydrogen compounds that do not result in stable solids in the beam chamber are desirable. Two such compounds are water and ammonia. In both cases, the compounds need to be feed into the beam chamber in frozen condition, in order to minimize sublimation of the material. Limited sublimation is tolerable. For water, in order to prevent sublimation, temperatures around 200 K or lower are desirable. Similarly ammonia need to be help cold in order to prevent sublimation. In both cases, the water or its byproducts (oxygen ions, atoms and water clusters) and ammonia and its by products, (nitrogen, ammonium clusters, ...) would not build up in the machine.

Ideally the ion source is located along the axis, on the midplane of the machine. Thus, there are high magnetic fields. The performance of laser ion sources in the presence of strong magnetic fields needs to be investigated.

DEPARTMENT OF DEFENSE

DEFENSE THREAT REDUCTION
AGENCY
8725 JOHN J. KINGMAN ROAD
STOP 6201
FORT BELVOIR, VA 22060
ATTN: D. PETERSEN

DEFENSE TECHNICAL
INFORMATION CENTER
8725 JOHN J. KINGMAN ROAD,
SUITE 0944
FT. BELVOIR, VA 22060-6201
ATTN: DTIC/OCA

**DEPARTMENT OF DEFENSE
CONTRACTORS**

QUANTERION SOLUTIONS, INC.
1680 TEXAS STREET, SE
KIRTLAND AFB, NM 87117-5669
ATTN: DTRIAC